Detecting flow events in turbulent flow of vertical-slot fish passes

Zur Erlangung des akademischen Grades eines

DOKTOR-INGENIEURS

von der Fakultät für
Bauingenieur-, Geo- und Umweltwissenschaften
des Karlsruher Instituts für Technologie (KIT)

genehmigte

DISSERTATION

von
Dipl.-Ing. Béla Sokoray-Varga
aus Budapest

Tag der mündlichen Prüfung
26.10.2016

Referent:	Prof. Dr.-Ing. Dr. h.c. mult. Franz Nestmann
Korreferenten:	Prof. Dr.-Ing. Bodo Ruck
	Prof. Dr. Vladimir Nikora

Karlsruhe 2016

Abstract

The influence of turbulence on fish swimming is of considerable interest in both biological and engineering contexts. Fish-behavior investigations have contributed significantly to the understanding of the response of fish to different flow characteristics. However, it has not been clarified yet how the specific features of turbulence influence fish swimming performance. According to earlier publications, one of these features is the predictability of turbulence that, in this study, is interpreted as the existence of predictable changes in the flow field due to turbulence, which fish might be able to anticipate. Importantly, the feature of predictability refers to the flow alone without considering the ability of fish to recognize or use predictable changes of the flow.

The fundamental assumption of this work is that repeating changes in the flow are the basis for predictability, because repetition facilitates their recognition by experience on the fish' part. Leaning to this assumption, if repeating changes in the flow form repeating sequences of changes, the changes occurring later within the repeating sequence are considered predictable in the sense of short-term predictability, even if the repeating sequence itself occurs non-periodically. While the predictability of the flow is quite evident in case of a flow with periodic pattern, there are no methods available to reveal non-periodically repeating sequences of changes in the flow.

The objective of this thesis has been to develop a novel flow-analysis methodology suitable for detecting predictable turbulent *flow events* and their *occurrences* in vertical-slot fish passes, even if they occur non-periodically. Here, the term *flow event* refers to changes in the flow field associated with the appearance of turbulent flow structures or with their change of position and the term *occurrence* denotes instances of times at which the particular flow event happens.

The presented methodology is applied in this work to a Particle Image Velocimetry (PIV) measurement performed in the scale model of a vertical-slot fish pass and is based on Proper Orthogonal Decomposition (POD).

First, the velocity dataset measured by PIV is analyzed using conventional flow-analysis methods with the aims, on the one hand, to reveal the flow characteristics relevant for the presented methodology, and on the other hand, to discuss whether POD results are suitable to represent flow events.

Then, repeating sequences of large-scale flow events and their occurrences are detected based on POD results. The methodology essentially consists of the detailed examination of POD modes representing repeating flow events and the corresponding time series of POD coefficients. Once repeating flow events have been identified, repeating sequences of their occurrences can be detected based on the time series of the POD coefficients. In addition, it is shown that it is possible to involve in the analysis supplementary flow features that are not represented by POD modes.

Finally, it is demonstrated that the POD results leading to the detection of predictable flow events can also be obtained with low-resolution measurements that, in principle, can be carried out by means of point measurement techniques. This is essential for the applicability of the presented methodology to fish behavior experiments in full-scale facilities, where the occurrences of the predictable flow events have to be correlated with the simultaneous response of fish.

Kurzfassung

Sowohl in biologischer als auch in ingenieurtechnischer Hinsicht ist der Einfluss von Turbulenz auf das Schwimmverhalten von Fischen von großem Interesse. Versuche mit Fischen haben wesentlich zum Verständnis der Reaktion von Fischen auf Strömungen verschiedener Eigenschaften beigetragen. Es ist jedoch nicht abschließend geklärt, wie sich die einzelnen Eigenschaften der Turbulenz auf das Schwimmverhalten auswirken. Laut einer kürzlichen Studie ist eine der maßgebenden Eigenschaften die Vorhersagbarkeit von Turbulenz, welche nach Interpretation dieser Arbeit bedeutet, dass es vorhersagbare Änderungen der Strömung gibt, die von Fischen erkannt werden könnten. Die Vorhersagbarkeit bezieht sich dabei auf die Strömung und beinhaltet nicht die Fähigkeit von Fischen, vorhersagbare Änderungen in der Strömung zu erkennen.

Die grundlegende Annahme des angewendeten Ansatzes dieser Arbeit ist, dass sich wiederholende Änderungen in der Strömung die Basis für die Vorhersagbarkeit sind, da die Wiederholungen das Erkennen solcher Änderungen durch Erfahrung von Seite des Fisches fördern. Wenn sich solche Änderungen der Strömung in bestimmter Reihenfolge wiederholen, werden demzufolge die Änderungen am Ende der Abfolge (kurzfristig) vorhersagbar. Die Änderungen der Strömung, die am Ende der Abfolge auftreten, sind auch dann vorhersagbar, wenn die Abfolge sich nicht periodisch wiederholt.

Das Ziel dieser Arbeit war es daher, eine neuartige Strömungsanalyse-Methodik zu entwickeln, die geeignet ist, vorhersagbare turbulente *Strömungsereignisse* und deren *Auftreten* in vertikalen Schlitzfischpässen zu detektieren, auch wenn die Strömungsereignisse nicht periodisch auftreten. Der Begriff *Strömungsereignis (flow event)* wird in der vorliegenden Arbeit verwendet, um Änderungen in der Strömung zu bezeichnen, die mit dem Erscheinen oder Positionsänderung von turbulenten Strömungsstrukturen verbunden sind, und mit *Auftreten (occurrence)* wird das zeitliche Vorkommen bezeichnet. Während die Vorhersagbarkeit von periodischen Strömungsereignissen relativ evident ist, war das Ziel der Arbeit eine Methodik zu entwickeln, die zur Detektion von nicht periodischen Strömungsereignissen geeignet ist, weil dafür derzeit noch keine Methoden zur Verfügung stehen.

Fischpässe sind Bauwerke, die für Fische die Durchgängigkeit von Flüssen an Querbauwerken ermöglichen; sie werden in unterschiedlichen Ausführungen hergestellt, wobei der Schlitzpass einer der gängigsten Fischpasstypen ist. Anhand von früheren Studien wird deutlich, dass die Strömung innerhalb von Fischpässen stark turbulent ist. Die Vorhersagbarkeit der Strömung in Schlitzpässen ist von besonderer Bedeutung für die passierenden Fische, da Schlitzpässe aus Reihen von identischen Becken bestehen und dementsprechend hier die Kenntnis eines vorhersagbaren Musters, das am Anfang einer solchen Anlage gelernt wurde, in den weiteren Becken vorteilhaft einsetzbar ist.

Die präsentierte Methodik besteht aus einer Reihe von Strömungsanalysemethoden, mittels derer sich wiederholende Abfolgen von Strömungsereignissen und deren Auftreten detektiert werden können. Die Methodik wird in dieser Arbeit an experimentellen Ergebnissen einer Particle Image Velocimetry (PIV) Messung demonstriert, die im skalierten Labormodell eines Schlitzpasses ermittelt wurden.

Ein wesentlicher Bestandteil der Methodik ist die Anwendung von Proper Orthogonal Decomposition (POD), mit der sich wiederholende Strömungsereignisse effizient ermittelt werden konnten. Die im Schlitzpassmodell durchgeführte Messung wurde zunächst mittels konventioneller Strömungsanalyseverfahren und POD analysiert, um zu verstehen, wie POD-Resultate zu interpretieren sind.

Daraufhin wurden in dem gemessenen Geschwindigkeitsdatensatz wiederholt auftretende Strömungsereignisse auf Basis von POD-Resultaten identifiziert und analysiert. Auf diese Weise konnte gezeigt werden, wie wiederholende Abfolgen von Strömungsereignissen identifiziert werden können. Darüber hinaus wurde mit einem hypothetischen Beispiel demonstriert, wie zusätzliche Strömungseigenschaften, die eine vorteilhafte oder nachteilige Strömungssituation beschreiben, mit den sich wiederholenden Strömungsereignissen in die Analyse eingebunden werden kann.

Zum Schluss konnte im Rahmen der Arbeit gezeigt werden, dass die POD-Resultate, die für das Detektieren von vorhersagbaren Strömungsereignissen relevant sind, auch anhand von Messungen mit sehr niedriger Auflösung erhalten werden können. Dies belegt, dass die Detektion vorhersagbarer Strömungsereignisse prinzipiell auch mittels Punktmessungen möglich ist, wenn die für die Detektion relevanten POD-Komponenten vorher mittels PIV bestimmt wurden. Dies ist wichtig für die Anwendbarkeit der vorgestellten Methodik, da das Auftreten der vorsagbaren Strömungsereignisse mit dem Verhalten der Fische korreliert werden müssen, was nur durch mit Fischverhaltensbeobachtungen gleichzeitigen Strömungsmessungen möglich ist.

Acknowledgements

The present dissertation is based on the work carried out as part of the ongoing joint research of the Institute for Water and River Basin Management (IWG) at the Karlsruhe Institute for Technology and of the German Federal Waterways Engineering and Research Institute (BAW).

Several people have contributed to the realization of this thesis; some of them by participating in technical discussions, some of them by creating laboratory accessories and some of them by solving administrative difficulties. I would like to thank them all, and a few of them I would like to thank here separately.

Firstly, I would like to express my sincere gratitude to my advisor, Professor Franz Nestmann, for his continuous support of my research and for the many degrees of freedoms that he gave during the work. Besides my advisor, I am very grateful to my co-referees and all my committee members for their valuable advice given in various meetings, especially Professor Nikora, Professor Uhlmann and Professor Ruck for the challenging discussions.

I am also grateful to the leaders of the BAW for supporting the research and the experiments in their hydraulic laboratory.

I would like to thank many current and former colleagues both at the BAW and at the IWG for supporting me and for discussing with me various issues of the work. In particular, huge thanks go to Roman Weichert, Jochen Eckhardt, Walter Metz, Patrick Heneka, Frank Seidel, Sina Wunder, Irina Klassen and Boris Lehmann. I also thank the BAW laboratory support team for always helping out, especially Roy, Bruno, Klaus, Andreas and Peter.

I owe thanks to Jochen Kriegseis for his help in understanding the mathematical background of POD and for discussing with me on the interpretation of POD results.

Special thanks go to Giordano Lipari who has discussed with me several issues of my work since 2006 and without whom I would not have gained the critical thinking on turbulence data I did.

Finally, I also want to thank my former colleagues at Department of Hydraulic and Water Resources Engineering at the Budapest University of Technology and Economics for our valuable discussions, especially János Józsa, Sándor Baranya and Tamás Krámer.

Content

List of Symbols

Latin

a	POD coefficient	-
a_i	POD coefficients corresponding to POD mode i	-
B	pool width	L
c_u	scale ratio of velocities	-
c_l	scale ratio of lengths	-
c_t	scale ratio of times	-
C_{md}	discharge coefficient	-
CMF_u, CMF_v, CMF_w	cumulative mean function of the velocity components u, v, w	L/T
CVF_u, CVF_v, CVF_w	cumulative variance function of the velocity components u, v, w	L^2/T^2
E_D	rate of dissipated energy per unit pool volume	$1/(LT^2)$
f	frequency	1/T
g	gravity	L/T^2
h	water depth	L
h_m	mean water depth	L
h_o	water depth before slot	L
h_u	water depth after slot	L
K	number of segments used in Welch’s method	-
l	length	L
L	pool length	L
$L_{C,x}$, $L_{C,y}$	characteristic length scales in directions x, y	L
l_0	integral length scale	L
l_{EI}	length scale separating the energy containing and the inertial subranges	L
l_{DI}	length scale separating the inertial and the dissipative ranges	L
N	total number of samples in the measurement	-
Q	discharge	
Re	Reynolds number	-
s	slot width	L
S_{uu}, S_{vv}, S_{ww}	One-sided PSD of the velocity components u, v, w	L^2/T
$S_{uu}^{(w)}$, $S_{vv}^{(w)}$, $S_{ww}^{(w)}$	One-sided PSD of u, v, w created by using windowing	L^2/T
$S_{uu}^{(a,w)}$, $S_{vv}^{(a,w)}$, $S_{ww}^{(a,w)}$	Averaged one-sided PSD of u, v, w created by using windowing	L^2/T
$S_{uu}^{(n)}$, $S_{vv}^{(n)}$, $S_{ww}^{(n)}$	One-sided PSD of the noise in the velocity components u, v, w	L^2/T
t	time	L/T
t_n	n-th time step	-
$t^{(95\%)}$	95%-duration	T
TKE	turbulent kinetic energy	L^2/T^2
u	flow velocity	L/T
u_0	characteristic velocity of the integral scale	L/T

u_η	characteristic velocity of the Kolmogorov scale	L/T
$u_{max,s}$	maximal flow velocity in the slot	L/T
$\mathbf{u}$	velocity vector	L/T
$\mathbf{u^i}$	instantaneous velocity vector	L/T
$\mathbf{u^m}$	mean velocity vector	L/T
$\mathbf{u^{md}}$	velocity vector within a POD mode	L/T
u', v', w'	fluctuation of the velocity components in x, y and z directions	L/T
u^i, v^i, w^i	instantaneous values of the velocity components	L/T
$u^{i,(n)}, v^{i,(n)}, w^{i,(n)}$	instantaneous noise in the velocity components	L/T
u^m, v^m, w^m	mean values of the velocity components	L/T
u^{sf}, v^{sf}, w^{sf}	spatial fluctuation of the velocity component *u, v, w*	L^2/T^2
VAR_u, VAR_v, VAR_w	variances of the velocity component *u, v, w*	L^2/T^2
$VAR_u^{(n)}, VAR_v^{(n)}, VAR_w^{(n)}$	variances produced by noise in the velocity component *u, v, w*	L^2/T^2
w_i	weighting	-
x, y, z	spatial coordinates	L

Greek

α	pool geometry dependent coefficient	-
Δ	difference	-
$\in$	error	%
η	Kolmogorov scale	L
ν	kinematic viscosity of water	L^2/T
$\mu_{r,u}, \mu_{r,v}, \mu_{r,w}$	*r*-th order central moment of the velocity fluctuation time series of the velocity component *u, v, w*	L^4/T^4
ρ	density of water	M/L^3
ρ_p	density of particle	M/L^3
τ	time-scale	T
$\tau_{I,u}, \tau_{I,v}, \tau_{I,w}$	integral time-scales of the velocity component *u, v, w*	*T*
τ_p	relaxation time of particle	T
$\sigma_u, \sigma_v, \sigma_w$	standard deviations of the velocity component *u, v, w*	L/T
τ_0	time-scale at the integral scale	T
τ_η	time-scale of the Kolmogorov scale	T

Subscripts

(P)	quantity measured in the prototype
(M)	quantity measured in the scaled model
uv	quantity calculated using only the u and v velocity components

1 Introduction

The ecological continuity of rivers is an important element of their good ecological status, which is one of the key targets of the European Water Framework Directive. The longitudinal connectivity is of particular importance for fish. It assures not only the longitudinal migration to spawning areas for migratory fish, but also ensures the sufficient extent of fish habitats by gaining access to areas in upstream or downstream sections of rivers. Artificial or natural transversal obstructions in rivers like falls, dams, weirs or barrages usually represent obstructions to the longitudinal connectivity, as they are unpassable barriers for most species.

Figure 1.1 View of the vertical-slot fish pass in Koblenz, Germany (Image: BAW)

Fish passes are hydraulic structures that are built to facilitate the passage of such transversal obstructions by fish, in either upstream or downstream direction. In facilities providing upstream passage, like the vertical-slot fish pass (Figure 1.1), the flow usually becomes highly turbulent due to high flow velocities and high velocity gradients.

The main objective of fish pass design guidelines is to create facilities that are adjusted to the biological requirements of the target fish species considering a wide range of factors. The requirements of fish are, however, still being researched regarding several factors.

For the swimming performance of fish against the mean flow velocity, a quite clear relationship was determined in the past between swimming speed, fish size and fish endurance based on fish-behavior experiments (see Section 1.1). The mean flow velocities within fish passes are accordingly limited by the guidelines based on the limited swimming capability of fish.

In contrast, the influence of turbulence on fish swimming performance is one of the ongoing major research topics worldwide. Although it has been recognized by fish-behavior investigations that turbulence can significantly decrease the swimming performance of fish, it could not be clearly shown to date how the individual features of turbulence determine this influence. Accordingly, fish pass design guidelines contain currently no specifications on the features of turbulence in vertical-slot fish passes (e.g. DWA 2014).

Since earlier fish-behavior studies focusing on individual turbulence features lead to inconsistent results, it has been proposed in a recently published framework on fish-behavior investigations to conduct and evaluate such experiments in the future using a combination of different features of turbulence. The suggested features are the intensity and the predictability of turbulence as well as the features describing the orientation and the scale of the turbulent structures (see Section 1.1). Thereby, the predictability of turbulence is interpreted in this work to indicate whether there are changes in the flow due to turbulence that fish might be able to anticipate.

The feature of predictability might be of particular importance in vertical-slot fish passes, because they consist of a series of pools, which means that fish encounter the same flow again and again while swimming through the pools. Patterns learned at the beginning of such a facility can be expected to be recognized further upstream.

While at least estimation methods are known for determining the intensity features of turbulence, and the orientation and scale features of flow structures, there is no flow-analysis method available to detect and examine predictable changes in the flow, unless they occur periodically (see Section 1.1). Periodicity, however, develops in turbulent flows only under very special conditions and is rather rare in natural flows or in hydraulic structures of complex geometries. As long as the predictability of non-periodically repeating changes in the flow cannot be investigated, the influence of the predictability of turbulence is going to be neglected in the assessment of the swimming performance of fish. For this reason a novel flow-analysis methodology is required that is suitable for investigating the predictability of non-periodically occurring flow changes.

1.1 Background

The vertical-slot fish pass is one of the most popular types of fish passes providing upstream passage. It consists of a rectangular open channel divided into a series of pools that are interconnected by vertical slots, where water flows through from pool to pool from the headwater to the tailwater, so that fish can swim through the slots from pool to pool from the tailwater to the headwater of a barrage. In this way, the large height difference between the headwater and the tailwater is distributed among the water level differences between the pools of the fish pass. The water level differences at the slots create a jet-like main stream in the pools represented by high flow velocities, which results in highly turbulent flow within the pools due to the high velocity gradients (e.g. Rajaratnam et al. 1986, Rajaratnam et al. 1992, Larinier 1992, Wu et al. 1999, Puertas et al. 2004; Liu et al. 2006; Tarrade et al. 2008, Wang et al. 2010, Tarrade et al. 2011).

Turbulence is characterized by fluctuations of the flow velocity about the mean velocity. These fluctuations arise due to the unsteady turbulent flow structures and flow instabilities, which occur over a wide range of temporal and spatial scales in natural flows or hydraulic structures with complex geometries, like fish passes. Turbulence is consequently characterized by different features, like the statistical characteristics of the fluctuations or the size or orientation features of the flow structures.

Swimming performance of fish against the mean flow velocity is described by the speed that a fish can maintain over a period of time and can be classified to three different swimming modes (e.g. Hoar and Randall 1978, Powers and Orsborn, 1984). While the so called sustained swimming speed can be maintained without fatigue, because it is an aerobic swimming, swimming at higher speeds (prolonged and burst speeds) leads to fatigue. A functional relationship can be given between the swimming speed and the time to fatigue, in which the higher the swimming speed is, the sooner the fatigue occurs. This relationship depends on several factors like temperature, fish species, or fish size. If fatigue once occurs, a resting period is needed for muscle recovery. In theory the distance a fish can swim can be calculated based on the flow velocity, the fish speed and the fatigue time, but such a calculation is very simplified, as this relationship does not consider, among others, the influence of turbulence decreasing the swimming performance and is not indicating the variance between fish individuals.

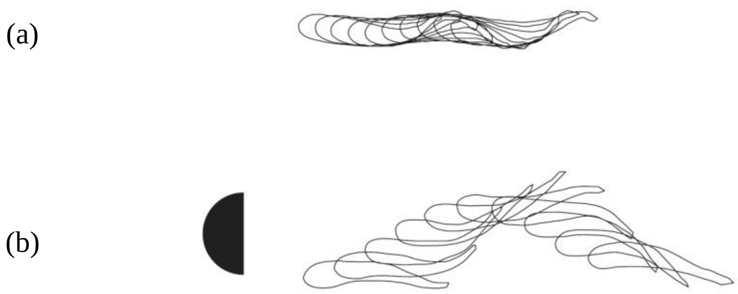

Figure 1.2 Swimming pattern of trout: (a) in steady flow, (b) in a Karman-vortex-street. The ten body contours show approximately one tail-beat cycle (after Liao2007)

The influence of turbulence on fish behavior was addressed by numerous experiments in the past. In such investigations turbulence has mostly been recognized as a flow characteristic that affects the swimming performance of fish by causing an increase in the energy costs of swimming or by disturbing the ability of fish to hold their position. Though, it is not clearly shown to date how the individual features of turbulence determine this influence. Since the individual features playing a role have been gradually identified by such investigations, most studies had disregarded the features that were identified later. Earlier studies evaluated only the statistical characteristics of the fluctuations, like the standard deviation, turbulent kinetic energy, Reynolds shear stress and their normalized forms (e.g. Odeh et al. 2002, Enders et al. 2003, Nikora et al. 2003, Guiny et al. 2005, Smith et al. 2005). The scale and the orientation features of the flow structures were first involved after some studies could not show an influence based on the intensity features (e.g. Nikora et al. 2003, Tritico et al. 2010). Other research groups in turn examined fish behavior in Kármán vortex streets and observed that fish could take advantage of the periodic changes in the flow due to the periodic vortex shedding (Liao et al. 2003, Pryzbilla et al. 2010).

Lacey et al. (2012) have therefore proposed to evaluate future fish-behavior examinations using the combination of the features describing the intensity and the periodicity of turbulence as well as the features describing the orientation and the scale of the turbulent structures in order to obtain comparable results. The feature of periodicity is thereby intended to indicate whether there are changes in the flow that might be anticipated by fish, which is reconsidered in the following.

Periodicity develops in turbulent flows only under very special conditions and is rather rare in natural flows or in hydraulic structures of complex geometries. The term periodicity is mathematically well defined; a periodic function repeats its values at regular time intervals. Periodicity has been selected as a relevant feature by Lacey et al. (2012), because trout were observed to adjust their swimming pattern to the vortex shedding characteristics of the periodic vortices in Kármán vortex streets (Figure 1.2). The studied fish made use of the flow velocities reduced by the upstream directed velocity component of the rotating vortices, thereby reducing their swimming costs (Liao 2003). Crucial to this behavior is that fish knew by experience what vortex arrives next with the flow; hence they could anticipate changes in the flow.

Predictability might, however, arise without a periodic pattern. If a particular sequence of changes in the flow occurs again and again repeatedly, the changes at the end of the sequence are hypothetically predictable, even if the sequence is repeating in non-regular time intervals. Whether fish can make use of the predictability based on such non-periodically repeating sequences of changes in the flow has not been investigated explicitly yet. For the investigation of such behavior, first a flow-analysis method is required that is suitable for identifying non-periodically repeating changes in the flow, so that fish behavior can be correlated with such changes in the flow.

Changes in the flow due to turbulence can be associated with the appearance and position change of turbulent flow structures. The investigation of turbulent flow structures in highly turbulent flows is, however, particularly challenging, since flow structures of different time and length scales appear simultaneously, hence superimposed, in the velocity fields (see Section 2.1). The superposition of flow structures disturbs both the detection and the feature determination of the individual flow structures. In addition, the flow field in the pools of vertical-slot fish passes is significantly inhomogeneous due to the presence of the jet-like main stream, which is limiting the applicable analysis methods (e.g. Adrian et al. 2000). Moreover, an unsteady main stream grants further complexity to the flow, since the fluctuations generated by the main stream might have similar frequencies as other large flow structures (see Section 0), which further complicates the distinction between different structures. Although these suggest separating the flow structures of different scales by some means, an appropriate separation is still being searched for (e.g. Sokoray-Varga et al. 2014).

Considering recent observations, the feature of predictability of turbulence is of particular interest in vertical-slot fish passes. The main stream in the pools appeared to show an unsteady, oscillating pattern in some laboratory scale model investigations (e.g. Wang et al. 2010, Sokoray-Varga et al. 2012), which has been confirmed using flow-analysis methods by Tarrade et al. (2011). Although fish appeared to make use of the oscillating character of the flow during crossing the slot in the observations of Wang et al (2010), this fish behavior could not be correlated with the unsteady flow, because, on the one hand, the flow measurements were not carried out simultaneously with the fish observations and, on the other hand, there was no flow-analysis methodology available that was suitable for detecting predictable flow events. Thus, the predictability aspects of the oscillation process have not been examined so far.

1.2 Objectives and approach

The work resulting in this thesis has been carried out as part of an ongoing joint research initiative between the Institute for Water and River Basin Management (IWG) at the Karlsruhe Institute for Technology and the German Federal Waterways Engineering and Research Institute (BAW). The aim of this joint research is to improve the design criteria of vertical-slot fish passes by considering a wide range of aspects. In the framework of the research program, fish-behavior experiments are planned in order to enhance our understanding of the fish-hydraulics interactions in such facilities and, thereby, improve their design criteria.

The objective of this thesis has been to develop a flow-analysis methodology for detecting turbulent *flow events* in vertical-slot fish passes whose *occurrences* are predictable (short-term predictability). Here, the term *flow event* refers to changes in the flow field associated with the appearance of turbulent flow structures or with their change of position, such as the appearance of a turbulent eddy at a location or the trajectory displacement of an unsteady main stream. The term *occurrence* denotes instances of times at which the particular flow event happens, e.g. when a particular turbulent eddy appears at a given location. Since it is reasonable to assume that in vertical-slot fish passes periodic flow events are unlikely, a methodology is required that is suitable for investigating the predictability of repeating flow events that occur non-periodically, that can later be used for the evaluation of the fish-behavior experiments.

The fundamental assumption of the present approach is that repeating flow events are the basis for predictability, because repetition facilitates their recognition by experience on the fish' part. Leaning on this assumption, the following requirements for predictability have been formulated:

1. flow events occurring repeatedly in the flow exist,
2. repeating sequences of different flow events exist.

If these conditions are fulfilled, the flow events occurring later within the repeating sequence can be considered predictable in the sense of short-term predictability, even if the sequence itself is repeating non-periodically.

It has to be highlighted that the feature of predictability refers to the flow alone. Whether fish are able to recognize and use predictable flow events of given characteristics is a separate issue, which will have to be ascertained using fish-behavior experiments in the future by correlating fish behavior and the occurrences of predictable flow events. Hence, the present work has the objective to develop a methodology that detects predictable flow events and their occurrences based on flow analysis methods.

In order to achieve this goal, first a laboratory model of a vertical-slot fish pass has been designed and built in the laboratory of the BAW in Karlsruhe with a geometric scale of 1:4.1, and then, a 2D-2C Particle Image Velocimetry (PIV) measurement performed in this model has been used to identify predictable flow events by means of a combination of flow-analysis methods.

1.3 Thesis outline

The outline of the thesis is as follows.

Chapter 2 provides first a brief summary on the origin and the scales of turbulence as known from the turbulence theory and then introduces the computation methods that were used in this work for the characterization of turbulent flows.

Chapter 3 presents a literature review on the hydraulics of vertical-slot fish passes relevant for the methodology described in Chapter 6.

Chapter 4 describes first the laboratory scale model and the experiment execution, then addresses possible scale effects arising from the use of scale models by considering the model similitude, and presents finally the used Particle Image Velocimetry (PIV) system including the methods used for the PIV evaluation.

Chapter 5 displays the results of the PIV measurement analyzed using the methods described in Chapter 2. The analysis has the objective to reveal the flow characteristics relevant for the methodology presented in Chapter 6. The chapter shows time-series analysis results, the results of Proper Orthogonal Decomposition (POD), and considerations on the interpretation of POD results.

Chapter 6 presents the methodology developed for detecting predictable flow events, considerations on involving supplementary flow features in the examination and considerations on performing the measurements without using PIV.

Chapter 7 closes with summary, conclusions and recommendations for the future work.

2 Characterization of turbulent flows

In this chapter a brief summary is given first on the origin and the scales of turbulence; then, the methods are presented that were used in this work for the characterization of turbulent flows.

2.1 Origin and scales of turbulence

Most flows occurring in nature and in engineering practice are turbulent. Accordingly, there is a very large amount of literature available on turbulence, so that the following information can be found in the most textbooks on turbulence (e.g. Pope 2000, Davidson 2004).

Turbulence is characterized by *random fluctuations* of the flow velocity about the mean velocity (Figure 2.1). The random characteristic denotes that different realizations of the same experiment yield to different temporal sequences of the fluctuations; hence the exact sequences of fluctuations are not reproducible in detail.

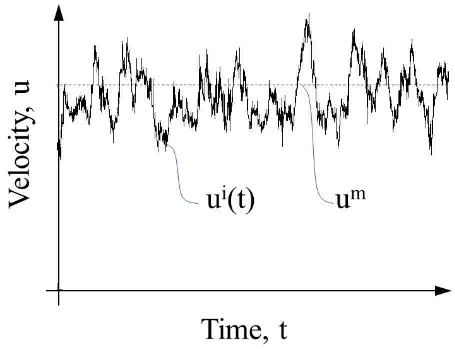

Figure 2.1 Velocity fluctuations typical for turbulent flows

The reason for the random characteristic is that although the Navier-Stokes equation describing fluid motion is deterministic, its non-linearity leads to *chaotic behavior* of the result under certain conditions. Chaotic behavior means that the result is sensitive to disturbances of the initial conditions, which implies, for example, that small disturbances in the inflow velocities or in the upstream water levels of a channel induce perturbations in the flow velocities downstream. As disturbance free initial conditions never occur, no realizations of the flow yield exactly the same sequences of fluctuations. Furthermore, the induced perturbations are themselves disturbances for the later flow development.

A good indicator of how sensitive the flow is to disturbances of the initial conditions is the *Reynolds number*:

$$Re = \frac{u \cdot d}{\nu} \tag{2.1}$$

where u is the characteristic velocity of the flow, d is the characteristic length scale of the flow and ν is the viscosity of water ($\nu \sim 10^{-6}$ m^2/s). The characteristic length scale of the flow can be chosen as the smallest measure of the flow, which is usually e.g. its depth in open channel flows or its width in case of jets.

The Reynolds number is a measure of the ratio of the inertial forces to the viscous forces in the investigated flow. Inertial forces are the forces required to slowdown the moving fluid; viscous forces are the forces that are exerted by the internal friction of the fluid to decrease the velocity of the moving fluid.

At low Reynolds numbers the viscous forces are large enough to damp the perturbations of the flow velocities, so that disturbances do not lead to fluctuations in the result, and the flow is not sensitive to disturbances of the initial conditions (laminar flow). At high Reynolds number, in turn, the damping effect of the viscous forces is largely insufficient to suppress the perturbations, which leads to *flow instabilities* and to a complex series of events yielding to the random fluctuations of the flow velocity (turbulent flow). For this reason, the flow at high Reynolds numbers is sensitive to disturbances of the initial conditions. In general, the higher the Reynolds number is, the more sensitive is the flow to disturbances. Since this sensitivity also depends on the magnitude of the disturbance, a universal critical value of the Reynolds number above which the flow is always turbulent does not exist. However, at the scales of typical open channel flows in engineering practice the flow can be considered to be fully turbulent if $Re \gg 2000$.

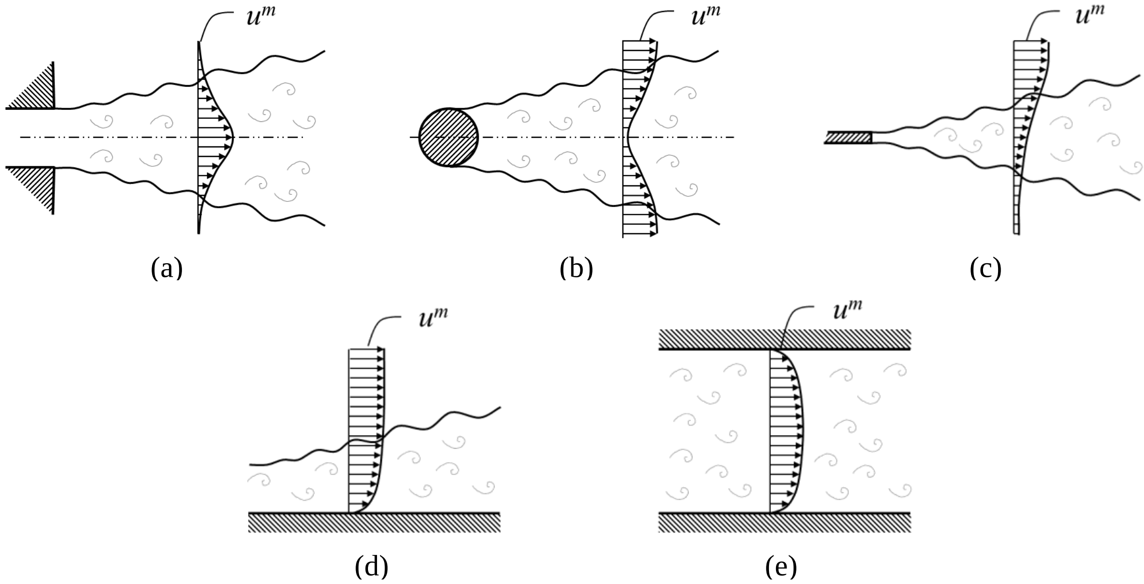

(a) (b) (c)

(d) (e)

Figure 2.2 Simple shear flow types: (a) jet, (b) wake, (c) mixing layer, (d) boundary layer and (e) channel flow

A high potential to become turbulent have flows with velocity gradients called shear flows, because the evolving flow instabilities can transport fluid of given velocity to a flow region with significantly different velocity, which generates further instabilities. Simple types of shear flows are the free shear flows (e.g. jet, wake, mixing layer), which are remote from walls and where turbulence arises due to the velocity gradients, and wall-bounded shear flows (e.g. pipe, flat-plate boundary layer), where both mean value and fluctuation of the velocity must be zero at the wall (Figure 2.2). Most flows in engineering practice are more complex than these simple flow types. Since the flow in vertical-slot fish passes is dominantly a free shear flow, the following description mainly presents turbulence from free shear point of view.

In flows at high Reynolds numbers the instabilities developed in the flow generate turbulent flow structures characterized by rotating motion, called eddies. These eddies become themselves unstable and break up to smaller eddies, which are also unstable and break up to even smaller and smaller eddies. The *break-up process* of eddies is essentially driven by inertial forces and continues until the eddies are so small, that the energy of the eddies get dissipated. This can be recognized based on the Reynolds numbers of the eddies. Eddies can be characterized by their size l, their characteristic velocity $u(l)$, their characteristic time scale (which is the turn-over-time) $\tau(l)=l/u(l)$, and their Reynolds numbers $Re_l(l)=u(l)l/\nu$. While the eddy sizes get smaller and smaller, their characteristic velocities, time scales and Reynolds numbers decrease. As the eddies are so small, that the viscous forces become significant, the energy of the eddies get dissipated.

The above process is also called the *energy cascade* and it describes how the kinetic energy of the mean flow gets dissipated through turbulence. First, the largest eddies extract energy from the kinetic energy of the mean flow, then, the kinetic energy is transferred from larger eddies to the smaller eddies through the break-up process without extracting further kinetic energy from the mean flow, and finally, the kinetic energy is dissipated by the smallest eddies. As these three different processes coincide with the scales of eddies, they are assigned to ranges of eddy sizes: the energy containing range, the inertial subrange and the dissipation range, where the two latter ones form the universal equilibrium range. Further, the distribution of the turbulent kinetic energy among eddies of different sizes is well displayed by the energy spectrum as illustrated in Figure 2.3.

The turbulent flow finally consists of lots of eddies of different time and length scales, which occur superimposed in the velocity fields and in the fluctuations of the time series. Although the exact sequences of fluctuations, hence the exact occurrences of eddies, are not reproducible in detail by different realizations of the same experiment, the statistical quantities of the fluctuations are reproduced well, because the *scales of all eddies* mainly depend on the characteristic scales of the mean flow, the boundary and the viscosity of the fluid. This dependence is demonstrated in more details next.

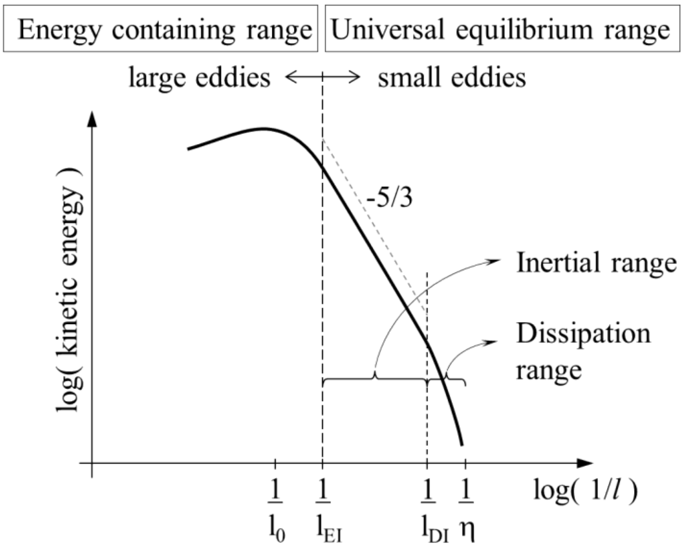

Figure 2.3 A typical distribution of the turbulent kinetic energy among the eddies of different sizes at high Reynolds numbers

The largest eddies are created by mean flow instabilities. The geometric characteristics of the *large eddies* contained by the *energy containing range* are determined by the mean flow geometry and are affected by the boundary conditions of the flow. The geometry of large-scale eddies has accordingly directional biases, i.e. differences in the fluctuations of different directions. Their size l_0 is comparable with the characteristic geometric length scales of the mean flow, their characteristic velocity u_0 is on the order of magnitude of the mean standard deviation, their Reynolds number $Re_0=u_0l_0/\nu$ is in the order of magnitude of the mean flow Reynolds number and their characteristic time scale is $\tau_0=l_0/u_0$. It has to be pointed out that these eddy sizes and characteristics have to be interpreted as order of magnitudes. An exact size at which large eddies are created cannot be specified, in particular because the sizes vary from eddy to eddy due to the chaotic behavior of the flow. This accordingly also applies to other eddy characteristics.

While large eddies become unstable and break up to smaller and smaller eddies, the directional biases gradually vanish, so that eddies below a certain size are statistically isotropic and are called *small eddies* ($l<l_{EI}$, $l_{EI}\sim 1/6*l_0$). In addition, below a certain size eddies are not created by the mean flow but by breaking up of larger eddies, which implies that neither energy nor directional biases of the mean flow are introduced at these scales. In the *universal equilibrium range*, where the eddies are isotropic and the mean flow does not introduce energy or directional biases, the eddy characteristics are similar for all flows at high Reynolds numbers and the break-up process gain universal characteristics. This can be well observed in the *inertial subrange*, where the distribution of the kinetic energy across the eddy sizes follows the universal -5/3-power-law function, which can be recognized on the -5/3 slope of the energy spectrum displayed in logarithmic scale. Thus the kinetic energy content of the eddy sizes can be determined by the kinetic energy level at l_{EI}. The characteristic velocities and time scales belonging to eddy size l in the inertial subrange can be calculated as:

$$\begin{aligned} &u(l)\sim u_0\cdot(l/l_0)^{1/3} \\ &\tau(l)\sim\ \tau_0\cdot(l/l_0)^{2/3} \end{aligned} \tag{2.2}$$

The inertial subrange ends at the eddy size where dissipation becomes significant (l_{DI}). In the *dissipation range* ($l<l_{DI}$, $l_{DI}\sim 60*\eta$) the kinetic energy content gradually reduces as viscous forces are more and more significant with decreasing eddy sizes. The smallest eddies that occur in a turbulent flow are defined by the *Kolmogorov scale*. The characteristic length η, the characteristic velocity u_η and the characteristic time scale τ_η, of these eddies can be calculated based on the Reynolds number of the mean flow as:

$$\begin{aligned} &\eta\sim l_0\cdot Re^{-3/4} \\ &u_\eta\sim u_0\cdot Re^{-1/4} \\ &\tau_\eta\sim\ \tau_0\cdot Re^{-1/2} \end{aligned} \tag{2.3}$$

Equations (2.2) and (2.3) confirm that the characteristics of small-scale eddies are only dependent on the characteristics of the large-scale eddies (l_0, u_0, t_0) and on the Reynolds number of the mean flow. Once the large eddies of a flow are characterized, the small scales can be well estimated, which demonstrates why the characterization of the large eddies is essential.

Since the characteristics of the large eddies are determined by the characteristics of the mean flow and the boundary of the flow, the characteristics of all eddies in the different ranges essentially depend on these characteristics. This contributes to the statistical quantities of the fluctuations being well reproduced in different realizations of the same experiment, even though the exact sequences of flow structures, hence fluctuations, are not reproducible in detail. This highlights why the statistical description is indispensable for the characterization of turbulence.

As mentioned before, most flows in the engineering practice are more complex than the simple shear flow types presented previously. More complex flows usually contain several flow processes that produce large eddies simultaneously, so that the generated fluctuations and eddies appear superimposed in the measured velocities and the energy cascade.

2.2 Definitions

For the following description of the methods used for characterizing turbulent flows it is important to declare that the present work uses the *Eulerian description of the flow*, i.e. the temporal evolution of the flow velocities are described at fixed locations of space as:

$$\mathbf{u}^i(x,y,z,t) = u^i(x,y,z,t)\cdot\mathbf{e}_x + v^i(x,y,z,t)\cdot\mathbf{e}_y + w^i(x,y,z,t)\cdot\mathbf{e}_z \tag{2.4}$$

where $\mathbf{u}^i$ is the instantaneous three-dimensional flow velocity vector at location (x, y, z) and time t (i stands for “instantaneous”), $\mathbf{e}_x$, $\mathbf{e}_y$ and $\mathbf{e}_z$ are orthonormal unit vectors in x, y and z directions of the three-dimensional Cartesian coordinate system respectively; and u^i, v^i and w^i are the magnitudes of the velocity components in x, y and z directions of the same coordinate system respectively.

The velocity information is provided as *discrete data* both in time and space in the present work due to the applied measurement technique. Velocity information that is discrete in time is provided as time series at the individual locations, velocity information that is discrete in space is provided at discrete locations of a field, in grid points of a rectangular grid.

A velocity time series is a sequence of velocity data collected over time. The velocity time series in present work consist of velocity data at equidistant, discrete time steps at a fixed location of space. The discrete time values of the time steps can be given in time as:

$$t_n = n\cdot\Delta t = n\cdot\frac{1}{f_s}, \quad n = 1,2,\dots,N \tag{2.5}$$

where Δt is the time difference between samples, f_s is the sampling frequency of the measurement, n denoting the time step and N is the number of time steps (sample size).

As described previously, turbulence is represented by the fluctuation of the velocity time series. The fluctuating part of the velocity is obtained by the *Reynolds decomposition*, namely by subtracting the mean velocity from the instantaneous velocity as (e.g. Pope 2000):

$$\begin{aligned} u'(x,y,z,t) &= u^i(x,y,z,t) - u^m(x,y,z) \\ v'(x,y,z,t) &= v^i(x,y,z,t) - v^m(x,y,z) \\ w'(x,y,z,t) &= w^i(x,y,z,t) - w^m(x,y,z) \end{aligned} \tag{2.6}$$

where u', v' and w' are the fluctuations of the velocity components; and u^m, v^m and w^m are the mean values of the velocity components. In this work, the mean values of the velocity components were determined using the temporal means defined as:

$$\begin{aligned} u^m(x,y,z) &= \frac{1}{N}\cdot\sum_{n=1}^{N} u^i\ (x,y,z,t_n) \\ v^m(x,y,z) &= \frac{1}{N}\cdot\sum_{n=1}^{N} v^i\ (x,y,z,t_n)\,. \\ w^m(x,y,z) &= \frac{1}{N}\cdot\sum_{n=1}^{N} w^i\ (x,y,z,t_n) \end{aligned} \tag{2.7}$$

The *mean velocity field* is the vector field consisting of the mean velocity vectors $\mathbf{u}^m$(x,y,z) in the individual grid points, which is defined as:

$$\mathbf{u}^m(x,y,z) = u^m(x,y,z) \cdot \mathbf{e}_x + v^m(x,y,z) \cdot \mathbf{e}_y + w^m(x,y,z) \cdot \mathbf{e}_z \tag{2.8}$$

Particle Image Velocimetry (PIV) technique provides *velocity datasets* of a measurement field. A *velocity dataset* consists of individual velocity fields that represent different time steps of a velocity acquisition in the same grid points, which can also be considered as simultaneously measured velocity time series in the individual grid points. The velocity dataset can be analyzed using different approaches. The velocities in a grid point captured over time can be analyzed by time-series analysis tool. The instantaneous velocity vectors at a time step represent an *instantaneous velocity field*, which can be examined for spatial structures in the flow. A combined investigation involving the temporal and spatial dimensions is called spatio-temporal analysis.

It has to be highlighted that, although the methods are presented in this section for three-dimensional velocity data (*u*, *v*, *w*), they are applied during the analysis using only the *u* and *v* velocity components. This means that flow features normally consisting of three velocity components are calculated here using only two components, which is denoted by the subscript “uv” (e.g. TKE_{uv} is the turbulent kinetic energy involving only the *u* and *v* components). The velocity components involved in the calculation of an individual flow feature are generally marked as subscript of the flow feature notation, e.g. σ_v is the standard deviation of the *v* velocity component.

2.3 Statistical analysis of time series

The equations of componentwise calculated characteristics, hence involving velocity component separately, are only presented for the u velocity component in this subsection and can be analogously implemented for further velocity components.

2.3.1 Statistical features of fluctuations

The standard deviation of the velocity time series can be calculated as:

$$\sigma_u\ (x,y,z) = \sqrt{\frac{1}{N} \cdot \sum_{n=1}^{N} (\, u'\ (x,y,z,t_n)\,)^2}. \tag{2.9}$$

The variance of the velocity time series (also called second order central moment) is:

$$VAR_u\ (x,y,z) = \sigma_u^2 = \frac{1}{N} \cdot \sum_{n=1}^{N} (\, u'\ (x,y,z,t_n)\,)^2 \tag{2.10}$$

The *r*-th order central moment about the mean of a velocity time series can be obtained as:

$$\mu_{r,u}(x,y,z) = \frac{1}{N} \cdot \sum_{n=1}^{N} (\, u'\ (x,y,z,t_n)\,)^{\mathrm{r}} \tag{2.11}$$

The turbulent kinetic energy (TKE) represents the average kinetic energy per unit mass contained by the velocity fluctuation and can be calculated using the variance of the velocity components, i.e. the square of the standard deviations:

$$TKE(x,y,z) = \frac{1}{2}(\sigma_u^2 + \sigma_v^2 + \sigma_w^2). \tag{2.12}$$

2.3.2 Velocity spectra

The velocity spectrum shows how the turbulent kinetic energy (more precisely, the variance) of the fluctuation is distributed over frequency, that is to say it reveals the contribution of the different frequencies to the total variance of the fluctuation. The velocity spectrum is usually regarded as an approximation of the kinetic energy distribution across the eddy sizes (see Figure 2.3) through the application of Taylor's hypothesis of frozen turbulence, which relates the frequencies to wavenumbers by considering the convection velocity.

The velocity spectrum is the one-sided power spectral density (PSD) of the velocity time series, which can be obtained from the discrete Fourier transform (DFT) of the time series. Several methods exist for the computation of the PSD. As it will be seen later, different PSD computation methods were used in this work depending on the purpose on the examination. In order to explain the differences between them, the following methods are described in this section: calculating the PSD without using a window, calculating the PSD using a windowing function and calculating the PSD using the averaging Welch's method using a windowing function.

The complex DFT coefficients of a time series are defined as (e.g. Pope 2000):

$$C_u(\mathrm{x},\mathrm{y},\mathrm{z},\mathrm{f}_k) = \sum_{n=1}^{N} u(x,y,z,t_n)\cdot e^{-\frac{2\pi ink}{N}}, \qquad -\frac{N}{2} \le k \le \frac{N}{2} \tag{2.13}$$

where the frequency f_k, is obtained as:

$$f_k = \frac{k}{N\cdot\Delta t} \tag{2.14}$$

The one-sided PSD can be computed from the square magnitudes of the DFT as (e.g. Pope 2000):

$$S_{uu}(\mathrm{x},\mathrm{y},\mathrm{z},f_k) = 2\cdot\frac{1}{N}\cdot\Delta t\cdot|C_u(x,y,z,f_k)|^2, \qquad 0 < k \le \frac{N}{2} \tag{2.15}$$

Without going into details of the mathematical background of spectral analysis, the following two essential issues have to be considered when computing the PSD of a turbulent velocity time series: the effects arising from the finite length time series and the high variance of the PSD arising from the randomness of the time series.

The first issue arises because the time series of the measured process is truncated at the ends due to the finite length of the measurement (e.g. Pollock 1999). As a result, jumps appear at the ends of the time series, which lead to false power contributions at several frequencies in the PSD. Note that low frequencies are not affected by this issue.

This effect can be dampened out by applying windowing functions to the time series before calculating the DFT as (e.g. Vaseghi 2000):

$$C_u^{(w)}(x,y,z,f_k) = \sum_{n=1}^{N} u(x,y,z,t_n)\cdot w(n)\cdot e^{-\frac{2\pi ink}{N}}, \qquad -\frac{N}{2} \le k \le \frac{N}{2} \tag{2.16}$$

where *w(n)* is a windowing function of length *N* containing a weight for every time-series element. The power loss caused by the window can be compensated in the PSD as (e.g. Vaseghi 2000):

$$S_{uu}^{(w)}(x,y,z,f_k) = 2\cdot\frac{1}{N}\cdot\frac{1}{W_c}\cdot\left|\mathrm{C}_u^{(w)}(x,y,z,f_k)\right|^2, \qquad 0 < k \le \frac{N}{2} \tag{2.17}$$

where W_c can be calculated as:

$$W_c = \frac{1}{N}\sum_{n=1}^{N} w(n)^2 \tag{2.18}$$

The weights of the windowing function are reduced at the ends of the time series, thereby reducing the effects of the truncation. The reduced power contributions arising due to the reduced fluctuations at the ends are compensated by the correction factor W_c, so that the integral of the PSD yields the total variance. Note that applying a rectangular window provides the same result as calculating the DFT without applying a window function.

It has to be pointed out that PSD estimations using non-rectangular windows can produce biased results as follows. The duration of velocity measurements is usually optimized with respect of time (see Section 2.3.3) so that just the minimal number of large-scale events are captured, which are necessary to produce a measured variance value that is sufficiently converging to the true variance value. Since windowing functions suppress the variance contributions of large-scale events at the beginning and at the end of the time series, the remaining large-scale events in the middle of the time series might be insufficient to obtain a sufficiently converging variance value. For this reason the PSD values at low frequencies become reduced by the windowing.

The second issue, when computing the PSD of a turbulent velocity time series, is the high variance in the PSD arising from the randomness of the velocity time series, which can significantly disturb the clear recognition of the power distribution over the frequencies. This effect can be effectively reduced by applying methods that are averaging the results of several PSDs computed from the given velocity time series. Such an averaging method is Welch's method, which first divides the time series into K overlapping segments, then calculates the PSDs of the windowed segments, and finally averages the obtained PSDs as (e.g. Vaseghi 2000):

$$S_{uu}^{(a,w)}(x, y, z, f_k) = \frac{1}{K}\sum_{i=1}^{K} S_{uu}^{(i,w)}(x, y, z, f_k) \tag{2.19}$$

where $S_{uu}^{(i,w)}$ is the PSD of the i-th segment calculated according to Eqs. (2.16) and (2.17).

On the one hand, the higher the number of the segments is, the smoother is the PSD. On the other hand, smooth results are produced on the cost of frequency resolution, so that distinct peaks at frequencies near to each other tend to merge to single peaks with increasing number of segments. It has to be highlighted that the previously described bias effect arising from the windowing, which affects the low frequency contributions, also applies for this method, however, it is expected to be significantly lower, because the windowing is applied to each segments of the time series.

In the present work the power spectra were calculated using MATLAB 2011b, which computes the DFT using the fast Fourier transform (FFT) algorithm called FFTW (Frigo et al. 1998). The segment overlap used for the computation of the PSD by Welch's method was always 50 %, but the number of segments was varied as will be highlighted later in this section. The windowing function used was the Blackman-Harris window (Harris 1978), which is composed of cosine elements expected to introduce the least possible false frequencies to the PSD and is defined as:

$$w(n) \quad = a_0 - a_1\cos\left(\frac{2\pi(n-1)}{N}\right) + a_2\cos\left(\frac{4\pi(n-1)}{N}\right) - a_3\cos(\frac{6\pi(n-1)}{N}) \tag{2.20}$$

where $a_0 = 0.35875$, $a_1 = 0.48829$, $a_2 = 0.14128$ and $a_3 = 0.01168$.

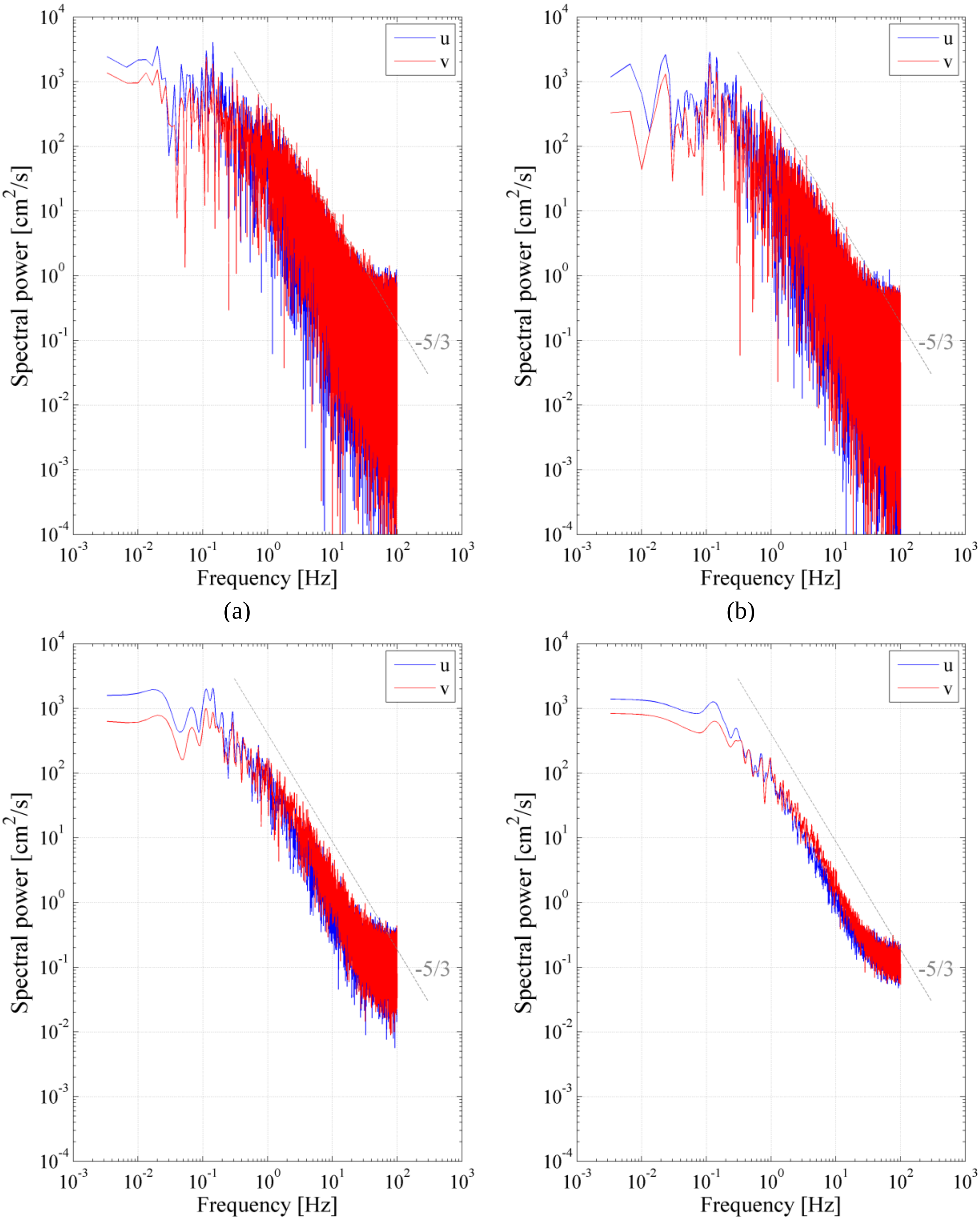

(a) (b)

(c) (d)

Figure 2.4 Velocity spectra of a measured velocity time series obtained by different methods: (a) PSD without using a window, (b) PSD using a Blackman-Harris window, (c) PSD computed by Welch's method using Blackman-Harris window and 4 time-series segments, (d) PSD computed by Welch's method using Blackman-Harris window and 12 time-series segments.

In order to illustrate the differences arising from the different methods, the PSDs of a measured velocity time series were computed by each of the methods described in this section and are displayed in Figure 2.4. Figure 2.4 (a) shows the velocity spectra calculated without using a windowing function according to Eqs. (2.13) and (2.15). Here, although the PSD values corresponding to low frequencies are correct, it can be expected that false power contributions are contained at higher frequencies and the spectra calculated this way show high variance. Figure 2.4 (b) displays the velocity spectra calculated based on Eqs. (2.16) and (2.17) by using a Blackman-Harris window. The impact of the windowing on the velocity spectra can be observed in the PSD values at low frequencies, where some values are significantly reduced. Figures 2.4 (c) and (d) show the PSDs computed by Welch's method according to Eq. (2.19) using $K = 4$ and $K = 16$ segments, respectively. It can be well observed that the high variance in the spectra is effectively reduced by increasing the number of segments, so that the power distribution over frequency becomes clearer. On the other hand, smooth results are produced on the cost of frequency resolution, which can be well recognized in the frequency range 0.1-0.2 Hz, where the two distinct frequency contributions in Figure 2.4 (c) are fused to a single "peak" in Figure 2.4 (d).

Note that, in contrast to the power distribution expected according to Figure 2.3, the power contributions stop decreasing with increasing frequency at about 50 Hz in Figure 2.4. This can be considered as the measurement noise and will be revisited in Section 4.3.5.

These examples point out that the method to use for the PSD estimation depends on the examined frequency range and on the objective of the examination. If the power contributions of the lowest frequencies are needed, the PSD without using a window has been used; if peaks have to be identified at low frequencies, the PSD computed by Welch method using low number of segments was used; and if the contributions of the highest frequencies are in focus, the PSD computed by Welch method using high number of segments was used.

2.3.3 Convergence analysis of measured statistical quantities

As discussed previously, the statistical description of turbulence is essential because the statistical quantities of the fluctuations are well reproduced by different realizations of the flow, even though the temporal sequence of the fluctuations is not reproducible in detail. Due to the randomness of the fluctuations, however, the strictly accurate, true statistical quantities would only be achievable by infinite number of measured samples, which is not practicable.

The statistical quantities derived from a finite number of samples always deviate from the true quantities to some extent. For this reason, the quantities derived from measurements are called estimations and the computational algorithms applied to obtain them are called estimators. Note that all of the computation methods presented in Section 2.3 are estimators.

Since only a finite number of samples are collected during a finite length measurement, it has to be ensured that the collected number of samples is sufficient for obtaining statistical features that properly characterize the measured flow. The convergence analysis of the measured statistics has the aim to reveal whether the number of samples is sufficient, hence, in the present work, whether the measurement duration is long enough. Considering that the true value of the statistical quantities is unknown, the convergence analysis of the measured statistics comprises, firstly, whether the statistical values obtained by the measurement converge over the measurement time and, secondly, the estimation of the error arising from the finite measurement duration.

The convergence of the measured quantities was examined in the present work using cumulative statistical functions, which show the change of the statistical quantities with increasing duration, hence cumulated measurement time. If the measurement duration is large enough, the cumulative statistical functions converge.

The cumulative mean function *CMF* and the cumulative variance functions *CVF*, which show the change of the mean and variance values with increasing measurement duration, can be calculated for the individual velocity components as follows:

$$CMF_u(x,y,z,t_k) = \frac{1}{k} \cdot \sum_{n=1}^{k} u^{i}\ (x,y,z,t_n) \tag{2.21}$$

$$CVF_u(x,y,z,t_k) = \frac{1}{k} \cdot \sum_{n=1}^{k} (u'\ (x,y,z,t_n))^2 \tag{2.22}$$

where $k = 1,2,3,\ldots,N$. Note that the final value of these functions at $k = N$, give the mean value according to Eq. (2.7) and the variances according to Eq. (2.10), respectively.

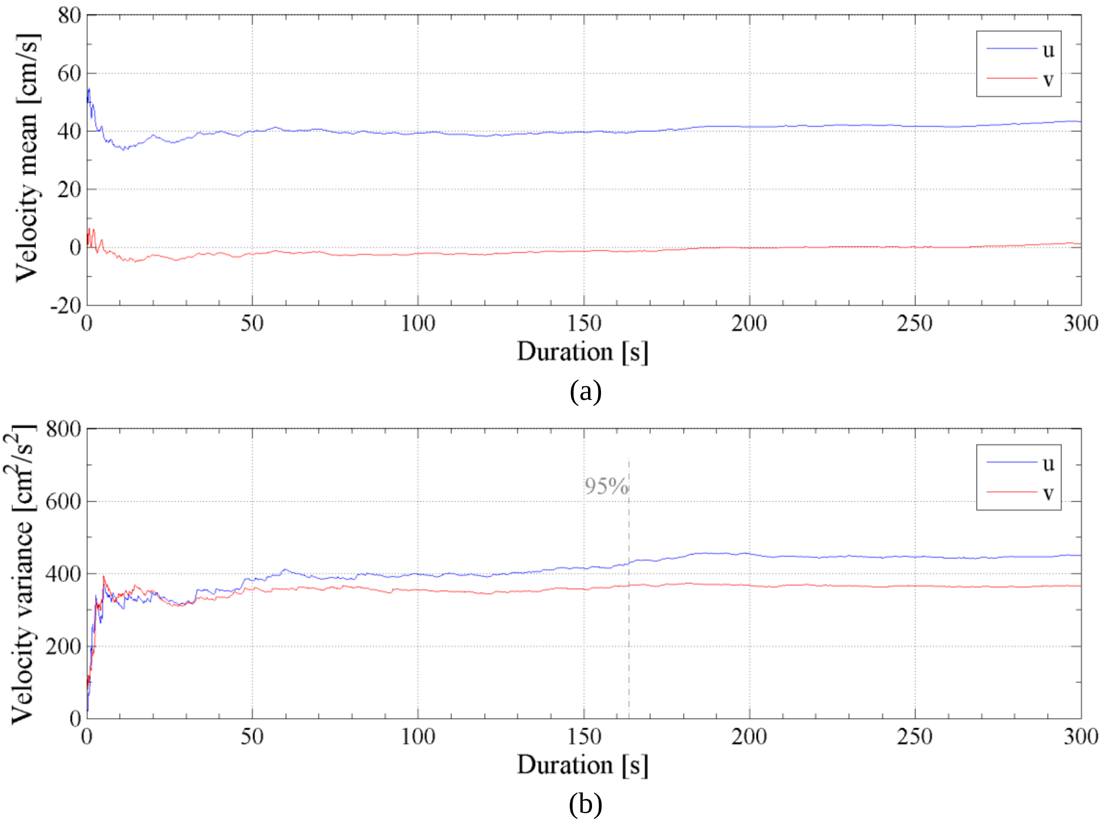

Figure 2.5 The (a) cumulative mean function and the (b) cumulative variance function of a velocity time series for the *u* and *v* components. The dashed line marks the 95%-durations of the variance.

Figure 2.5 exemplarily shows the cumulative mean and cumulative variance functions of both the *u* and the *v* velocity components of a measured velocity time series. Although it can be recognized based on these functions, whether the displayed statistical quantities converge, the visual inspection of these functions in every grid point is impracticable at high numbers of grid points. In order to obtain a more compact representation of the convergence characteristics, the following indicator of the convergence can be computed.

The duration $t^{(95\%)}$, after which the variance has at least 95% of the final variance value, can be given as:

$$CVF_u(x,y,z,t_k) > 0.95 \cdot CVF_u(x,y,z,t_N), \ \text{ for } t_k \geq t^{(95\%)} \tag{2.23}$$

which is:

$$CVF_u(x,y,z,t_k) > 0.95 \cdot VAR_u(x,y,z), \quad \text{for } t_k \geq t^{(95\%)} \tag{2.24}$$

This indicator is called *95%-duration* in this work. High values of the 95%-duration with respect to the applied measurement duration mean that the variance changed more than 5% in the last time-segment of the measurement, which indicate that the applied measurement duration might be too short for the good convergence of the measured variance. Note that this indicator was not determined for the mean values, because locations with mean velocities near to 0 result in misleading high 95%-durations.

The error arising from the finite measurement duration cannot be quantified based on these cumulative statistical functions, since the true values of the mean and the variance are unknown. As described before, the statistical quantities obtained from the measurement are estimations, which deviate from the true statistical quantities due to the finite length measurement.

The error of the estimation with respect to the true quantity can be derived analytically as shown in e.g. Tropea et al. (2007). Note that the estimated error is to be considered as the standard deviation of the measured quantity with respect to the true quantity. By dividing this error by the measured quantity, the normalized error can be obtained (Bendat et al. 2000). Accordingly, the normalized mean error of the measured mean values and the normalized mean error of the measured variances can be estimated as:

$$\epsilon_{(u^m)}(x,y,z) = \frac{1}{u^m(x,y,z)}\sqrt{\frac{2 \cdot \tau_{I,u}(x,y,z)}{T} \cdot VAR_u\ (x,y,z)^2} \tag{2.25}$$

$$\epsilon_{(VAR_u)}(x,y,z) = \frac{1}{VAR_u(x,y,z)}\sqrt{\frac{2 \cdot \tau_{I,u}(x,y,z)}{T} \cdot \left(\mu_{4,u}(x,y,z) - VAR_u\ (x,y,z)^2\right)} \tag{2.26}$$

where $\tau_{I,u}$ is the integral time scale and T is the duration of the measurement.

The integral time scale is usually computed from the autocorrelation function of the time series; however, due to the randomness of the fluctuations, the obtained values often show a considerable variability. For this reason, the integral time scales were deduced in the present work from the velocity spectra as (e.g. Pope 2000):

$$\tau_{I,u}(x,y,z) = \frac{\pi}{2} \cdot \frac{S_{uu}(\mathrm{x,y,z,0})}{VAR_u(x,y,z)} \tag{2.27}$$

where $S_{uu}(x,y,z,0)$ is the value of the velocity spectrum at 0 Hz, which was approximated by the first available value of the velocity spectrum, since the velocity spectrum does not have a value a $f = 0$ Hz. In order to achieve the best possible estimation, the velocity spectrum used for this calculation was the PSD without using a windowing function according to Eqs. (2.13) and (2.15), since the PSD values at low frequencies are not affected by the windowing using this method.

Note that both normalized errors in Eqs. (2.25) and (2.26) are themselves estimations, because the true statistical quantities (variance, 4-th order moments and integral time scales) needed to calculate them are unknown, so that the available estimations of the required statistical quantities have to be used.

2.4 Spatial features of vector fields

If the spatial structures formed by vectors of a vector field are of similar size, so that the field is homogeneous, the characteristic length scale of the structures can be estimated based on the spatial autocorrelation-coefficient functions of the vector field.

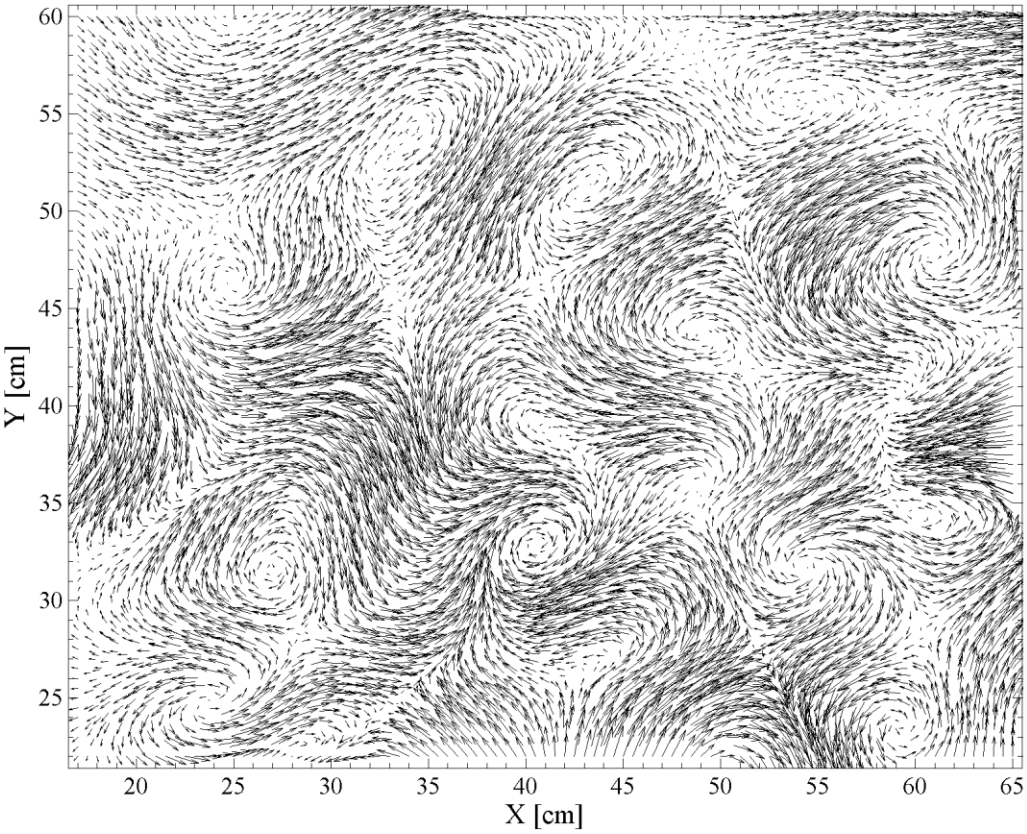

Figure 2.6 A vector field containing vortical structures of similar size.

The x-directional and y-directional spatial autocorrelation-coefficient functions of the v and the u velocity fields ($SACF_x$ and $SACF_y$) can be computed as:

$$\mathbf{SACF}_x(x_{lag}) = \left(\sum_{x=x_1}^{x_e - x_{lag}} \sum_{y=y_1}^{y_e} v^{sf}(x,y) \cdot v^{sf}(x + x_{lag}, y) \right) \Big/ \sum_{x=x_1}^{x_e} \sum_{y=y_1}^{y_e} v^{sf}(x,y) \cdot v^{sf}(x,y)$$

$$\mathbf{SACF}_y(y_{lag}) = \left(\sum_{x=x_1}^{x_e} \sum_{y=y_1}^{y_e - y_{lag}} u^{sf}(x,y) \cdot u^{sf}(x, y + y_{lag}) \right) \Big/ \sum_{x=x_1}^{x_e} \sum_{y=y_1}^{y_e} u^{sf}(x,y) \cdot u^{sf}(x,y) \tag{2.28}$$

where u^{sf} and v^{sf} are the spatial fluctuations of the u and v velocity components (after removing the whole-field spatial mean values), x_1 and y_1 are the smallest x and y coordinates, x_e and y_e are the largest x and y coordinates, x_{lag} and y_{lag} are the spatial lags in x and y directions.

The x-directional and y-directional characteristic length scales of the vector field ($L_{C,x}$ and $L_{C,y}$) are obtained as the first spatial lag resulting in zero correlation, hence the zero crossing of the SACF.

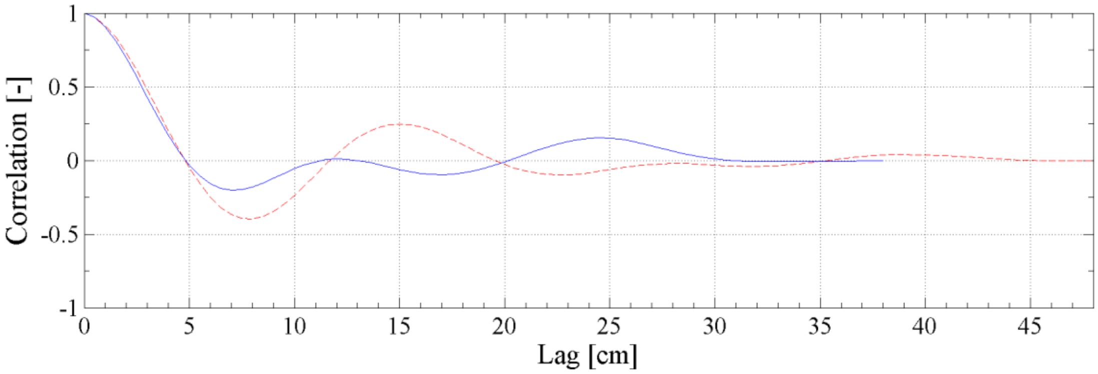

Figure 2.7 The spatial autocorrelation-coefficient functions of the vector field: SACF$_x$ (red, dashed) and SACF$_y$ (blue, solid)

Figure 2.7 shows the SACFs of the vector field displayed in Figure 2.6. It can be recognized that the lags of the first zero-crossings in ($L_{C,x}$~ 5 cm, $L_{C,y}$~5 cm) correspond approximately to the average radius of the vortical structures to be observed in the vector field. Note that the accuracy of the values depends on the spatial resolution of the velocity data and that this simple estimation works well only if the structures in the vector field are of similar size.

2.5 Spatio-temporal analysis by Proper Orthogonal Decomposition (POD)

The Proper Orthogonal Decomposition (POD) is a method that is suitable to be applied on velocity datasets with inhomogeneous flow fields (e.g. Adrian et al. 2000).

Since the review of the mathematical background of POD is beyond the scope of this work, only a very brief description of POD and the equations needed to compute POD are presented in this section. Further information about the method can be found in e.g. Lumley (1967), Sirovich (1987), Aubry (1991), Cordier (2003), Meyer et al. (2007), Kriegseis et al. (2010).

From mathematical point of view, POD creates a set of orthonormal basis functions for the input velocity dataset, so that each individual time step of the input dataset can be reconstructed using these new basis functions, called POD modes. An important property of POD is that it calculates the basis functions from the input velocity dataset without need for assumptions about the flow. Further, the POD modes are optimal in terms of variance representation, which means that the POD modes with highest contribution to the ensemble turbulent kinetic energy are the first modes. For these reason the most energetic and largest structures of the flow are usually represented by the first POD modes, so that largest structures can be usually investigated using the first few modes.

In order to compute POD, the velocity dataset has to be arranged in a specific form. First, the mean velocity field of the dataset, which is considered as POD mode 0, is subtracted from the dataset at the beginning, so that the following steps are done using only the fluctuating parts of the velocity.

The typical velocity dataset of a PIV measurement contains two- (or three-) dimensional velocity vectors (u, v; w) in M positions of the measurement grid for N time steps. Such a velocity dataset can be arranged in a matrix of size 2MxN (or 3MxN in case of three-dimensional data) as follows:

$$\mathbf{X} = \begin{bmatrix} u'(p_1,t_1) & u'(p_1,t_2) & \cdots & u'(p_1,t_N) \\ u'(p_2,t_1) & u'(p_2,t_2) & \cdots & u'(p_2,t_N) \\ \vdots & \vdots & \vdots & \vdots \\ u'(p_M,t_1) & u'(p_M,t_2) & \ldots & u'(p_M,t_N) \\ v'(p_1,t_1) & v'(p_1,t_2) & \cdots & v'(p_1,t_N) \\ \vdots & \vdots & \vdots & \vdots \\ v'(p_M,t_1) & v'(p_M,t_2) & \ldots & v'(p_M,t_N) \\ w'(p_1,t_1) & w'(p_1,t_2) & \cdots & w'(p_1,t_N) \\ \vdots & \vdots & \vdots & \vdots \\ w'(p_M,t_1) & w'(p_M,t_2) & \cdots & w'(p_M,t_N) \end{bmatrix} = [\mathbf{x}^1 \cdots \mathbf{x}^n \cdots \mathbf{x}^N] \tag{2.29}$$

where the column vectors $\mathbf{x}^n$ contain the velocities of the individual time steps t_n and the row vectors contain the time series of a component in the individual grid point p_m located in (x_m, y_m, z_m).

POD is calculated based on the auto-covariance matrix of the velocity data matrix **X**. According to whether the auto-covariance matrix is computed as $\mathbf{XX}^\mathrm{T}$ or as $\mathbf{X}^\mathrm{T}\mathbf{X}$, the approaches Classical POD (also called Direct POD) and Snapshot POD can be distinguished, respectively. As the snapshot POD approach consists of more steps than the classical approach, first the steps of the snapshot approach are presented, and then the connection to the classical approach is highlighted.

The auto-covariance matrix of the velocity data matrix is created as:

$$\mathbf{C} = \mathbf{X}^\mathrm{T}\mathbf{X} \tag{2.30}$$

The corresponding eigenvalue problem to solve is:

$$\mathbf{C\Psi} = \mathbf{D\Psi} \tag{2.31}$$

where the diagonal matrix **D** contains the eigenvalues λ'_i ordered in descending order:

$$\mathbf{D} = \begin{bmatrix} \lambda'_1 & & & & 0 \\ & \ddots & & & \\ & & \lambda'_i & & \\ & & & \ddots & \\ 0 & & & & \lambda'_N \end{bmatrix} \tag{2.32}$$

and the columns of $\mathbf{\Psi}$ contain the temporal eigenvectors of the velocity data matrix. These eigenvectors are orthogonal and are used as basis to construct the corresponding POD modes as follows. First, spatial vectors are computed as:

$$\mathbf{\Phi}' = \mathbf{X\Psi} = [\mathbf{\Phi}'^{\mathbf{1}} \cdots \mathbf{\Phi}'^{\boldsymbol{i}} \cdots \mathbf{\Phi}'^{\boldsymbol{N}}] \tag{2.33}$$

where the columns of **Φ'** are orthogonal vectors and have to be normalized by their Euclidean norms as:

$$\mathbf{\Phi}^{\boldsymbol{i}} = \frac{\mathbf{\Phi}'^{i}}{\|\mathbf{\Phi}'^{i}\|}. \tag{2.34}$$

The obtained column vectors $\mathbf{\Phi}^\mathbf{i}$ are the orthonormal POD modes and are the spatial eigenvectors of the velocity data matrix **X**:

$$\mathbf{\Phi} = [\mathbf{\Phi}^{\mathbf{1}} \cdots \mathbf{\Phi}^{\boldsymbol{i}} \cdots \mathbf{\Phi}^{\boldsymbol{N}}] \tag{2.35}$$

Due to the normalization of the column vectors $\mathbf{\Phi}'^{\mathbf{i}}$, the correction of the corresponding temporal eigenvectors is necessary. Instead of calculating weighting factors for each eigenvector separately, it is more practical to extract the correct temporal vectors, called POD coefficients, using the orthonormal POD modes as:

$$\mathbf{A} = \mathbf{\Phi}^{\mathrm{T}}\mathbf{X} = [\mathbf{a}^1 \cdots \mathbf{a}^n \cdots \mathbf{a}^N] = \begin{bmatrix} \mathbf{a}_1 \\ \vdots \\ \mathbf{a}_i \\ \vdots \\ \mathbf{a}_N \end{bmatrix}, \tag{2.36}$$

where POD coefficients in the column vector $\mathbf{a}^{\mathbf{n}}$ contain the coefficients corresponding to the individual POD modes at time step *n*, and the POD coefficients in the row vector $\mathbf{a}_{\mathbf{i}}$ contain the time series of coefficients over the time steps 1..*n*..*N* corresponding to POD mode *i*. Considering the modified POD coefficients, the adjusted values of λ_i can be calculated as the variance of the time series as:

$$\lambda_i = \mathrm{VAR}(\mathbf{a}_{\mathbf{i}}) \tag{2.37}$$

The ensemble velocity variance produced by POD mode *i* is equivalent to λ_i. The contribution of the POD mode *i* to the ensemble variance of the input velocity dataset can be obtained as the normalized lambda values:

$$p_i = \frac{\lambda_i}{\|\lambda\|} \tag{2.38}$$

which is equivalent contribution of the POD mode *i* to the ensemble turbulent kinetic energy of the input velocity dataset.

Further, the sum of the coefficients in the row vector $\mathbf{a}_{\mathrm{i}}$ belonging to the POD mode *i* is per definition zero:

$$\sum_{j=1}^{N} a_{i,j} = 0$$

The input velocity dataset including every time step can be reconstructed as the sum of the products of the POD modes and the corresponding POD coefficients:

$$\mathbf{X} = \mathbf{\Phi}\mathbf{A} = [\mathbf{\Phi}^{\mathbf{1}} \cdots \mathbf{\Phi}^{i} \cdots \mathbf{\Phi}^{N}] \begin{bmatrix} \mathbf{a}_1 \\ \vdots \\ \mathbf{a}_i \\ \vdots \\ \mathbf{a}_N \end{bmatrix} \tag{2.40}$$

The reconstruction of a limited number of time steps is possible by involving only the needed time steps of each time series $\mathbf{a}_{\mathbf{i}}$ in the reconstruction. If some of the POD modes are excluded during the reconstruction, the resulting dataset is not an exact reconstruction of the original dataset.

According to the Classical POD approach, the auto-covariance matrix is computed as:

$$\mathbf{R} = \mathbf{X}\mathbf{X}^{\mathrm{T}}, \tag{2.41}$$

and the eigenvalue problem can be written as:

$$\mathbf{R\Phi} = \mathbf{D\Phi}, \tag{2.42}$$

where the diagonal matrix **D** contains the eigenvalues λ_{i} and the columns of $\mathbf{\Phi}$ are the orthonormal spatial eigenvectors of the velocity data matrix, which are the POD modes. Thus, the orthonormal POD modes can be obtained directly as the eigenvectors of $\mathbf{X}\mathbf{X}^{\mathrm{T}}$ without needing the calculations in Eqs. (2.33) to (2.35).

The difference between the two approaches is that Snapshot POD computes the POD results based on the two-point temporal correlation tensor obtained as $\mathbf{X}^{\mathrm{T}}\mathbf{X}$, whereas Classical POD computes the POD results based on the two-point spatial correlation tensor received as $\mathbf{X}\mathbf{X}^{\mathrm{T}}$ (Figure 2.8). The two approaches yield, however, the same POD modes and POD coefficients. The number of modes is the smallest dimension of the velocity data matrix regardless of the approach used, hence in case of two-dimensional velocity data min(N, $2M$) defines the valuable amount of data in the results.

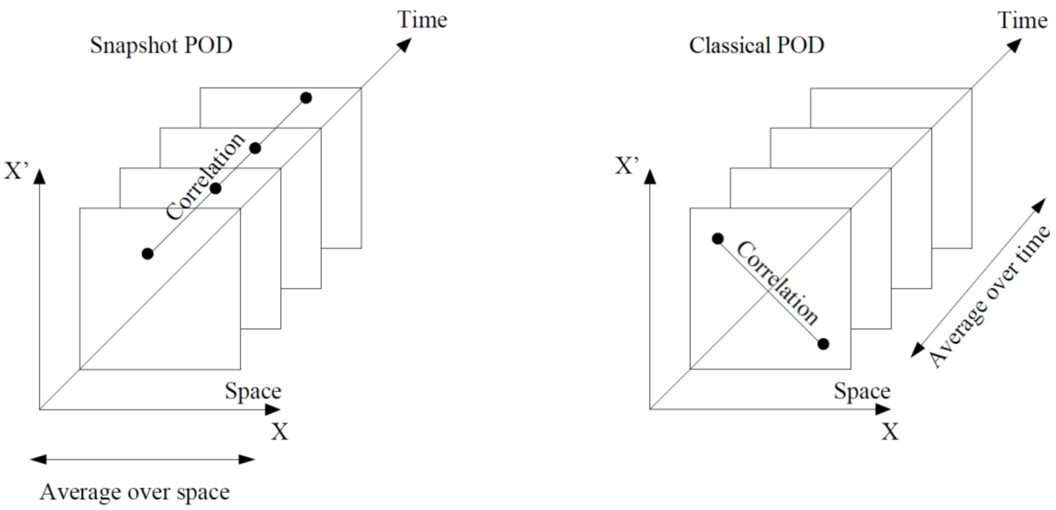

(a) (b)

Figure 2.8 Schematic view of the (a) Snapshot POD and (b) Classical POD (after Cordier 2003).

An essential difference between the computations of the two approaches is the size of the eigenvalue problem, which is determined by the size of the auto-covariance matrix, i.e. NxN for Snapshot POD and $2M$x$2M$ for Classical POD. If N is significantly smaller than $2M$, the computational cost of using Snapshot POD is lower. Therefore, the approach to use is to be decided on the basis of the size of the available velocity data matrix.

Note that one can obtain the eigenvectors in Eqs. (2.31) and (2.42) by Singular Value Decomposition as:

$$\mathbf{X} = \mathbf{\Phi} \mathbf{S} \mathbf{\Psi}^{\mathrm{T}} \tag{2.43}$$

where the left singular vectors in $\mathbf{\Phi}$ are the eigenvectors of $\mathbf{X}\mathbf{X}^{\mathrm{T}}$ as in Eq. (2.42) of Classical POD, the right singular vectors in $\mathbf{\Psi}$ are the eigenvectors of $\mathbf{X}^{\mathrm{T}}\mathbf{X}$ as in Eq. (2.31) of Snapshot POD, and $\mathbf{S}^2=\mathbf{D}$ (Cordier 2003). The use of Singular Value Decomposition to compute the spatial and temporal eigenvectors is also called Biorthogonal Decomposition.

A POD analysis usually focuses on the POD modes with the largest energy contributions and on the examination of the characteristics of corresponding time series of POD coefficients. However, an individual POD mode is by itself not an extracted flow structure, but rather a spatial oscillation component, which will be demonstrated in Chapter 5.

Most studies that managed to describe flow structures using POD have identified the POD modes necessary for the reconstruction based on connections between individual POD modes. Such connections are, for example, the almost identical energy contributions of POD modes and the identical dominant frequencies of POD coefficients corresponding to connected POD modes (e.g. Bernero et al. 2000, Meyer et al. 2007, Feng et al. 2011). In addition, the POD modes used in such studies are the very first modes representing the large flow structures, which could also be recognized and verified visually.

3 Literature review on the hydraulics of vertical-slot fish passes

A vertical-slot fish pass consists of a rectangular open channel divided into a series of pools by cross walls (Figure 3.1). The pools are interconnected by vertical slots established in the cross walls, where water can flow through from pool to pool. This arrangement divides the large water level difference between the headwater and the tailwater of the barrage into small water level differences between the pools which can be surmounted by fish.

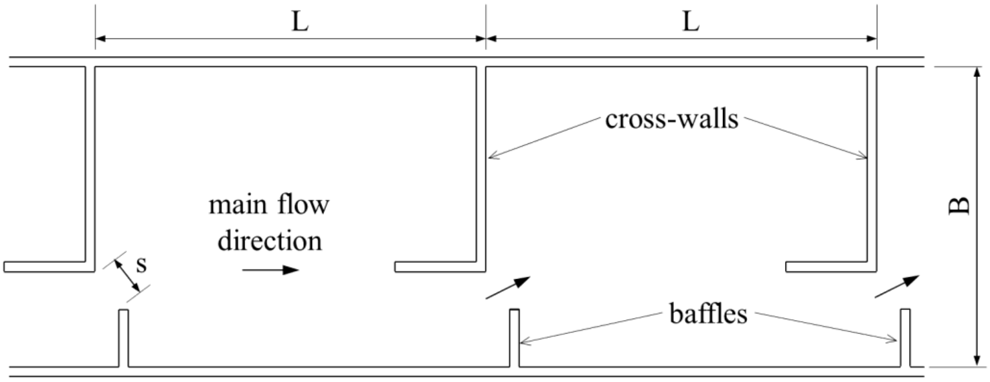

Figure 3.1 Plan view of typical pools of a vertical-slot fish pass with the main denotations

Due to the limited space near barrages, such fish passes often have a folded layout, where irregular pools (e.g. turning pools) serve as connection of the straight sections. Though, the majority of pools are regular pools in a straight layout, hence most scientific investigations in the literature cope with the flow in the straight sections neglecting the influence of irregular pools on the hydraulics of the straight sections. Since the present investigation also deals with regular pools, the literature review in this section focuses on results gained in vertical-slot fish passes of identical pools in a straight layout.

For the following review it has to be pointed out that the uniform flow condition for such arrangements is defined so that the water depths and flow velocities are identical in each pool (see e.g. Rajaratnam et al. 1986), even though they are not identical within the pools. Further, the slot geometry is considered to be part of the pool geometry, so that pools with the same pool dimensions but with differences in any other geometric element are considered as different pool geometries.

3.1 Hydraulic performance of the vertical-slot fish pass

Current fish pass design guidelines (e.g. DWA 2014) define design criteria based on the overall hydraulic performance of the vertical-slot fish pass, which consists of a one-dimensional description of the hydraulics involving the relation between the water depth and the discharge, the maximum flow velocity in the pools and an average measure for the level of turbulence in the pools. These hydraulic characteristics are fundamental for hydraulic design and have accordingly been objects of numerous hydraulic investigations in the past.

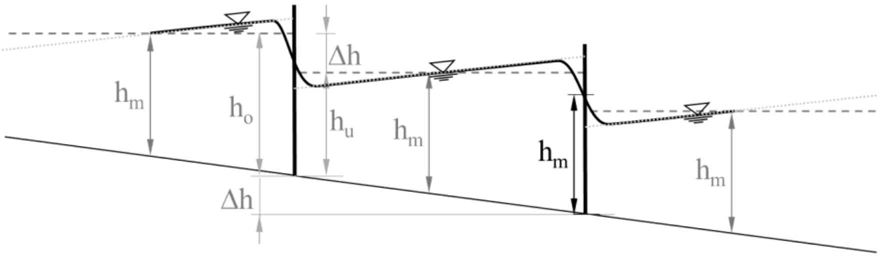

Figure 3.2 Schematic view of the water levels within the pools (solid line) and the assumption of a horizontal water surface (dashed line). (after Sokoray-Varga et al. 2015)

An essential parameter for the equations of these hydraulic characteristics is the nominal head drop at the cross walls of subsequent pools Δh, which is calculated by assuming horizontal water surfaces within the pools (Figure 3.2). The nominal head drop divided by the pool length is regarded as the slope parameter of the fish pass. In case of uniform flow, the nominal head drop is equal to the bottom level difference between subsequent pools.

In contrast to the assumption of a horizontal water surface within the pools, experimental results have revealed (e.g. Rajaratnam et al. 1986, Wu et al 1999, Puertas et al. 2004) that the water surface is not horizontal in reality but it tends to increases from a minimum level behind the upstream cross wall of the pool to a maximum level in front of the downstream cross wall (Figures 3.2 and 3.3). The tilt of the water surface within the pools has been later found to be geometry specific and dependent on the slope, but independent of the discharge (Puertas et al. 2004).

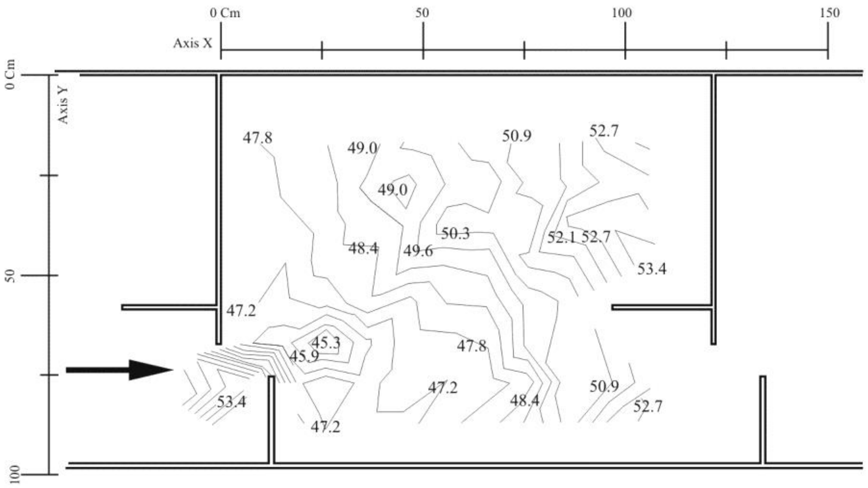

Figure 3.3 Distribution of the average water levels within a pool (after Puertas et al. 2004)

The relationship between the mean depth in the pools and the discharge in the fish pass has been shown to be linear for uniform flow in previous experimental investigations (Rajaratnam et al. 1986, Rajaratnam et al. 1992, Wu et al. 1999 and Puertas et al. 2004). These studies involved 20 different pool geometries at different slopes and discharges, and the resulting depth-discharge equations can be expressed as (Sokoray-Varga et al. 2015):

$$Q = \alpha \cdot \sqrt{\frac{s}{2 \cdot L}} \cdot h_m \cdot s \cdot \sqrt{2 \cdot g \cdot \Delta h} \tag{3.1}$$

where α is a pool geometry dependent coefficient, h_m is the mean depth in the pools, s is the slot width, Δh is the nominal head drop between subsequent pools, L is the pool length and g is gravity. The coefficient α proved to be essentially dependent on the geometry of the pool but to be constant for different discharges for uniform flow conditions, which results in the linear relationship between discharge and flow depth. Puertas et al. (2004) have detected a slight dependence of α on the slope.

Wang et al. 2010 suggested using the following equation:

$$Q = C_{md} \cdot h_m \cdot s \cdot \sqrt{2 \cdot g \cdot \Delta h} \tag{3.2}$$

where h_m is the mean water depth in the pools, and C_{md} is the discharge coefficient being only slightly dependent on the slope. The link between Eqs. (3.1) and (3.2) can be given as:

$$C_{md} = \frac{\alpha}{\sqrt{2}} \cdot \sqrt{\frac{s}{L}} \tag{3.3}$$

It has to be noted that there also exist further equations for the depth-discharge relationship, which, however do not make use of linearity (e.g. Rajaratnam et al. 1986, Larinier 1992, DVWK 1996, DWA 2010, Krüger et al. 2010, DWA 2014, Fuentes-Peres et al. 2014).

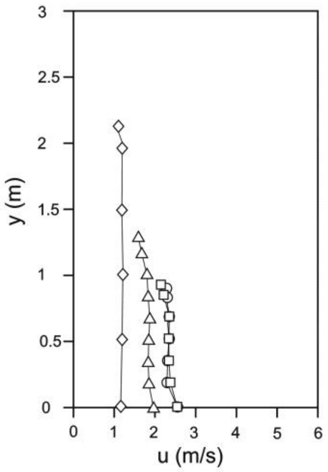

Figure 3.4 Vertical distribution of the flow velocities measured within the slots of different pool geometries (after Rajaratnametal1986)

The experimental investigations of Rajaratnam et al. (1986), Wu et al. (1999), Puertas et al. (2004) and Liu et al. (2006) found that the maximal flow velocity in the slot is approximately:

$$v_{max,s} = \sqrt{2 \cdot g \cdot \Delta h} \tag{3.4}$$

Their measurements have demonstrated that the maximal velocity in the slot is independent of the discharge and is essentially the same in different distances above the bottom – except near the surface and near the bottom (Figure 3.4). This explains the linear depth-discharge relationship in Eq. (3.2).

3.2 Velocity distribution in the pools

The investigations mentioned previously (Rajaratnam et al. 1986, Wu et al. 1999, Puertas et al. 2004, Wang et al. 2010) have demonstrated that the mean flow velocities within the pools and the slots of vertical-slot fish passes are essentially the same in different distances above the bottom (except near the surface and near the bottom), hence there are no significant differences in the horizontal velocity fields in different heights. The vertical velocity component has been shown to be generally small within the pools compared to the other components in these studies. The vertical velocity component obtained higher values only near the slots; in most parts of the pools it proved to be typically higher for slopes over 5% and was observed to be negligibly small for lower slopes. Additionally, the flow velocities in vertical-slot fish passes have been found to be independent of the discharge. The linear relationship found between the water depth and the discharge in Eq. (3.1) and (3.2) confirms these findings.

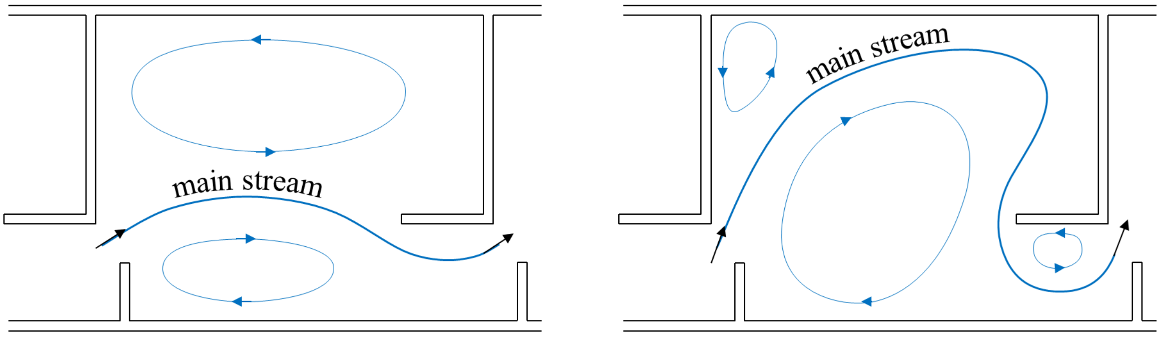

(a) (b)

Figure 3.5 Typical positions of the main streams (thick lines) and recirculation flows (thin lines) in the pools of vertical-slot fish passes: (a) flow pattern 1, (b) flow pattern 2.

These investigations have also shown that the horizontal velocity distribution in the pools consists of two types of flow regions: a main stream and several recirculation regions (Figure 3.5). The main stream is the jet-like stream traveling along a curved trajectory from the upstream slot to the next in the pool. It is characterized by high flow velocities, which decay along the trajectory but still stay higher than in the recirculation regions. The flow velocities have been observed to be even higher within the main stream at some distance below the slot than within the slot (Wu et al. 1999, Wang et al. 2010), but no equation has been found for its value so far. The recirculation regions are shear driven by the main stream and are characterized by circulations of lower flow velocities. The extents and locations of these flow regions vary in function of the specific pool geometry, however, two typical arrangements of flow regions have been observed, which are referred to as flow patterns (e.g. Wu et al. 99, Puertas et al. 2004, Liu et al. 2006, Tarrade et al. 2008, Wang et al. 2010, Höger et al. 2014).

Flow pattern 1 is characterized by a slightly curved main-stream trajectory and large recirculation regions on both sides of the main stream (Figure 3.5 a). Flow pattern 2 is characterized by a rounded main-stream trajectory that travels from the upstream slot toward the side wall of the pool and then to the next slot, so that one large recirculation region develops (Figure 3.5 b). Beside the large recirculation regions, several smaller recirculation regions can occur in case of both flow patterns.

Recent experimental studies have shown that the type of flow pattern depends on the pool geometry and the slope of the fish pass. However, it is currently not been finally clarified yet how large the influence of individual geometry parameters is (Wang et al. 2010, Höger et al. 2014).

3.3 Turbulence characteristics in the pools

The potential energy represented by the head drop between the pools is dissipated in every pool by turbulent mixing of the main stream, which results in a highly turbulent flow within the pools. Since turbulence had been recognized as influencing fish swimming performance long ago, its quantification has been an objective of hydraulics investigations from the beginning of fish pass research. Though, the methods used for characterizing turbulence have evolved with the development of measurement techniques.

The rate of dissipated energy per unit pool volume is a calculated measure of turbulence in the pools, which has been used since early studies on fish passes (e.g. Rajaratnam et al. 1986, Larinier 1992). It is computed as:

$$E_D = \frac{\rho \cdot g \cdot Q \cdot \Delta h}{L \cdot B \cdot h_m} \tag{3.5}$$

where ρ the density of water and B is the pool width. The value of E_D proved to be independent of the discharge in later studies (Wu et al. 1999, Puertas et al. 2004). Although this pool average value is still widely used as fish pass design criterion by considering thresholds for the target fish species (DWA 2014), the interpretation of this value with regard to the features of turbulence is unclear.

The determination of turbulence features by measurements became possible as velocity time series could be captured at high enough frequencies as a result of the developments in the flow velocity measurement technology, especially the appearance of Acoustic Doppler Velocimeters (ADV) and Particle Image Velocimetry (PIV).

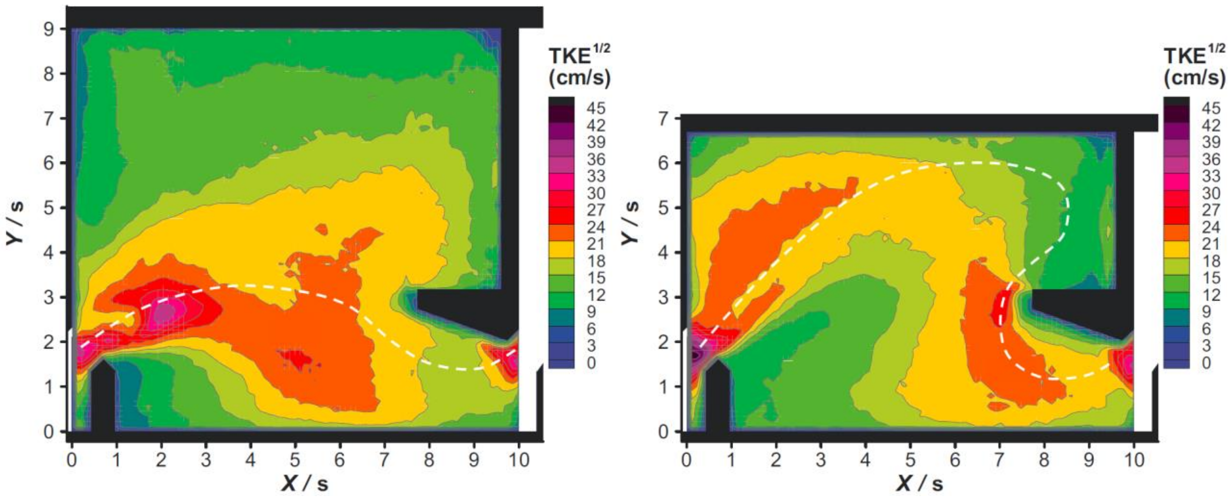

(a) (b)

Figure 3.6 Distributions of $(TKE_{uv})^{1/2}$ in pools with different geometries. The dashed lines illustrate the approximate centerline of the main stream based on the mean velocity fields (after Wang et al. 2010 and Tarrade et al. 2008).

Turbulent kinetic energy (TKE) measurements in vertical-slot fish passes (e.g. Puertas et al. 2004, Liu et al. 2006, Wang et al. 2010) have demonstrated that the maximum TKE levels occur near the slots, which decrease along the main stream. Within the pools, high TKE levels arise in the shear zones between the main stream and the recirculation regions, whereas other parts of the pool are characterized by lower TKE levels (e.g. Figure 3.6). Further, the TKE has been found to be independent of the distance from the bottom and to be only weakly affected by discharge variations (Puertas et al. 2004, Wang et al. 2010).

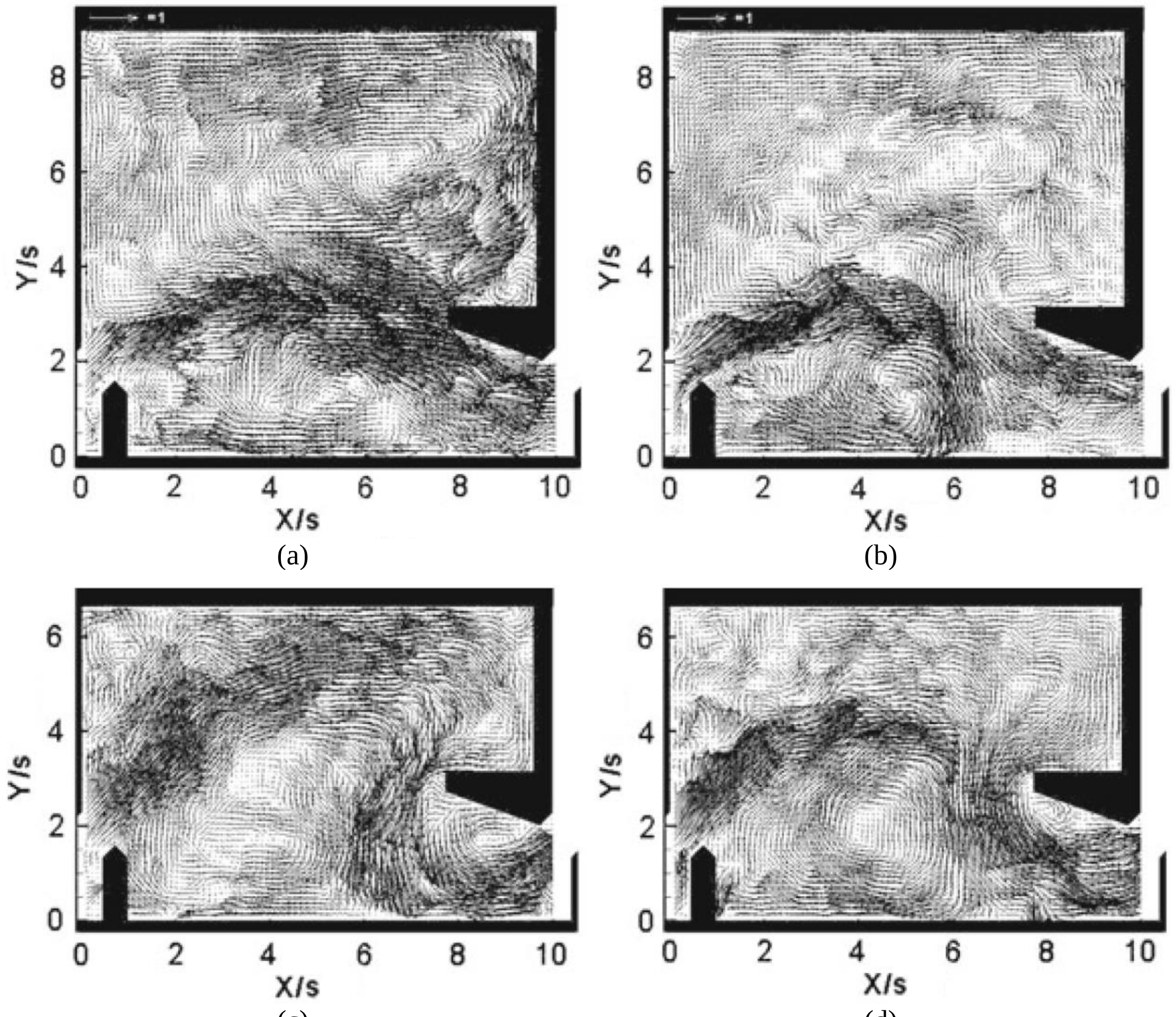

(a) (b)

(c) (d)

Figure 3.7 Unsteady main-stream positions in the instantaneous velocity fields at different time steps measured in the same pool geometries as in Wang et al. (2010) (after Tarrade et al. 2011).

The large-scale flow structure, i.e. the main stream and the recirculation regions, has been observed to show an unsteady, oscillating character in some laboratory scale-model investigations (Wang et al 2010, Tarrade et al 2011, Sokoray-Varga et al. 2012). This can be recognized in the instantaneous velocity fields of PIV measurements shown in Figure 3.7, where both the location of the main stream and the extents of the recirculation regions are unsteady in both of the two different pool geometries representing two different flow patterns. Based on visual observations of the instantaneous velocity fields in different pool geometries, Tarrade et al. (2011) explained the oscillation process as a combined result of velocity bursts arriving from the upstream pool and fluid exchange between the recirculation regions and the main stream.

Tarrade et al. (2011) additionally analyzed the PIV measurements of both pool geometries shown in Figure 3.7 by Proper Orthogonal Decomposition (POD). They recognized that POD mode 1 roughly describes the main-stream oscillation in both geometries. The frequency spectra of the POD-coefficient time series corresponding to POD mode 1 indicated that the characteristic frequencies of the main-stream oscillation were 0.12 and 0.08 Hz. The similar energy contribution levels (λ_i) of POD modes 1 and 2 revealed that POD mode 2 is connected with POD mode 1. Based on the spatial distribution patterns of the vectors in the POD modes they concluded that POD mode 2 represented burst processes of the main stream and POD modes 3 and 4 represented processes arising as a result of the oscillation. More detailed connections between these POD modes or further characteristics of the oscillation were, however, not extracted from the results.

4 Experimental methods

In this chapter, first the laboratory scale model and the experiment execution are described, then possible scale effects arising from using a scale models are addressed by considering the model similitude, and finally technical details of the used Particle Image Velocimetry (PIV) system are presented.

4.1 Experimental setup and execution

The laboratory model of the vertical-slot fish pass was built in the hydraulic laboratory of the BAW. The model consists of 9 identical pools installed in a flume with a slope of 2.8% (Figures 4.1 and4.2).

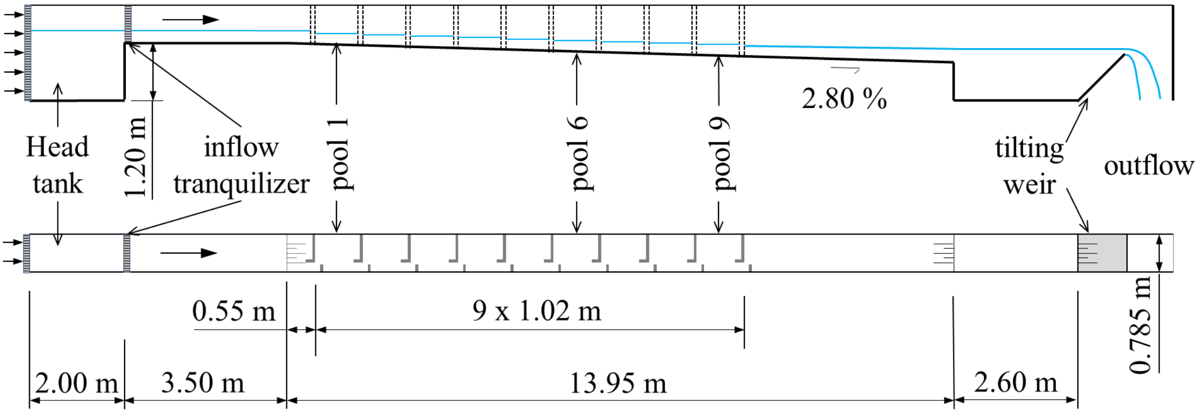

Figure 4.1 Side view and plan view of the laboratory model.

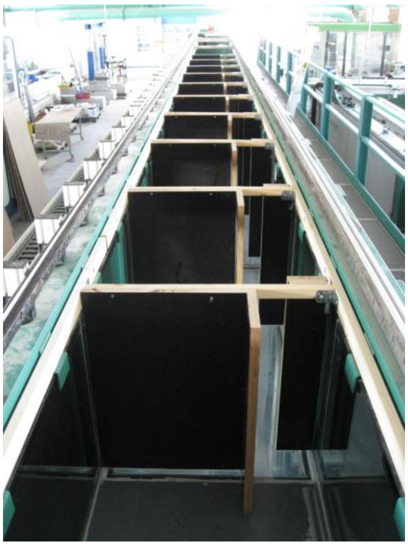

Figure 4.2 Picture of the laboratory model

The pools have a width of 78.5 cm and a length of 99.0 cm; the slot width is 12.2 cm (Figure 4.3 a). The Reynolds number in the scale model is about Re ~ 90 000 considering the slot width as characteristic length and the velocity in the slot as characteristic velocity, which is 0.75 m/s based on Eq. (3.4).

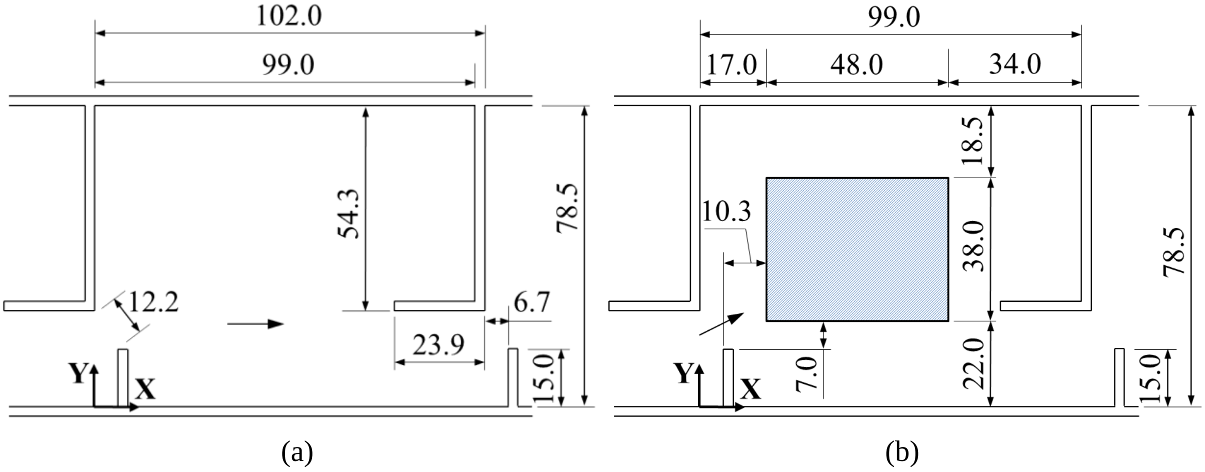

(a) (b)

Figure 4.3 (a) Plan view of a pool and (b) position of the PIV measurement field within the pool. Dimensions are in cm.

The used laboratory model was not the scale replica of a particular fish pass. Since the dimensions of the pool geometry followed the suggestions of the German design guideline of 2010 (DWA 2010), which specifies the dimensions of every pool element based on the slot width, the model can be considered to be a scale model that is not restricted to particular geometric scale (unless the slope is identical). Though, the geometric scale is 1:4.1 with respect to the fish passes being planned along the Neckar River in Germany.

The head tank of the model is supplied with water from the constant-head high-level tank of the laboratory. The discharge in the model can be manually set using an inductive discharge meter (IDM), the water levels can be adjusted by a tilting weir. The water depths were measured by rulers on the downstream side of the baffles and on the upstream side of the cross walls in the same positions in every pool.

The side walls and the bottom of the pools were made of glass, the cross walls and the baffles were made of wood. The edges of the cross walls and the baffles were rounded using a 10 mm radius milling cutter in order to better reflect the edge configuration of the concrete elements in real fish passes and to reduce the amount of air bubbles introduced to the water. It has to be noted that the y-positions of the baffles had to be adjusted due to the rounded edges in order to ensure the specified slot width.

The measurement analyzed in this work was carried out in uniform flow conditions at a discharge of 20 l/s, which was achieved by adjusting the tilting weir so that the water depths were nearly the same in the pools. Though, uniform flow conditions could only be reached in a section of five pools from pool 4 to pool 8, because the water depths deviated in the first three and the last pools, hence they appeared to be influenced by the inlet and outlet flow conditions. In the pools with uniform flow the water depths were 21 cm on the downstream side of the baffles and 24 cm on the upstream side of the cross walls. The velocity distribution showed flow pattern 1 in every pool of the model.

The PIV measurement was performed in pool 6 in a 48 x 38 cm large field 10 cm above the bottom in a plane parallel to bottom as shown in Figure 4.3 (b). The measurement plane was illuminated through the side wall by the laser of the PIV system, and the images were taken by the camera looking through the bottom of the model. The position of the measurement field was selected as displayed in order to include both the main stream and significant parts of the recirculation region in the measurement, thereby containing the main transversal velocity gradients of the flow. In order to reduce the disturbing reflections of the illumination from the surface waves, a 60 x 50 cm large black plate was placed over the measurement field 2 cm below the water surface.

Based on the literature results presented in the previous chapter, the hydraulic characteristics in the pools are independent of the distance from the bottom, so that a measurement performed in a single height was considered to characterize well the processes in the entire depth. Further, since the vertical component of the mean velocity also proved to be negligibly small for such slopes, the plate was expected to have negligible influence on the vertical flow velocity distribution near the position of the measurement field. The plate was selected to be significant smaller than the pool size in order to minimize its influence on the pool-wide water-level oscillations, which are expected to be connected with flow velocity oscillations. However, the final impact of the somewhat dampened water level oscillations on the velocity oscillations was not quantified yet.

The measurement analyzed in the present work was obtained using the 2D-2C PIV system presented in Section 4.3. The five minutes long measurement performed at a sampling frequency of 200 Hz resulted in 60 000 time steps. The recordings were first processed with a Particle Tracking Velocimetry (PTV) algorithm, and then the scattered velocity data was interpolated at each time step to the rectangular grid of 5.0x5.0 mm. Note that, since the measurement plane was parallel to bottom, the direction of the measured u-velocity components was not horizontal but parallel to bottom.

4.2 Model similarity

Quantities from a scale model can be up-scaled to full-scale quantities using specific scale ratios. For example, the lengths (l), the velocities (u) and the times (t) can be up-scaled as:

$$\begin{aligned} l_{(P)} &= c_l \cdot l_{(M)} \\ u_{(P)} &= c_u \cdot u_{(M)} \\ t_{(P)} &= c_t \cdot t_{(M)} \end{aligned} \tag{4.1}$$

where subscripts P and M refer to quantities in the prototype and the model respectively, c_l is the scale ratio of lengths being the geometric scale, c_u is the scale ratio of velocities and c_t is the scale ratio of times.

A laboratory scale model is perfectly similar to its full-scale prototype, if it fulfils the geometric, kinematic and dynamic similarity, i.e. the similarity of shapes (length), motion (time) and forces, respectively. This means that the ratios of the corresponding quantities in the two systems have to be constant. The dynamic similarity implies the geometric and kinematic similarity and additionally requires that the ratios of all forces in the scale model and the prototype are identical. The most relevant forces in fluid dynamics are inertial forces, gravitational forces, viscous forces, pressure forces, surface tension forces and elastic compression forces. The identity of the ratios of all these forces means that the ratio of inertial forces is equal to the ratio of gravitational forces and to the ratio of viscous forces etc. in the scale model and the prototype. However, gravity and viscosity are usually unscaled in scale models, because the gravity acting in the scale model is usually the same as in the prototype, and the viscosity of the model fluid is also unscaled, if the identical fluid is used in the scale model as in the prototype. Consequently, a perfectly similar scale model is hardly possible (with the exception of full-scale scale models). For this reason, only the most dominant forces are scaled and modelled properly by applying special similarity laws, whereas other forces are neglected during the modelling, which may lead to scale effects. For more detailed information it is recommended to refer a textbook or an article on this subject (e.g. Yalin 1971, Heller 2011).

The flow in vertical-slot fish passes was usually modelled in the literature by applying Froude similarity laws. Froude similarity yields the following scale factors for e.g. times and velocities:

$$\begin{aligned} c_u &= \sqrt{c_l} \\ c_t &= \sqrt{c_l} \end{aligned} \tag{4.2}$$

Froude similarity implies that the inertial and the gravitational forces are scaled properly, whereas other forces are not. While pressure forces, surface tension forces and elastic compression forces are expected to play a negligible role in the flow processes in vertical-slot fish passes, viscous forces play a role in the energy cascade of turbulence, hence in the development of the turbulent structures (see Chapter 2). Viscous forces are, however, not scaled properly by the scale model used in the present work, since the water used in the scale model is the same fluid as in the prototype, i.e. viscosity is unscaled in the model.

In the present work the scale effects arising from the incorrect scaling of viscous forces in the scale model were examined as follows. The characteristic eddy sizes in the scale model ($l_{0(M)}$, $l_{EI(M)}$, $l_{DI(M)}$, $\eta_{(M)}$) were first estimated based on the characteristic sizes in the prototype ($l_{0(P)}$, $l_{EI(P)}$, $l_{DI(P)}$, $\eta_{(P)}$) and then compared with each other (for characteristic eddy sizes see Section 2.1).

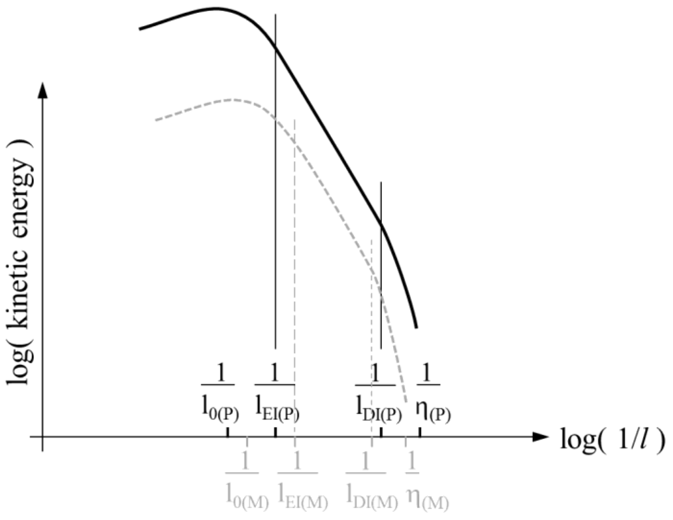

Figure 4.4 Schematic view of the energy spectra in the prototype (solid lines and lengths denoted by P) and in the scale model (dashed lines and lengths denoted by M).

The characteristics of large eddies ($l > l_{EI}$) and of eddies in the inertial subrange ($l > l_{DI}$) are determined by the geometry of the mean flow and the boundary of the flow. Further, processes in these ranges are substantially driven by inertial forces. Therefore, the characteristics of these eddies are reproduced properly by Froude models, so that their sizes are scaled with the geometric scale as:

$$l_{0(M)} = \frac{1}{c_l} \cdot l_{0(P)}$$
$$l_{EI(M)} = \frac{1}{c_l} \cdot l_{EI(P)} \quad (4.3)$$

In the dissipation range, in turn, viscous forces are significant, which are not scaled correctly in Froude models. The dissipation range in the model ($l < l_{DI(M)}$) is determined by the Reynolds number in the scale model, which can written as:

$$Re_{(M)} = \frac{u_{(M)} \cdot l_{(M)}}{\nu} = \frac{\frac{1}{c_u} \cdot u_{(P)} \cdot \frac{1}{c_l} \cdot l_{(P)}}{\nu} = \frac{1}{c_l \cdot \sqrt{c_l}} \cdot \frac{u_{(P)} \cdot l_{(P)}}{\nu} = c_l^{-3/2} \cdot Re_{(P)} \quad (4.4)$$

The Kolmogorov scale in the scale model can be approximated using Eqs. (2.3) and (4.4) as:

$$\eta_{(M)} = l_{0(M)} \cdot Re_{(M)}^{-3/4} = \frac{1}{c_l} \cdot l_{0(P)} \cdot \left(c_l^{-3/2} \cdot Re_{(P)}\right)^{-3/4} = c_l^{1/8} \cdot \eta_{(P)} \quad (4.5)$$

It can be recognized that while large eddies are smaller in the scale model than in the prototype, dissipative eddies ($l_{DI} > l > \eta$) are relatively larger in the scale model than in the prototype (Figure 4.4).

Turbulent structures are expected to be reproduced properly by a scale model unless they are in the dissipation range of the scale model, i.e. only eddies of sizes $l >> l_{DI(M)}$ are expected to be reproduced properly. This scale effect arises from the improper scaling of the viscous forces in Froude models and is relevant, if the investigated turbulent scales are in the dissipation range in the scale model.

The flow in a scale model is seriously affected by this scale effect, if the dissipation range and the energy containing range in a scale model get near to each other, i.e. there is no significant inertial subrange. In this case, the flow in the scale model is not fully turbulent, so that even the mean flow characteristics are expected to be improperly reproduced. This is usually avoided by choosing a geometric scale yielding a high Reynolds number, so that the flow in the scale model is fully turbulent.

The estimation of the different eddy sizes in the scale model used in this work give the following results. Since the eddies of the energy containing range are determined by the width of the main stream at the slot (s = 12.2 cm), their sizes are in the same order of magnitude yielding $l_{0(M)}$~10 cm. The inertial subrange starts at an order of magnitude smaller eddy sizes $l_{EI(M)}$~1.67 cm (see Section 2.1). The Reynolds number in the scale model used in present work is about $Re_{(M)}$~ 90 000 (see Section 4.1). The eddy sizes of the dissipation range in the scale model can be estimated based on Eqs. (2.3) and using $l_{0(M)}$ and $Re_{(M)}$; the Kolmogorov scale gives $\eta_{(M)}$~0.001 cm and the upper limit of the dissipation range is about $l_{DI(M)}$~0.06 cm. Although this estimation has to be regarded as an order of magnitude approximation, it clearly shows that a significant inertial subrange is expected in the scale model, so that a part of the inertial subrange of the prototype is expected to be reproduced properly.

Since the present study deals with the energy containing range, which is scaled properly in the scale model used in the present work, the results are expected to be unaffected by the scale effect described before. Although the results presented in this work are not scaled to prototype, the Froudian scaling laws are applicable to convert the results of the scale model to prototype (for the energy containing range).

4.3 Particle Image Velocimetry (PIV)

The velocity data of the present work was measured by an in-house constructed Particle Image Velocimetry (PIV) system.

4.3.1 Principles of PIV

Particle Image Velocimetry (PIV) is an optical measurement technique providing non-intrusive flow velocity measurements at high sampling rates over the whole measurement field simultaneously. In this section a brief description is given on this technique; for more detailed information it is worth to consult e.g. Raffel et al. 1998.

The methodological principle of PIV is that tracer particles are added to the flow that are illuminated by an intensive light source and recorded by cameras. The local flow velocities are measured by determining the displacements of the tracer particles in the images between two subsequent recordings, which define the velocity by considering the time delay between recording the images. The particle displacement can be determined based on the characteristic group of neighboring particles, called here neighborhood, which has a specific local distribution pattern.

PIV systems usually consist of following essential hardware components: camera(s) to take images, data recording units to store the taken images, tracer particles that follow the flow as correctly as possible, a light source (usually a laser) with adequate optics to illuminate the tracer particles, and a trigger to synchronize all the components (Figure 4.5).

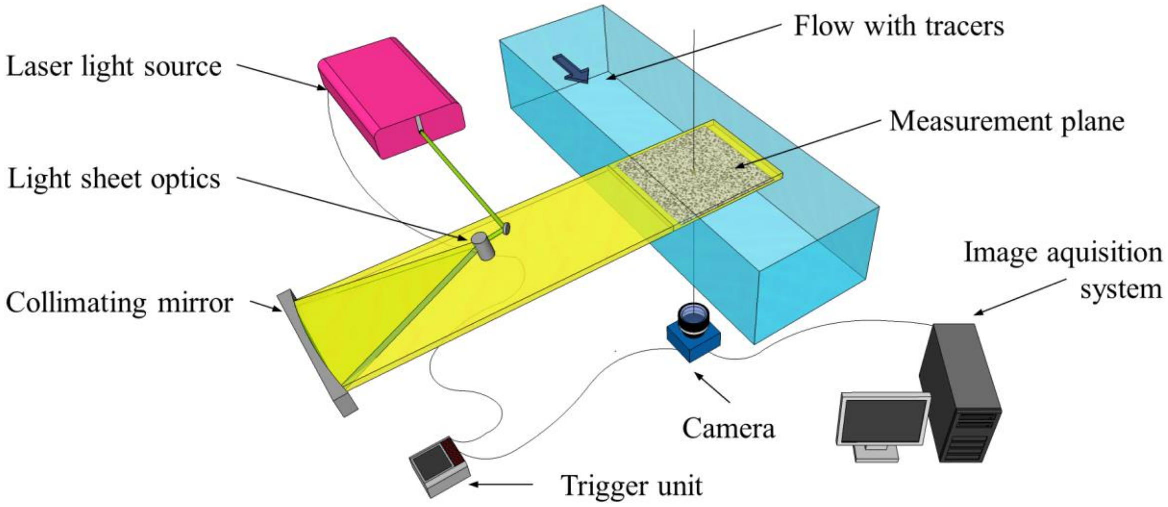

Figure 4.5 Schematic view of the PIV system

There exist different PIV-system configurations. The PIV system of the present work used light-sheet optics for the illumination and a single camera to record the images. Since the light-sheet optics illuminates a quasi 2D plane of the flow, and the single camera provides two velocity vector components, which are the projections of the three-dimensional vectors into the image plane, such a system is conventionally denoted as 2D-2C.

The velocity vectors are obtained by evaluating the recorded PIV images by software. There are two basic types of velocity evaluation algorithms. Particle Image Velocimetry (PIV) algorithms subdivide the images into rectangular segments, called interrogation areas, and determine the displacements of the individual interrogation areas, so that one vector is produced per interrogation area. Particle Tracking Velocimetry (PTV) algorithms, in turn, determine the displacement of each individual particle based on the individual neighborhoods. Both types of algorithms have advantages and disadvantages. Essential differences are briefly the following. Due to the spatial filtering effect of the interrogation areas, PIV algorithms produce lower noise results but are more sensitive to local velocity gradients. PTV algorithms, in turn, provide higher spatial resolution and are less sensitive to velocity gradients, but the obtained scattered data has a higher noise and has to be interpolated if the analysis is grid point based. It has to be noted that there exists a large number of methods for both types of algorithms, which themselves have strengths and weaknesses.

Further, it can be distinguished between single-pulsed and double-pulsed systems. Without going in details on the physical backgrounds of pulsed lasers, double-pulsed lasers produce pulse pairs with short time separation, which result in image pairs recorded with short time separation. Since the velocity evaluation algorithms have limitation on the largest and smallest particle displacements between subsequent images and on the gradients in the displacement of neighborhoods, the time delay between recording the images has to be adjusted to these characteristics. As the time separation between the pulses of the double pulse is relative flexible selectable, double pulsed lasers are more flexible adjustable than single pulsed lasers. In turn, while single pulsed systems produce a velocity field based on every image, only every second image provides velocity data in a double pulsed system, since a velocity field is only obtained by an image pair created by a pulse pair.

4.3.2 PIV hardware

The light source of the system was a 20 W Nd:YAG single pulsed laser emitting visible green light at 532 nm wavelength (Yasmin/Quantel). The maximal pulse rate was 200 Hz at pulse energy of 100 mJ; the pulse duration was 8 ns and the beam diameter was 8 mm. The green color was selected because green light is less absorbed in water than red (e.g. Smith et al. 1981).

The light sheet was produced from the beam by a combination of a cylindrical lens and a collimating mirror, which generated a constant width plane light sheet of approximately 50 cm width. The images were recorded via a surface mirror through the bottom of the model. (Figure 4.5)

An 8-bit monochrome camera with a CMOS sensor of 1280x1024 pixels resolution was used to record the images (Mikrotron MC1362). The camera was used with a Zeiss Planar T 1.4/85 ZF objective providing low optical distortion. The field of view of the camera was nearly 51x41 cm, which resulted in a pixel resolution of 0.4 mm/pixel.

The 250 Megabytes data per second produced by the camera (200 fps) was transferred to the image acquisition system over Camera Link interface. The image acquisition system was a RAID system capable to store data in real time at such transfer rates. The measurement duration of 300 s resulted in nearly 75 GB of raw image data.

To visualize the flow, polyamide particles of $\rho_p = 1.06$ g/cm^3 density and particle diameters between 30-250 μm (VESTOSINT 1101) were used.

4.3.3 Velocity evaluation using particle tracking

The velocity information was extracted from the recorded image sequence using the Particle Tracking Velocimetry (PTV) algorithm published in Sokoray-Varga et al. (2008). The PTV evaluation consists of two essential steps: particle detection and particle displacement determination.

The particle detection identifies the tracer particles in the recorded images and determines the coordinates of their centroids with sub-pixel accuracy. The tracer particles are first detected based on their typical brightness pattern in the images. Then, in order to achieve a higher accuracy of the particle positions than the pixel resolution of the images, the sub-pixel accuracy locations of the particle centroids are estimated by an interpolation method. Such interpolation methods tend, however, to shift the particle centroid towards the center of the pixels, which is referred to as pixel locking. Since this introduces an error to the resulting velocity vectors (see Section 4.3.5), this tendency can be displayed using the probability density function of the fractional part of the obtained particle positions (Figure 4.6).

It has to be noted that sub-pixel interpolation methods require that the particles are visible on at least 3x3 pixels. Since the particle diameter of the present work was significantly smaller than the image resolution of 0.4 mm/pixels (see Section 4.3.2), the requirement was fulfilled by defocusing the objective.

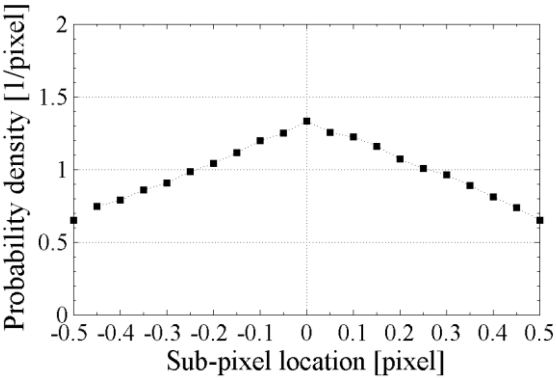

Figure 4.6 Probability density function of the fractional part of the particle positions.

The particle displacement determination identifies each particle in the subsequent frame based on the characteristic distribution pattern of their neighborhoods, so that the displacement vector of each individual particle can be determined. Sources of errors in the identification are too strong deformations of the neighborhood (velocity gradients) or the appearance or disappearance of particles in the second image (e.g. out-of-plane velocity). Both sources lead to false particle detections, which have to be filtered out in the results. The filtering of the erroneous velocity vectors was performed using the median filter by Westerweel et al. (2005).

An indicator for the effectiveness of the particle displacement determination is the percentage of the successfully identified particles with respect to the number of particles in the first image, which was about 66% in the present velocity evaluation. The number of successfully identified particles was about 25 000 per image.

The velocity vectors can be determined after converting the origin and the end positions of the particles from image coordinates to real coordinates based on the camera calibration field.

4.3.4 Interpolation to a rectangular grid

The scattered velocity vectors obtained by the PTV algorithm were interpolated to a rectangular grid using the Delaunay triangulation based natural neighbor interpolation method, which can be briefly explained as follows (e.g. Barnett 1981).

The Voronoi tessellation assigns a cell to each of the scattered data points based on the Delaunay triangulation (Figure 4.7 a). As a result, the Voronoi cell assigned to P_k defines the positions in the plane that are nearer to P_k than to any other scattered point. The natural neighbors of P_k are the scattered points corresponding to the cells neighboring with the cell of P_k.

According to the natural neighbor interpolation, the points to be interpolated is temporarily inserted to the tessellation, and the Voronoi cell of the inserted point is created by reassigning portions from the cells of the natural neighbors according to the Voronoi tessellation (Figure 4.7 b). The value of the new point is interpolated as:

$$u(x_n, y_n) = \sum_{i=1}^{m} w_i \cdot u(x_i, y_i) \tag{4.6}$$

where $u(x_i,y_i)$ is the velocity in the i-th natural neighbor of the grid point, w_i is the weight corresponding to the i-the natural neighbor and m is the number of natural neighbors. The weights are calculated based on the areas originating from the individual natural neighbors as exemplary shown in Figure 4.7 (b). As a result, the interpolating surface is C^1-continuous, which means that its first derivative is continuous.

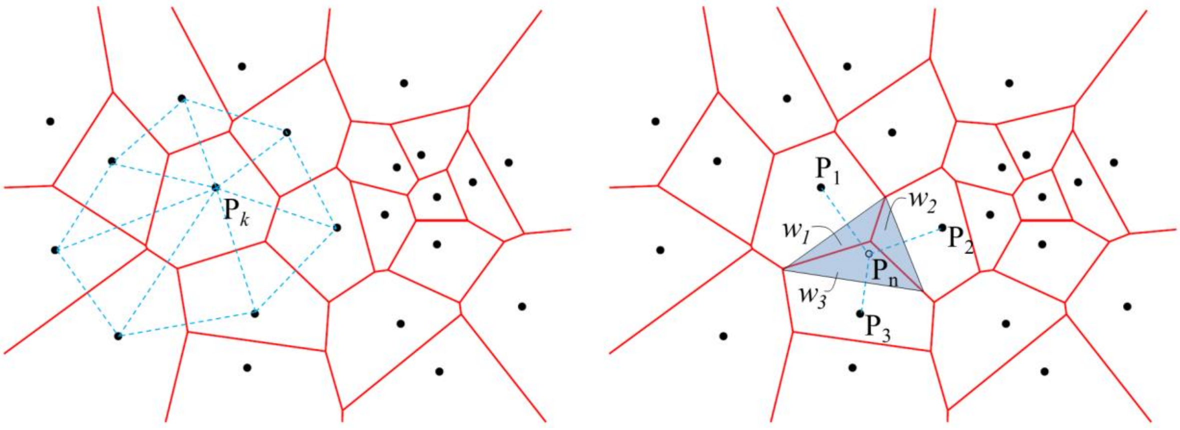

(a) (b)

Figure 4.7 Natural neighbor interpolation of scattered data: (a) natural neighbors of point P_k and (b) the weights w_i of the interpolation at point P_n. The black points are scattered data points, the dashed lines are the Delaunay triangles and the solid lines are the Voronoi cells. (after Ledoux 2006)

Interpolation is only possible within the area covered by scattered data. In order to avoid extrapolation, the area of the grid was selected to be preferably within the convex hull of the locations of the scattered vectors. Though, as a result of the moving characteristic of particles with inhomogeneous distribution and of vectors missing due to error filtering, some grid points happen to fall outside the convex hull of the scattered data in some snapshots. Data in such grid points has been extrapolated by the nearest neighbor method.

The interpolated values always differ to some extent from the true velocity values. In addition, since the interpolation is performed on the basis of data containing measurement noise, the interpolation methods might increase or decrease the noise in the result.

The interpolation method described above has been selected after comparing the noise levels obtained from different interpolation methods. The noise levels were ascertained based on the velocity spectra computed from the interpolated data (see Section 4.3.5). As it will be explained later, the noise level in the time series can be seen on the variance contributions at high frequencies, where a nearly constant value in the velocity spectra is reached. For ascertaining the noise levels, the velocity spectra were computed by Welch's method according to Eq. (2.19) using $K = 16$ segments, because smoothed values were required at high frequencies.

Figure 4.8 exemplarily shows velocity spectra of time series obtained using two different interpolation methods. The results in Figure 4.8 (a) were produced using the interpolation method presented in this section; whereas the results in Figure 4.8 (b) were produced using cubic interpolation, which is also based on the Delaunay triangulation and is C^2 continuous. As it can be observed, the noise level in the dataset interpolated by the natural neighbor interpolation is lower. This can be considered as a consequence of the weighted spatial averages computed by the method, which decrease the rather random errors arising from the pixel locking of the particle detection.

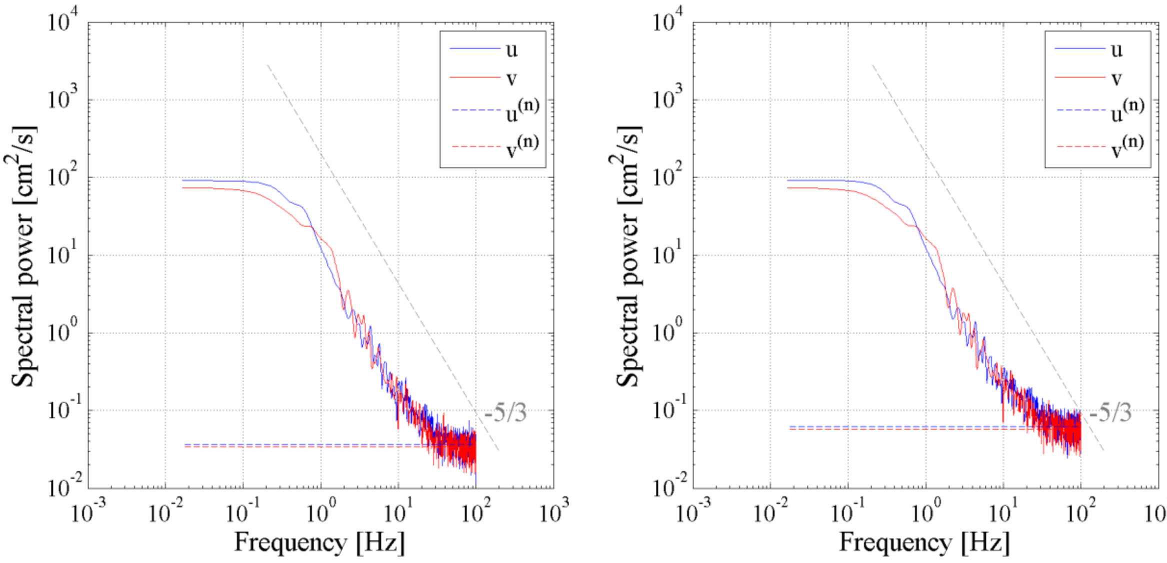

(a) (b)

Figure 4.8 Velocity spectra in the same grid point resulting from datasets produced using different interpolation methods: (a) natural neighbor interpolation and (b) cubic interpolation. (u and v denote the PSD of the interpolated time series, $u^{(n)}$ and $v^{(n)}$ denote the noise)

4.3.5 Measurement errors

The main errors in the velocities measured by the presented PIV system arise due to out-of-plane motion, particle density, pixel locking and interpolation to rectangular grid.

The out-of-plane motion produces an error, because, due to the use of a single camera, the measured vector components are the projections of the three-dimensional vectors into the image plane. The error introduced by this depends on the magnitude of the out-of-plane velocity component, which, however, has not been measured explicitly. Since the largest and most energetic flow structures within the vertical-slot fish pass can be considered to be approximately two dimensional in the area of the measurement field (see Sections 3.2 and 3.3), this error was neglected in this work.

Due to the principles of PIV, it has to be assured that tracer particles follow the local flow velocities. The primary source of error is the density difference between fluid and tracer particle. The behavior of particles exposed to accelerations in a fluid flow can be estimated by the Stokes number (e.g. Ruck 1990):

$$Stk = \frac{\tau_p \cdot u_f}{l_f} \tag{4.7}$$

where u_f is the characteristic velocity of the fluid, l_f is the characteristic size in the fluid and τ_p is the relaxation time of the particle, which can be obtained as:

$$\tau_p = \frac{d_p^2 \cdot \rho_p}{18 \cdot \nu \cdot \rho_f} \tag{4.8}$$

where d_p is the particle diameter, ρ_p is the particle density and ρ_f is the fluid density. The l_f is intended to represent the distance after which the fluid can be expected to decelerate from u_f to 0. Tracer particles follow the flow faithfully if $Stk << 1$. The flow characteristics $u_f = 0.75$ m/s, $l_f = 0.1$ m and the largest particle sizes of $d_p = 250$ μm yield $Stk \sim 0.02$, so that errors arising from tracing accuracy is negligible.

The errors arising from the pixel locking of the particle detection and from the interpolation of the scattered data to the rectangular grid are handled together in the present examination as follows.

Pixel locking arises during particle detection and occurs when the estimated position of the particle is shifted towards the next integer value (see Section 4.3.3). If the velocity vectors are determined based on such inaccurate particle positions, the error propagates to the measured velocity vectors and results in a noise in the velocity. As described in Section 4.3.4, the interpolation also affects the noise level. Since only the interpolated data was used in the later analysis, only the resulting noise and the collective error of these sources are considered in this work based on the interpolated data.

Accordingly, the measured fluctuation time series are considered to be composed as:

$$u^i = u^{i,(t)} + u^{i,(n)} \tag{4.9}$$

where $u^{i,(t)}$ are the instantaneous values of the true velocity and $u^{i,(n)}$ are the instantaneous contributions of the noise.

For the estimation of the arising error, it is assumed that the collective noise resulting from the pixel locking and the interpolation is Gaussian white noise in the velocity fluctuations. Gaussian white noise has a constant variance contribution over frequency, so that the PSD of the noise in the velocity fluctuation is constant:

$$S_{uu}^{(n)}(f\ ) = \text{const} \qquad (4.10)$$

The PSD of the measured velocity that contains noise is (e.g. Nikora et al. 1998):

$$S_{uu}^{(m)}(f\ ) = S_{uu}^{(t)}(f\ ) + S_{uu}^{(n)}(f) \qquad (4.11)$$

where $S_{uu}^{(m)}$ is the PSD of the measured velocity, $S_{uu}^{(t)}$ is the PSD of the true velocity.

Since the variance contributions of the turbulent velocity fluctuation decrease with increasing frequency (see Section 2.1) but the variance contributions of the noise in the velocity fluctuation is assumed to be constant, the variance contributions of the noise become dominant above a certain frequency f_c (e.g. Figure 4.8), so that $S_{uu}^{(n)}$ can be determined based on the constant values at high frequencies of the velocity spectra (e.g. Nikora et al. 1998).

The PSD contribution level of the noise in the velocity fluctuation was calculated in this work as follows. First, the critical frequency f_c, above which the PSD of the measured velocity time series obtained a constant value, was ascertained. This could be determined in the velocity spectra of every grid point as $f_c \sim 60$ Hz. Then, the PSD contribution level of the noise was calculated in each individual grid point for each velocity component as the mean PSD value at frequencies above f_c:

$$S_{uu}^{(n)}(x,y,z) = \frac{1}{M}\sum_{k=1}^{M} S_{uu}^{(a,w)}(x,y,z,f_k), \qquad f_k > f_c \tag{4.12}$$

where f_c is the critical frequency, $S_{uu}^{(a,w)}$ is the PSD of the measured time series and M is the number of the available frequencies above f_c. The PSD of the measured time series was computed by Welch's method according to Eq. (2.19) using $K = 16$ segments, in order to get a variance reduced spectra at high frequencies (see Section 2.3.2). Figure 4.9 exemplarily shows the results of such a calculation.

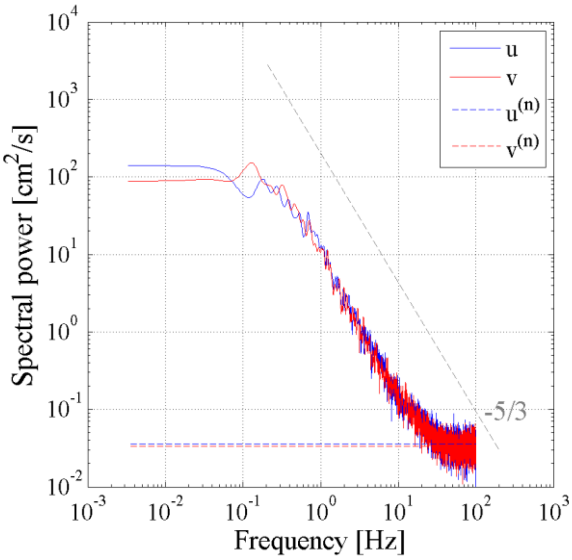

Figure 4.9 PSD contribution levels of the noise in the measured velocity time series; u and v denote the PSD of the measured time series, $u^{(n)}$ and $v^{(n)}$ denote the PSD of the noise.

The variance arising from the noise in the velocity fluctuation was obtained as the integral of the PSD contributions over the frequency:

$$VAR_u^{(n)}(x,y,z) = \sum_{k=1}^{N/2} S_{uu}^{(n)}(x,y,z,f_k) \tag{4.13}$$

The variances arising from the noise in the velocity fluctuation produced by the pixel locking and the interpolation was estimated in every grid point of the PIV measurement for both velocity components as described above (Figure 4.10).

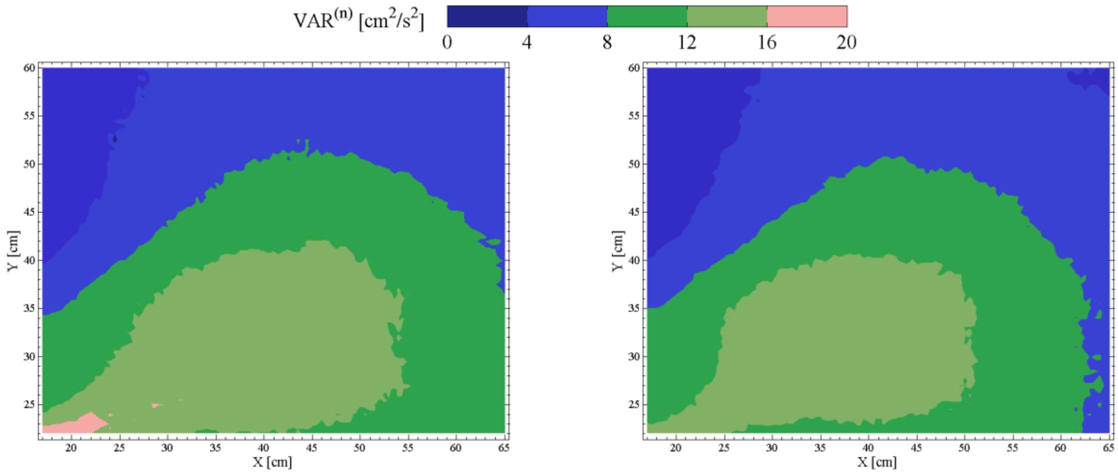

(a) (b)

Figure 4.10 The variance introduced by the pixel locking and the interpolation to the measured velocity time series of (a) u-velocity component and (b) v-velocity component

The error introduced to the velocity variance by this noise can be expressed in percentage of the total variance of the measured time series in every grid point (Figure 4.11):

$$\epsilon_{VAR}^{(n)}\ (x,y,z)=\frac{VAR_u^{(n)}(x,y,z)}{VAR_u\ (x,y,z)} \tag{4.14}$$

where $VAR_u(x,y,z)$ is the variance of the measured time series according to Eq. (2.10).

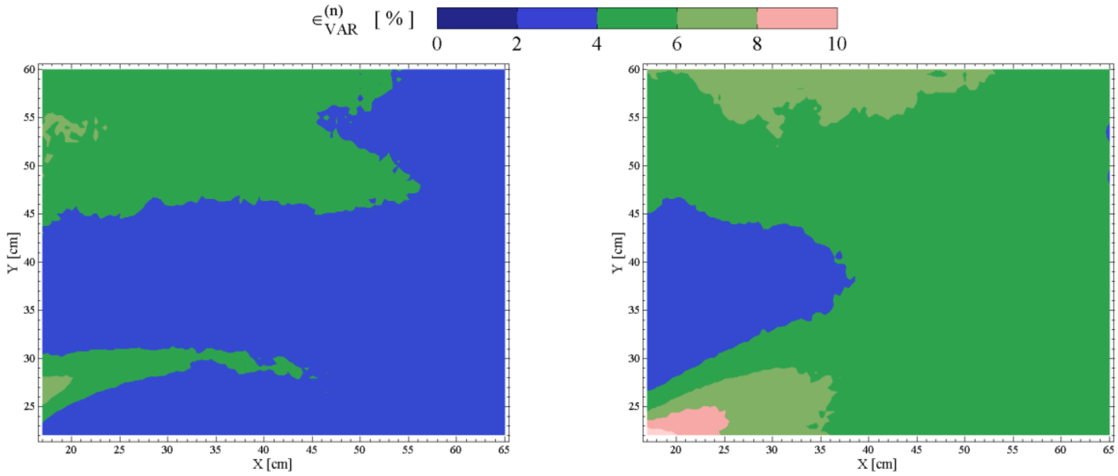

(a) (b)

Figure 4.11 The error introduced by the pixel locking and the interpolation to the measured velocity variance of (a) u-velocity component and (b) v-velocity component

Note that, although the variances and velocity spectra of the measurement could be corrected by reducing them by the contribution of the noise based on Eq. (4.11), the velocity time series cannot be corrected adequately. For this reason, in order to keep the integrity of the different calculated features, the velocity spectra and variances are also not corrected in the present work.

5 Statistical analysis and Proper Orthogonal Decomposition of the PIV measurement

In this chapter the measured velocity dataset is analyzed using the methods described in Chapter 2. The PIV measurement was carried out as described in Section 4.1. The measurement of 5 minutes duration performed at 200 Hz measurement frequency resulted in a velocity dataset containing 60 000 instantaneous velocity fields, each consisting of 7 469 two-dimensional velocity vectors located on a rectangular grid with 5.0x5.0 mm spacing.

5.1 Time-series analysis in the grid points

For the analysis of the velocity time series in the individual grid points the instantaneous velocities were decomposed to mean velocities and velocity fluctuations following Eqs. (2.6) and (2.7).

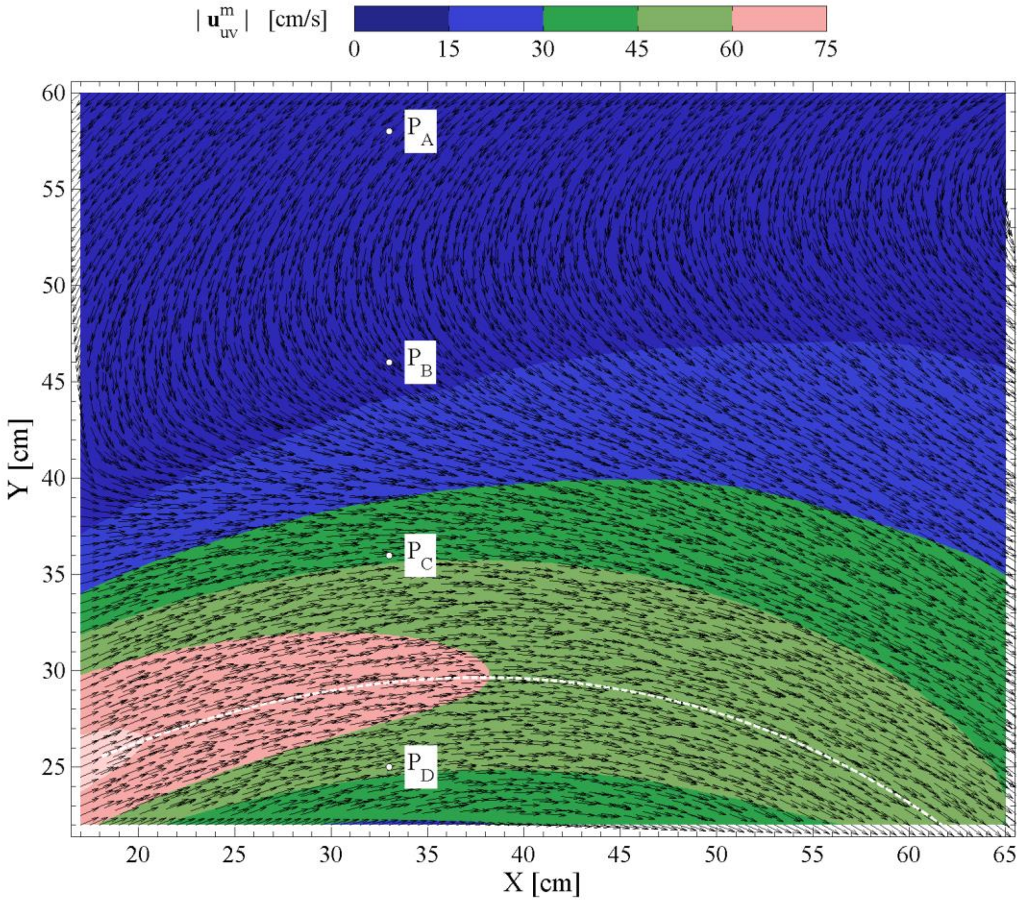

Figure 5.1 The mean velocity field with the centerline of the mean main stream. Detailed results of the time series in the grid points P_A-P_D are presented.

Figure 5.1 shows the mean velocity vectors in the individual grid points. The main stream interconnecting the slots consists of higher velocities, whereas the recirculation region is characterized by lower velocities, as described in the literature. The velocity distribution confirms that the flow in the pool is of flow pattern 1. The velocity magnitudes are roughly about 3 times higher within and around the main stream than in the recirculation region, and the ratio of the highest and lowest mean velocities is 15, which indicate an inhomogeneous mean flow field. A streamline along the highest velocity magnitudes of the cross sections is displayed by a dashed line in Figures 5.1 and 5.2 to illustrate the centerline of the main stream in the mean velocity field, called here the *mean main-stream centerline*.

The turbulent kinetic energy field in Figure 5.2 shows that the highest turbulence levels arise on the sides of the mean main stream, which are expected to be turbulence generating zones.

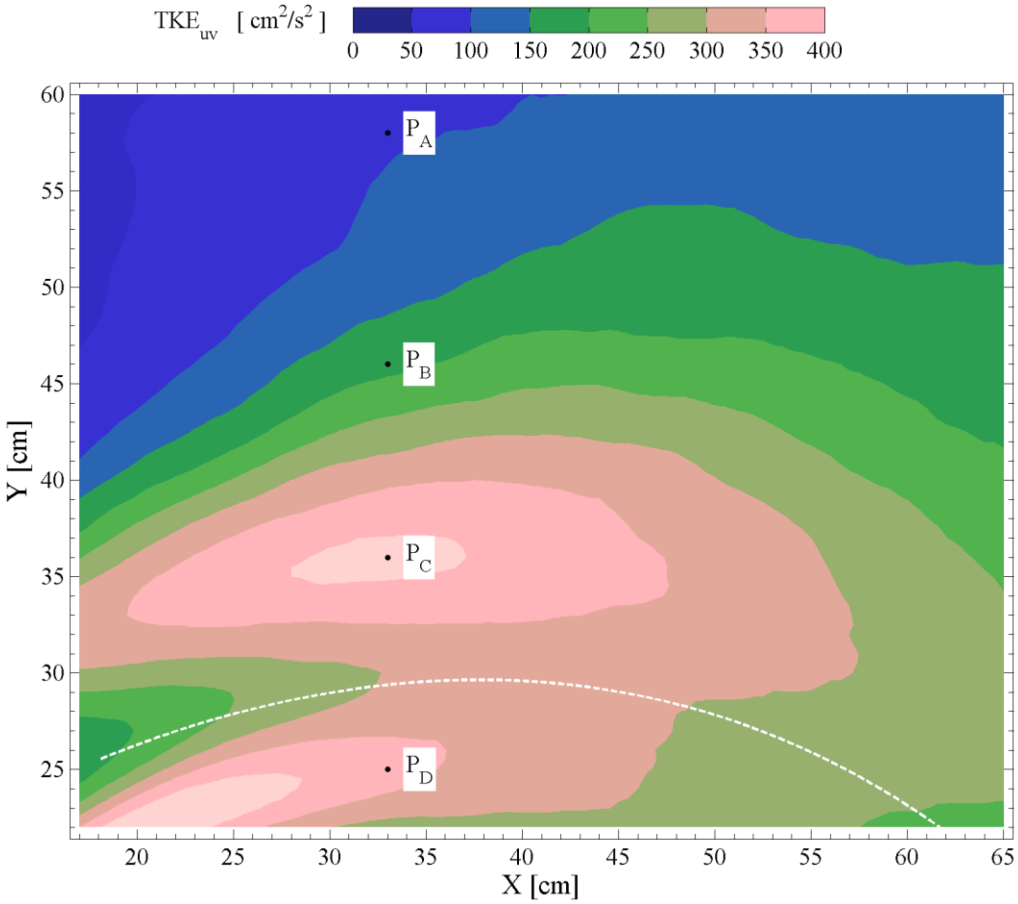

Figure 5.2 The turbulent kinetic energy field with the centerline of the mean main stream. Detailed results of the time series in the grid points P_A-P_D are presented.

The time-series analysis was performed in every measured grid point as described in Section 2.3. Though, as detailed results of each of the 7 469 individual grid points cannot be displayed in a printed work, those in the grid points P_A-P_D marked in Figures 5.1 and 5.2 were selected to be shown explicitly, as they represent well the tendencies within the measurement field. The selected points are in the same cross section; P_A, P_B and P_C are on the left-hand side of the mean main-stream centerline, whereas P_D is on the right-hand side in main flow direction; P_C and P_D represent the zones of highest TKE levels on each side of the mean main stream, while P_B represents the transition zone and P_A the areas characterized by low TKE levels. Time series of these grid points are displayed in Figure 5.3.

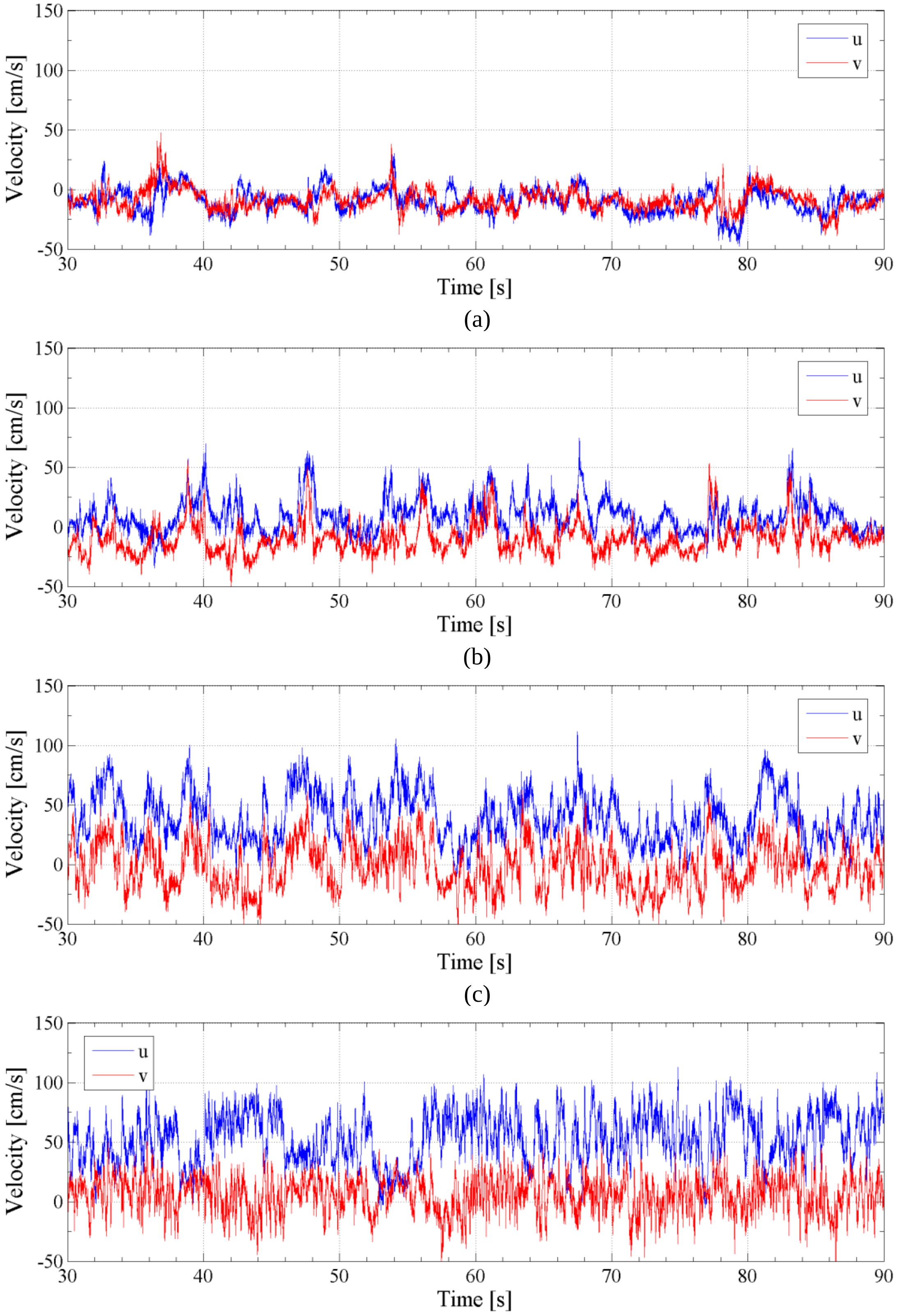

(a)

(b)

(c)

(d)

Figure 5.3 Exemplary sequences of the measured velocity time series in (a) P_A, (b) P_B, (c) P_C, (d) P_D.

The power spectra of the velocity time series are shown in Figure 5.4. Welch's method according to Eq. (2.19) using $K = 4$ segments was selected for the computation as a compromise between obtaining recognizable peaks at low frequencies and gaining a smoothed power distribution. Although the power spectra are very similar in the individual grid points, a continuous transition of the characteristics can be observed within the measurement field. The tendency of this transition is well represented by the results of points P_A, P_B and P_C (Figures 5.4 a-c) on the left-hand side of the mean main-stream centerline, while the results of P_D represents well the flow characteristics on the right-hand side.

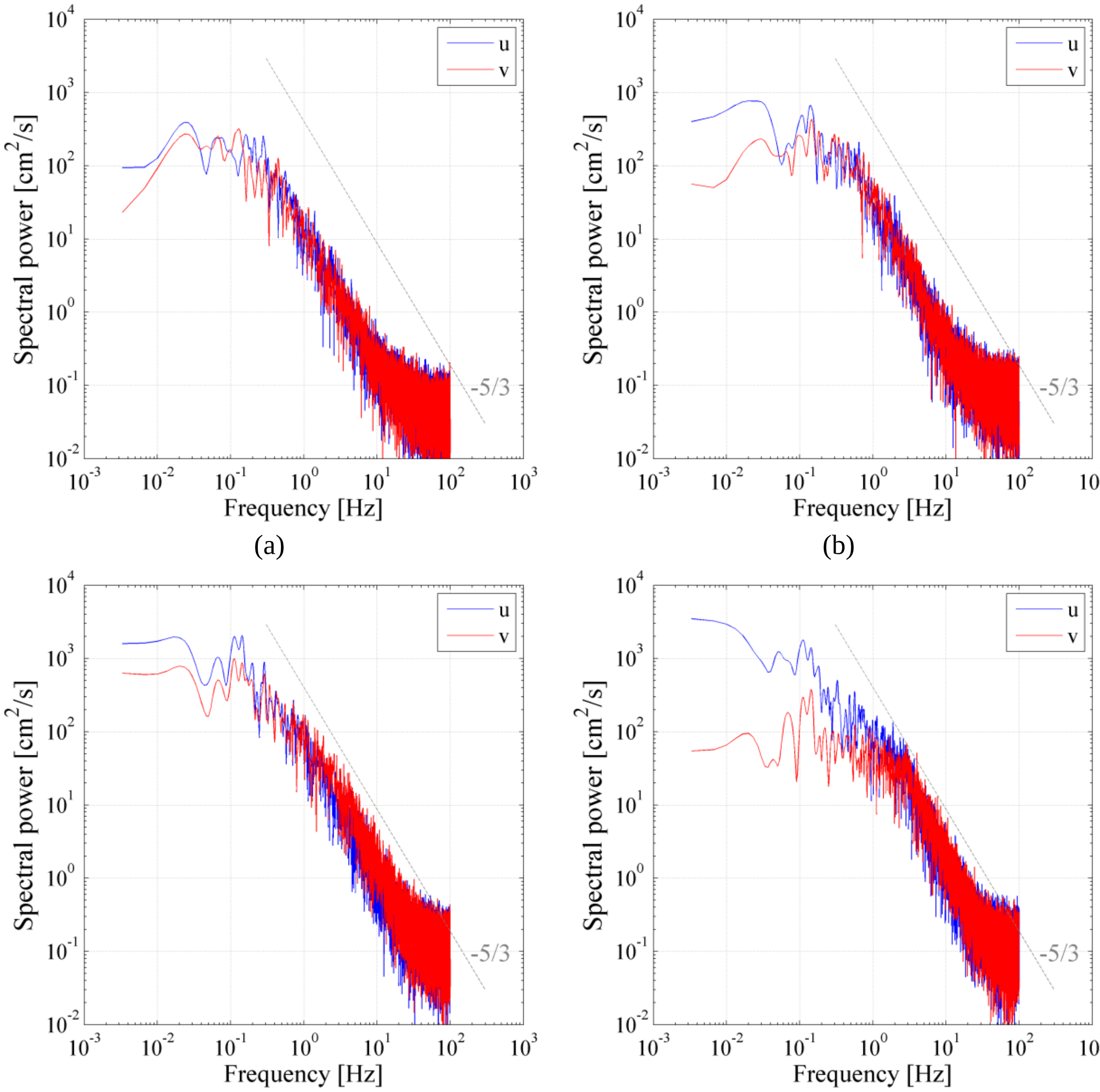

(a) (b)

(c) (d)

Figure 5.4 Velocity spectra of the measured time series (a) in P_A, (b) in P_B, (c) in P_C, (d) in P_D.

The energy contribution levels generally decrease from the high levels in P_C through P_B to the low levels in P_A (Figure 5.4 a-c), which agrees with the change of the TKE levels (Figure 5.2). The power spectra show a clear -5/3 slope in every measured grid point, which approves that the energy containing range was captured by the measurement. The frequency, at which the velocity spectra obtain the -5/3 slope, is about 3 Hz in positions near to the mean main stream and decreases with increasing distance from the main stream to about 1 Hz. Note that this will be used in Chapter 6. Remarkable peaks can be observed in the velocity spectra between 0.1 and 0.2 Hz, which is more significant near to the main stream than in grid points further away. It can, however, not be determined based on such statistical analyses, what flow structures produce these peaks, which will be revisited in Chapter 6.

Although the u- and the v-components show very similar spectra in most parts of the field, there are some areas, like in P_D on the right-hand side of the mean main-stream centerline, where their energy contributions are significantly different in the low frequency range (e.g. Figure 5.4 d).

For the analysis of the measurement duration both the convergence of statistical quantities was examined and the error arising from the finite length measurement was estimated. The mean and the variance were examined in particular, because they are expected to be the most relevant quantities for the Proper Orthogonal Decomposition (POD) analysis in Section 5.3 and Chapter 6.

The convergence of the statistical quantities over the measurement time were visually confirmed in every grid point based on the cumulative mean and cumulative variance functions of the time series as described in Section 2.3.1. The 95%-duration of the variance, which reveals over which duration the last 5% change of the final variance value is obtained (see Section 2.3.1), was determined in every grid point and is displayed as field for the u-velocity component in Figure 5.5. The 95%-duration reveals that, although the variances converge, the last 5% change occurs in the last 30 seconds of the measurement duration in large parts of the measurement field, which suggests that the measurement duration was not long enough in these areas.

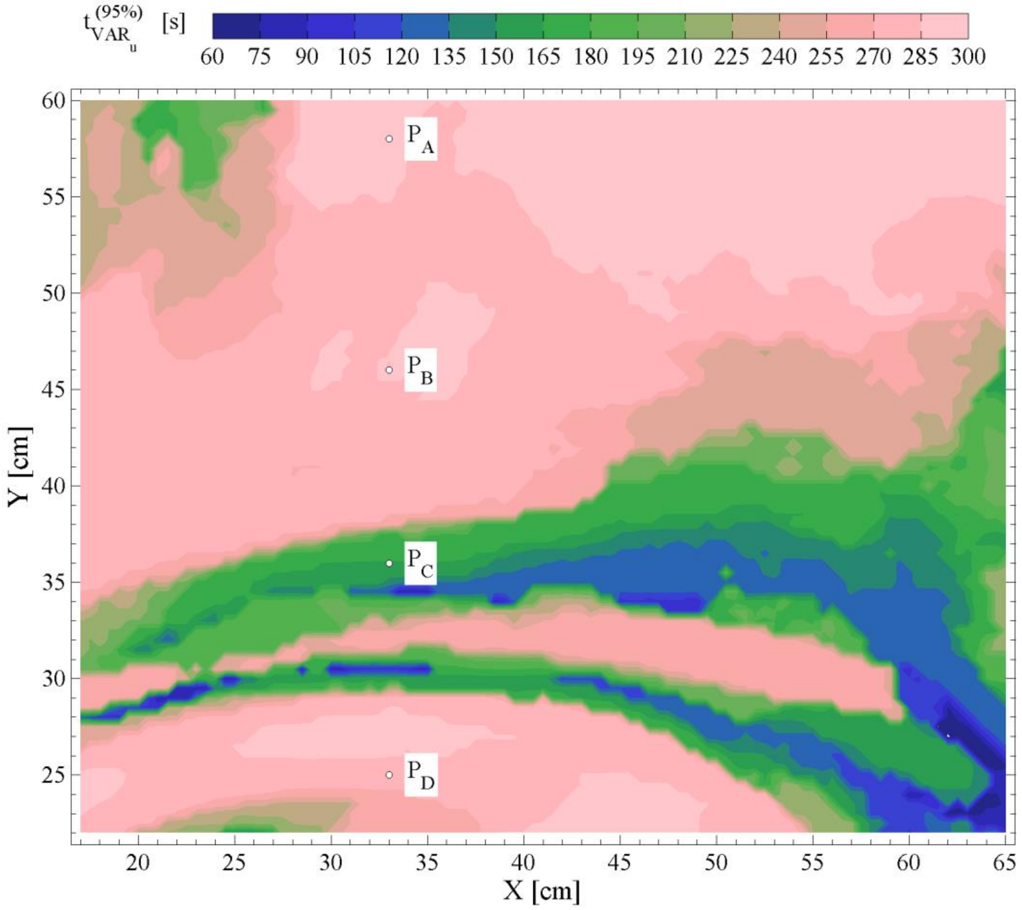

Figure 5.5 Durations at which 95% of the final variance value is reached

In order to quantify the error arising from the finite length measurement, the normalized mean errors of the measured mean and variance values were estimated in every grid point according to Eqs. (2.25) and (2.26), and are displayed in Figures 5.6 (a) and (b), respectively. Note that the results are shown here for the u-velocity component, as it yielded to higher errors than the v-velocity component.

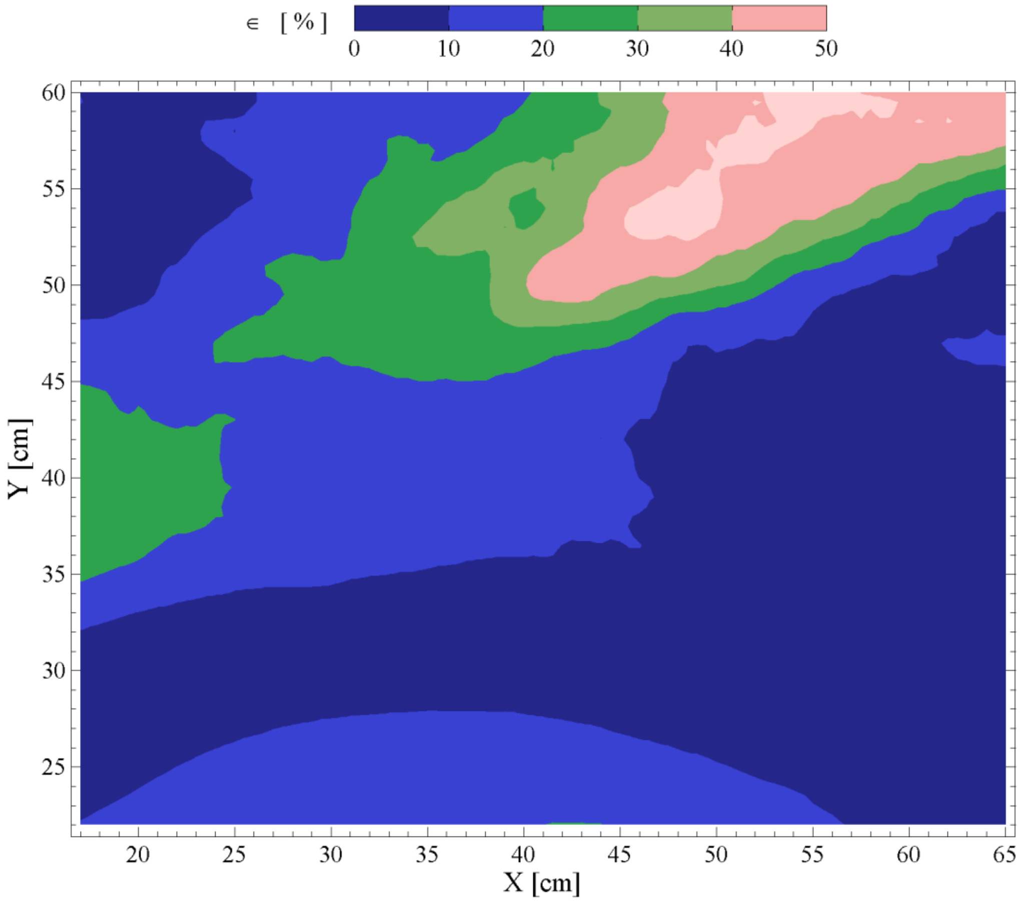

(a)

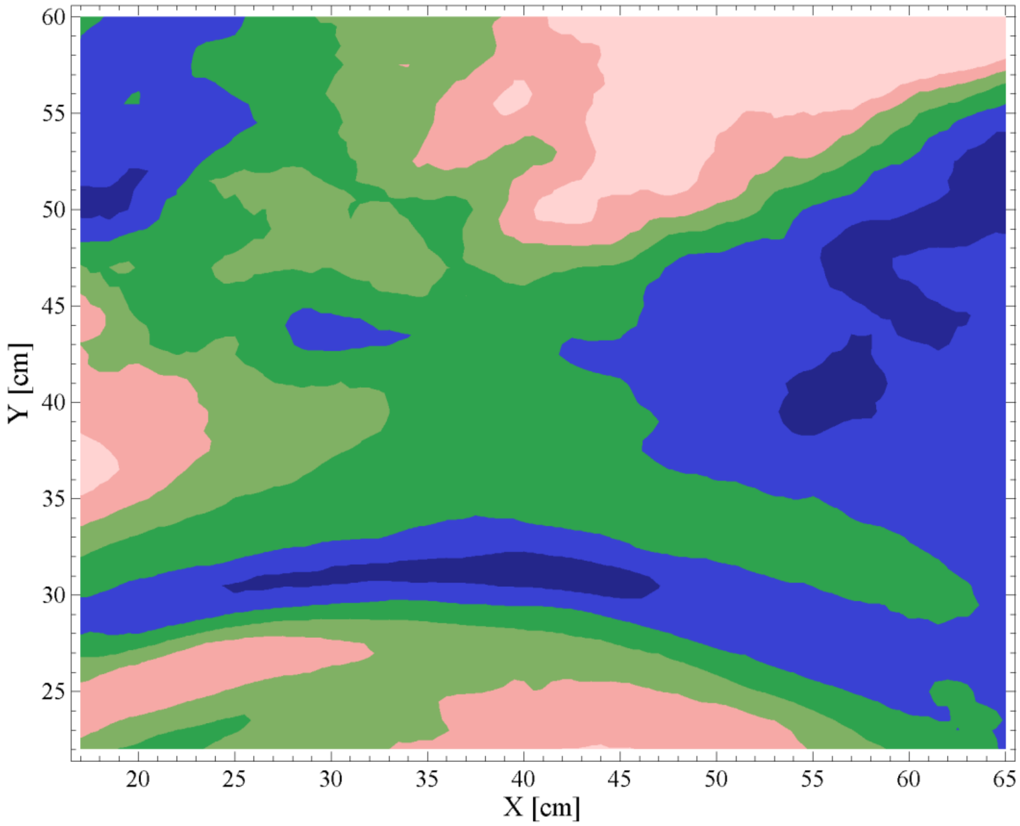

(b)

Figure 5.6 Estimated mean error of (a) the mean values and (b) the variances arising from the finite length of the measurement for the u-velocity components

The estimated normalized errors of the measured mean values are below 10 % in the mean main stream and are below 20 % in the most parts of the measurement field; higher values arise in the areas with low mean velocities (Figure 5.6 a). Though, the higher values are not only a result of dividing by the low mean values according to Eq. (2.25), but are rather a consequence of the high integral time scales (Figure 5.7), which were calculated according to Eq. (2.27).

The estimated normalized errors of the measured variance values are significantly higher in most parts of the flow field (Figure 5.6 b), and it can be recognized on its distribution that it is related to the distribution of the integral time scale (Figure 5.7). Further, its distribution shows a certain similarity to the distribution of the 95%-durations of the variance (Figure 5.5).

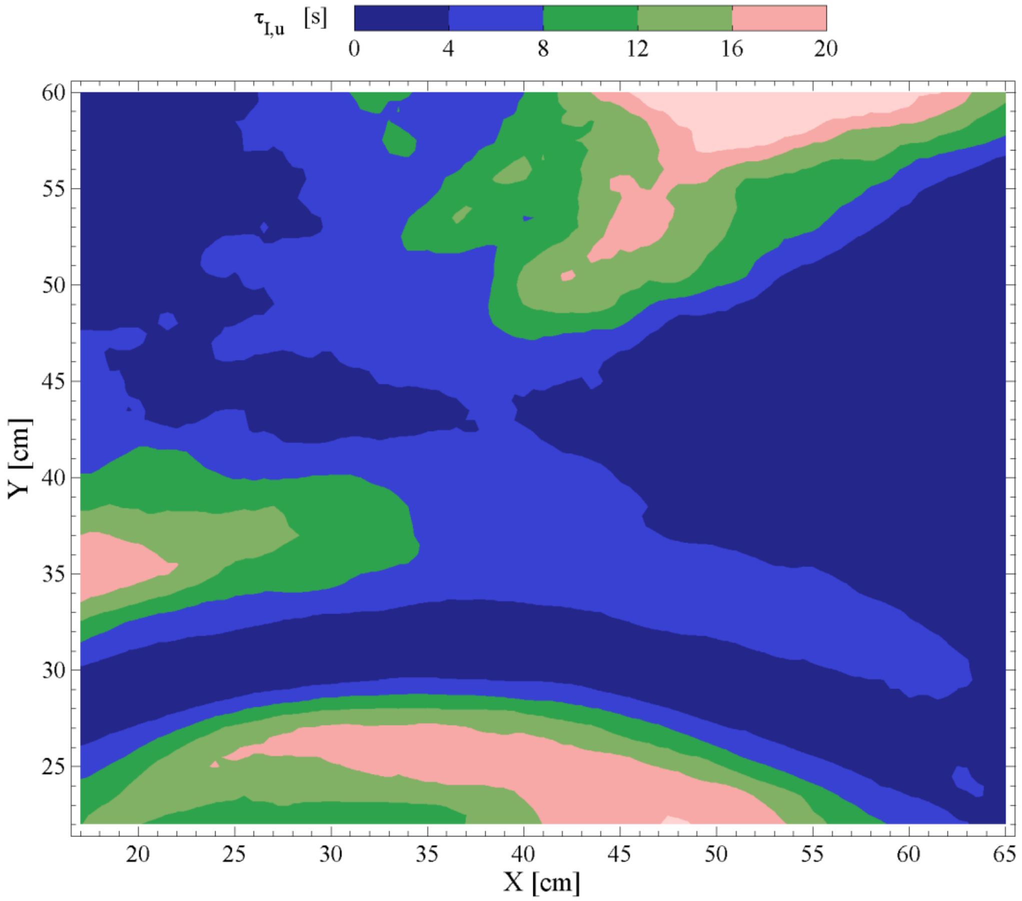

Figure 5.7 Integral time scales of the measured u-velocity components in the measurement field

These results prove that, on the one hand, different areas require different measurement duration for steady statistics and that, on the other hand, different statistical quantities also need different measurement duration. Although the variance values did not reach their steady values, it will be shown in Section 5.3.3 that the captured data is sufficient for the method presented in Chapter 6.

5.2 Inspection of the instantaneous velocity fields

The instantaneous velocity fields of the velocity dataset contain the instantaneous velocity fluctuations in the individual grid points, which appear as a perturbation of the spatial velocity distribution within the vector fields. The main stream is, however, dominant enough to be recognized visually based on the velocity magnitudes in the instantaneous velocity fields (Figure 5.8).

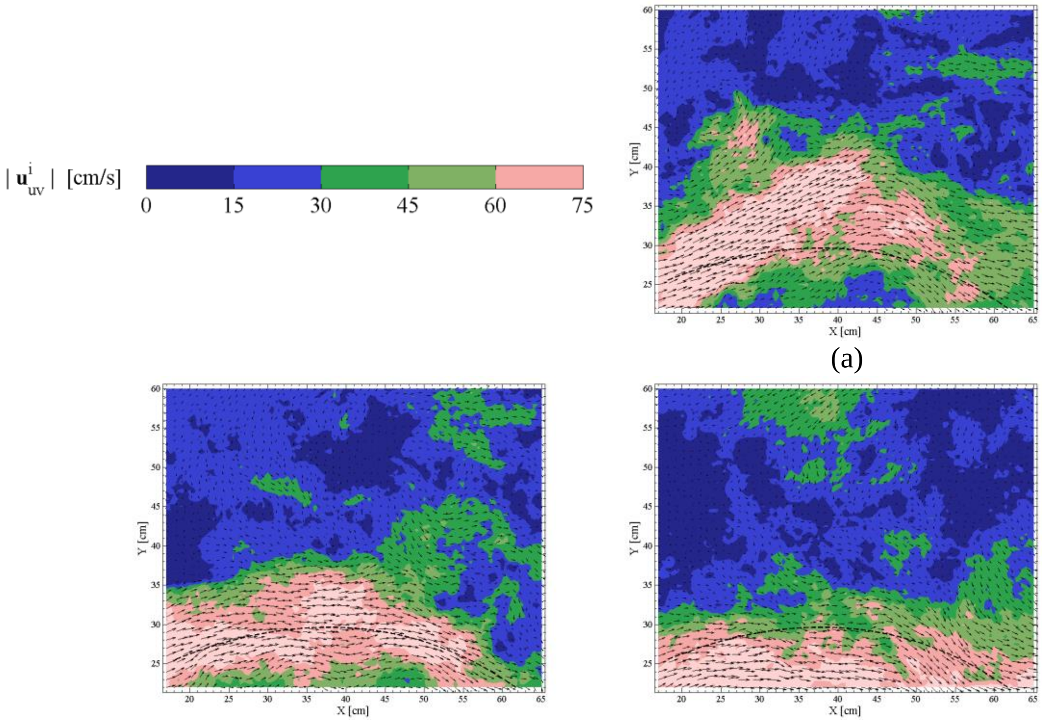

(a)

(b)

(c)

Figure 5.8 Instantaneous velocity fields at different time steps: (a) at 55.895 s, (b) at 62.560 s and (c) at 79.030 s. The dashed line represents the mean main-stream centerline.

By observing a sequence of instantaneous velocity fields, the location of the main stream appears to oscillate around the mean main-stream centerline. Although instantaneous velocity fields shown in Figure 5.8 do not represent one cycle of the oscillation, the different main-stream positions can be well recognized visually. Compared to the mean main-stream centerline illustrated by the dashed line, the instantaneous main stream has a steeper curved trajectory at time step t_I=55.895 s (Figure 5.8 a), while it appears nearly in the same position at time step t_{II}=62.560 s (Figure 5.8 b) and follows a flatter trajectory at time step t_{III}=79.030 s (Figure 5.8 c).

It is reasonable to suspect that the peaks observed in the velocity spectra of the time series (Figure 5.4) are produced by this oscillation. However, although the main stream can be roughly recognized visually, it is a challenge to quantify the frequency or the amplitude of the oscillation based on the instantaneous velocity fields, since the instantaneous positions of the main-stream centerlines are hardly determinable reliably. It has been made attempts to calculate the instantaneous centerlines both by using streamlines and polynomial curve-fitting on the highest velocity magnitudes (see Chapter 6). But streamlines were directed out of the visually recognizable main-stream centerline due to the other flow structures present in the flow fields, and polynomial curve-fitting on the locations with the highest velocity magnitudes also missed the centerline due to the velocities of large flow structures.

Note that the characteristics of the main-stream oscillation are revisited in Chapter 6.

5.3 Proper Orthogonal Decomposition analysis

POD of the measured velocity dataset was computed as described in Section 2.5. The velocity dataset consisting of N=60 000 time steps and M=7 469 two-dimensional velocity vectors per time step yielded 2*M = 14 938 POD modes consisting of 7 469 two-dimensional vectors and corresponding 2*M=14 938 time series of POD coefficients with N=60 000 time steps. As it will be demonstrated later, a POD mode and the corresponding POD-coefficient time series practically form a spatial oscillation. The *contribution of a POD mode i* at time step t_n to the input dataset can be calculated as the product of the vector field of POD mode i and the value of the POD coefficient at the needed time step $a_i(t_n)$, so that the contributions of a POD mode over all time steps yield a spatial oscillation.

In the present section, first the results of POD are presented, and then the applicability of POD is examined for detecting flow structures in the velocity dataset.

5.3.1 Results of POD

The contributions of the individual POD modes to the ensemble turbulent kinetic energy of the measured velocity dataset are shown in Figure 5.9. It can be recognized that the first POD mode has the highest energy contribution and that the contribution of the modes decreases with increasing mode number. The distribution of the turbulent kinetic energy among the POD modes shows a roughly linear relation in a logarithmic scale (Figure 5.10).

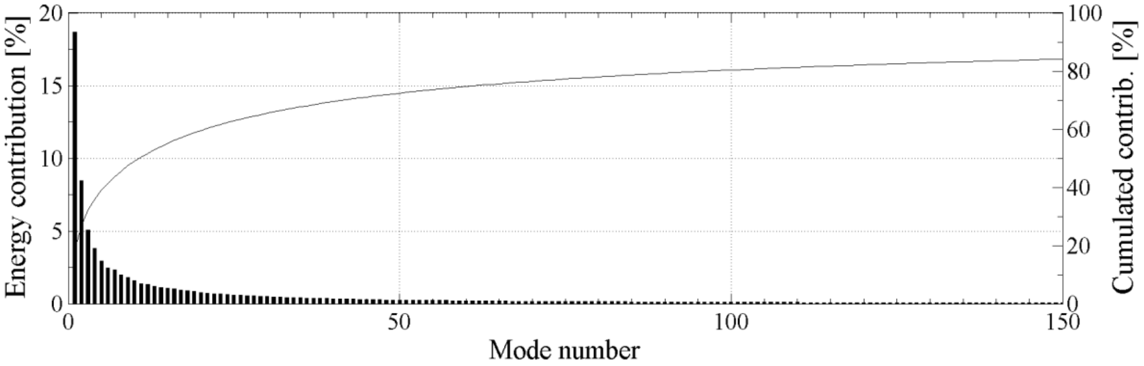

Figure 5.9 Contributions and cumulated contributions of the first 150 POD modes to the ensemble turbulent kinetic energy of the input velocity dataset.

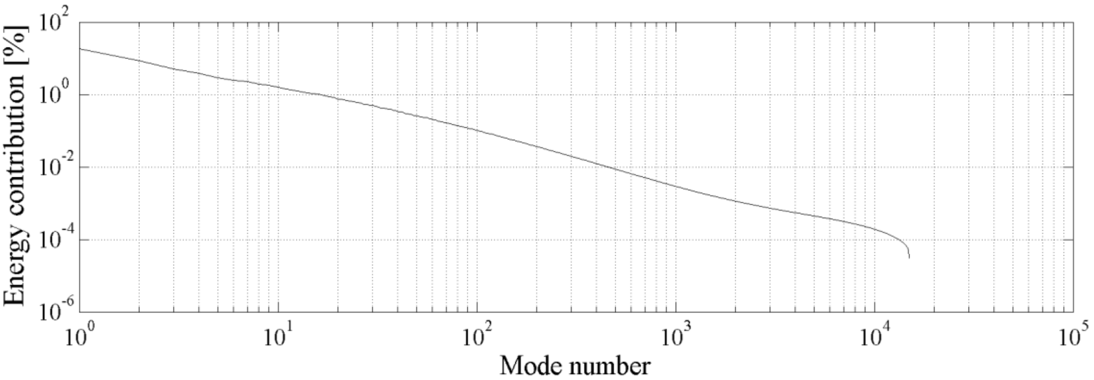

Figure 5.10 Distribution of ensemble turbulent kinetic energy among POD modes

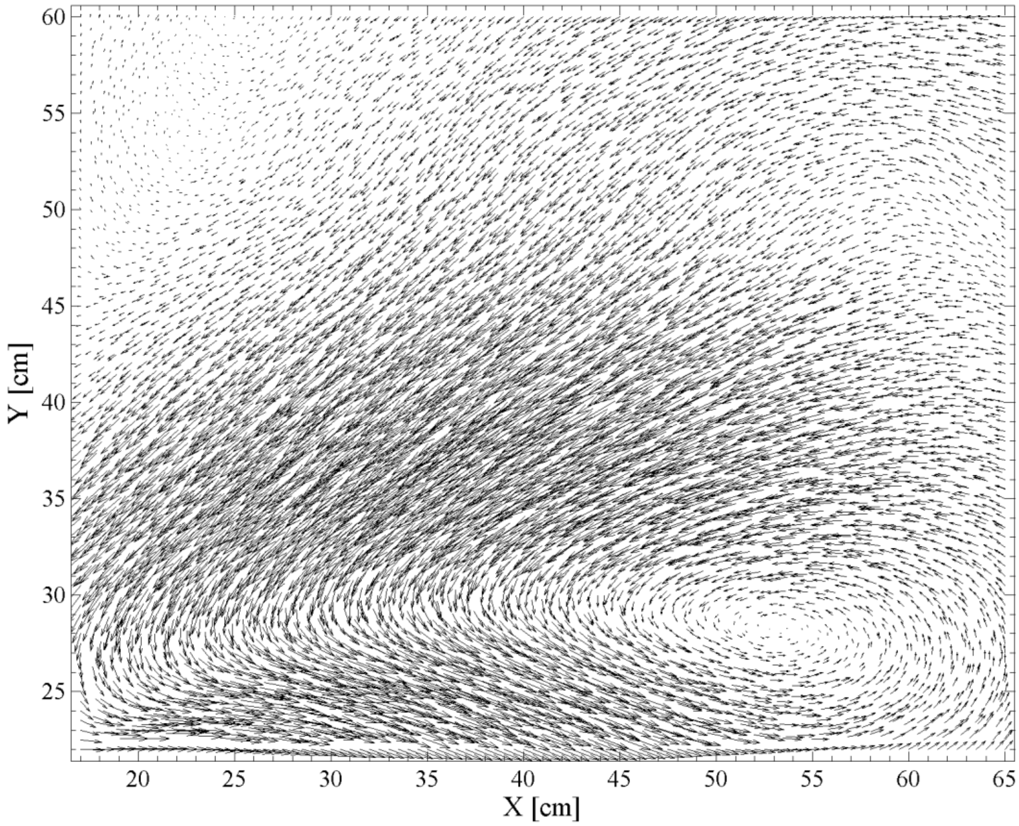

Figure 5.11 POD mode 1

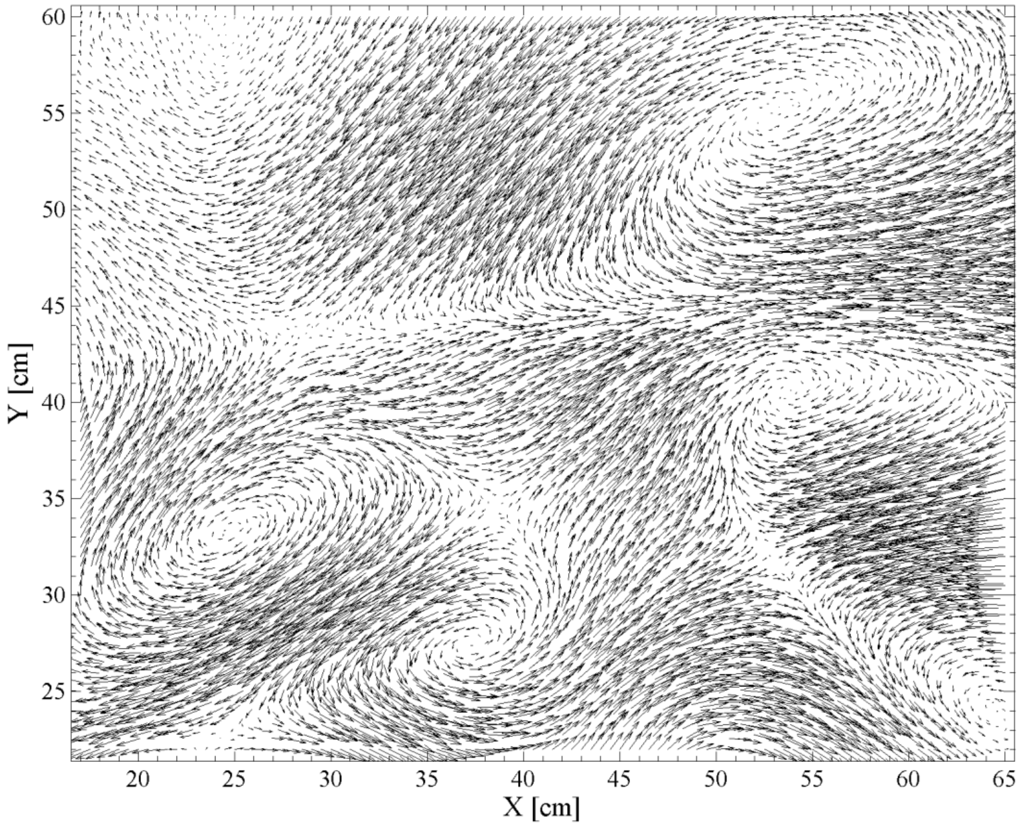

Figure 5.12 POD mode 10

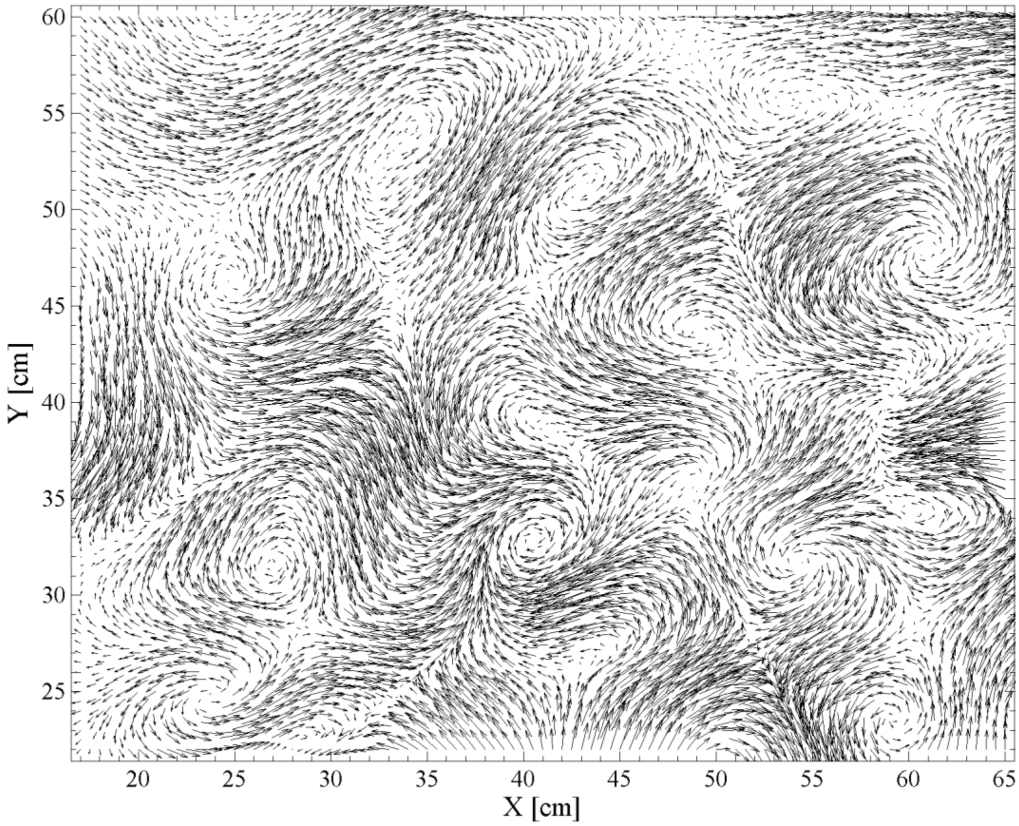

Figure 5.13 POD mode 45

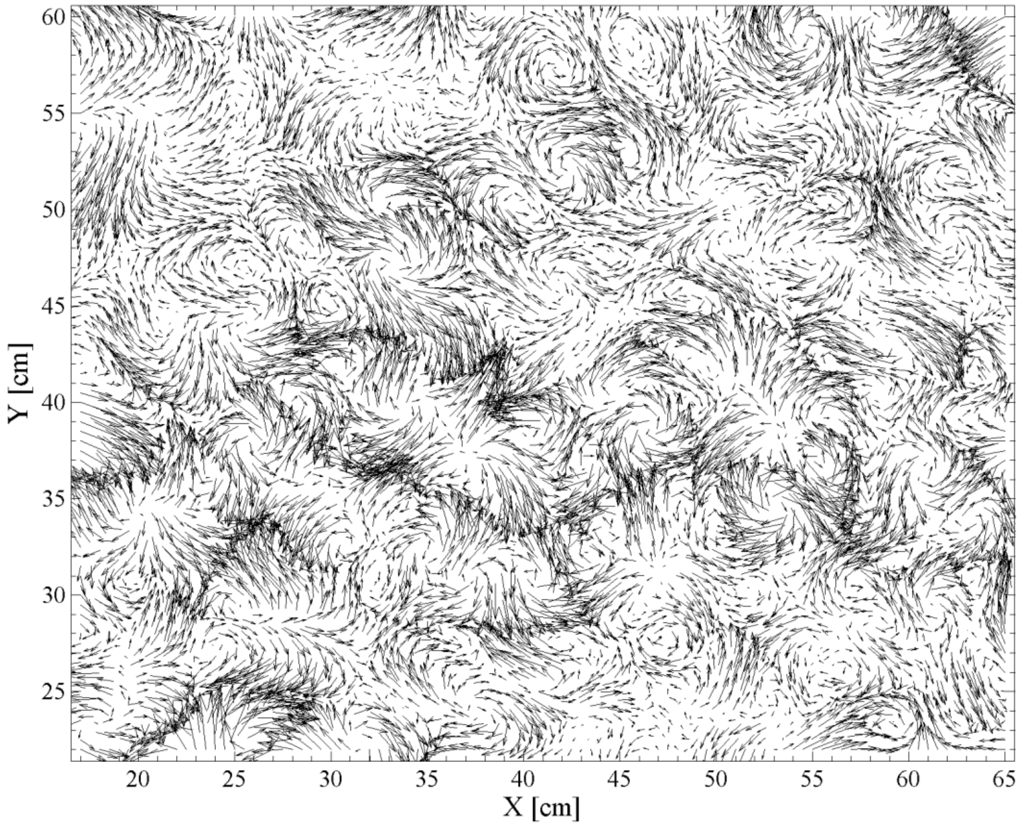

Figure 5.14 POD mode 300

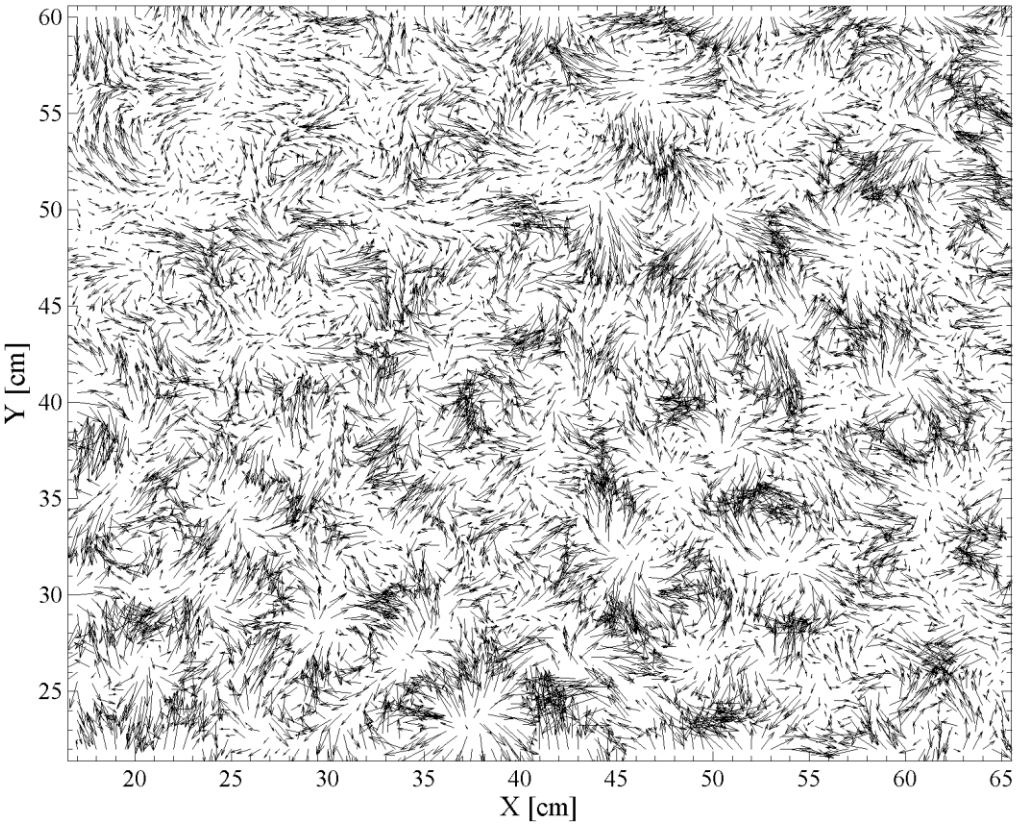

Figure 5.15 POD mode 600

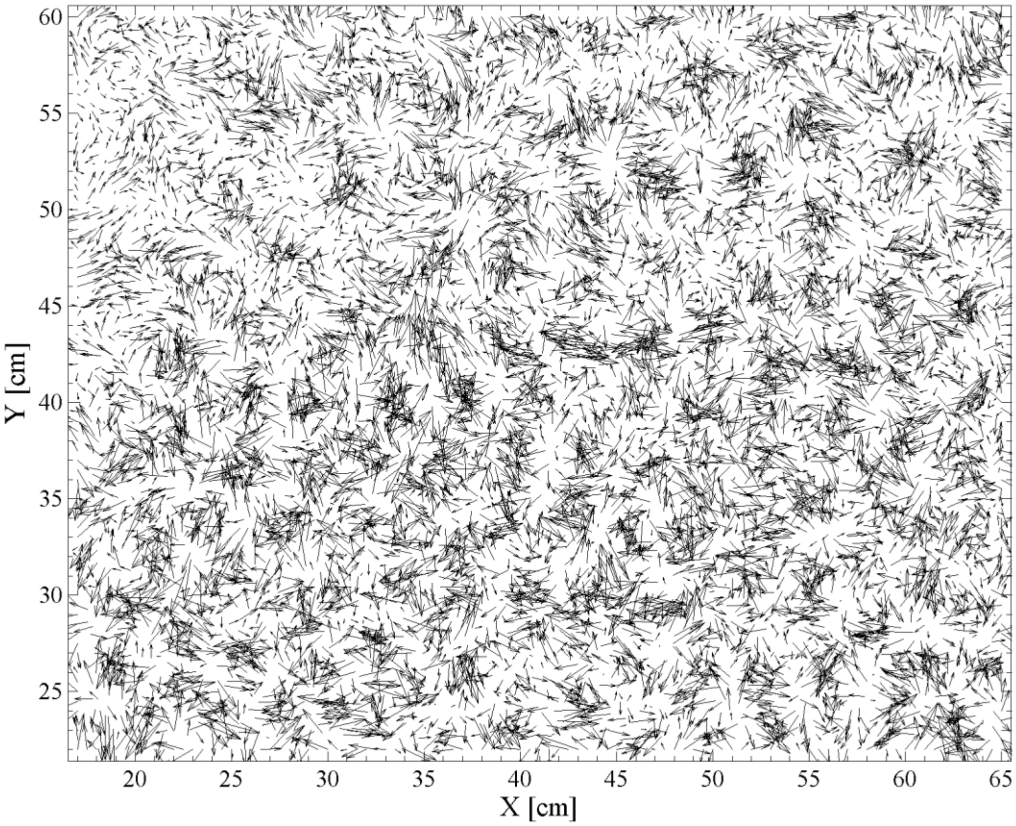

Figure 5.16 POD mode 1390

Since it is not possible to display each of the 14,938 POD modes in a printed work, only POD modes 1, 10, 45, 300, 600 and 1390 are presented here explicitly in order to show the tendencies in the characteristics of the POD modes and POD coefficients. POD mode 1390 was selected, because a reconstruction using modes 1 to 1390 reproduces 95 % of the total ensemble turbulent kinetic energy.

The selected POD modes are shown in Figures 5.11 - 5.16. Note that the same vector scale has been used in these plots and that the vector lengths are in the same range, since POD modes are orthonormal, not just orthogonal. It can be observed that the vectors of the POD modes typically form structures, which are of similar size within the individual modes. As it will be shown in Section 5.3.2, these structures are not flow structures but the spatial patterns of the oscillations produced by the POD modes. The higher the mode number is, the smaller the typical size of the structures is, so that in POD modes of very high order not even clear structures can be recognized (Figure 5.16).

In order to visualize the tendency of decreasing typical structure sizes with increasing POD mode numbers, the characteristic length scales of the individual POD modes were calculated as described in Section 2.4. The characteristic length scales of the POD modes appear to show a roughly linear tendency on a logarithmic scale (Figure 5.17). It has to be noted that although the described method is intended for homogeneous fields, it was applicable because the structures are usually of similar size within an individual POD mode.

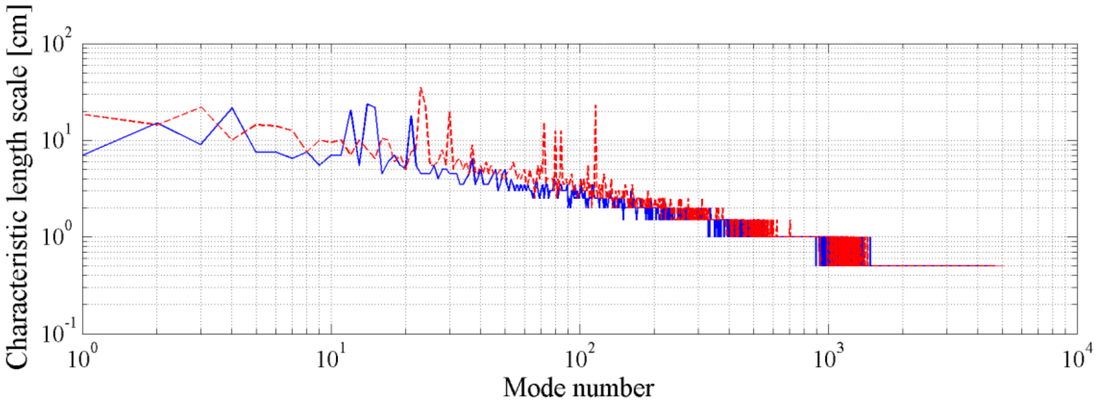

Figure 5.17 Characteristic length scales of POD modes in x- (dashed line) and in y-direction (solid line).

The POD-coefficient time series corresponding to the selected POD modes are displayed in Figures 5.18 and 5.19. These show that the higher the mode number, the smaller the coefficients values, hence the amplitudes. The frequency spectra of these POD coefficients (Figures 5.20 and 5.21) show that the higher the mode number is, the higher frequencies are involved.

These characteristics of the POD results demonstrate that the spatial size of the oscillating structures and the amplitudes of the oscillation decrease with increasing mode number, while the frequencies of the oscillations increase.

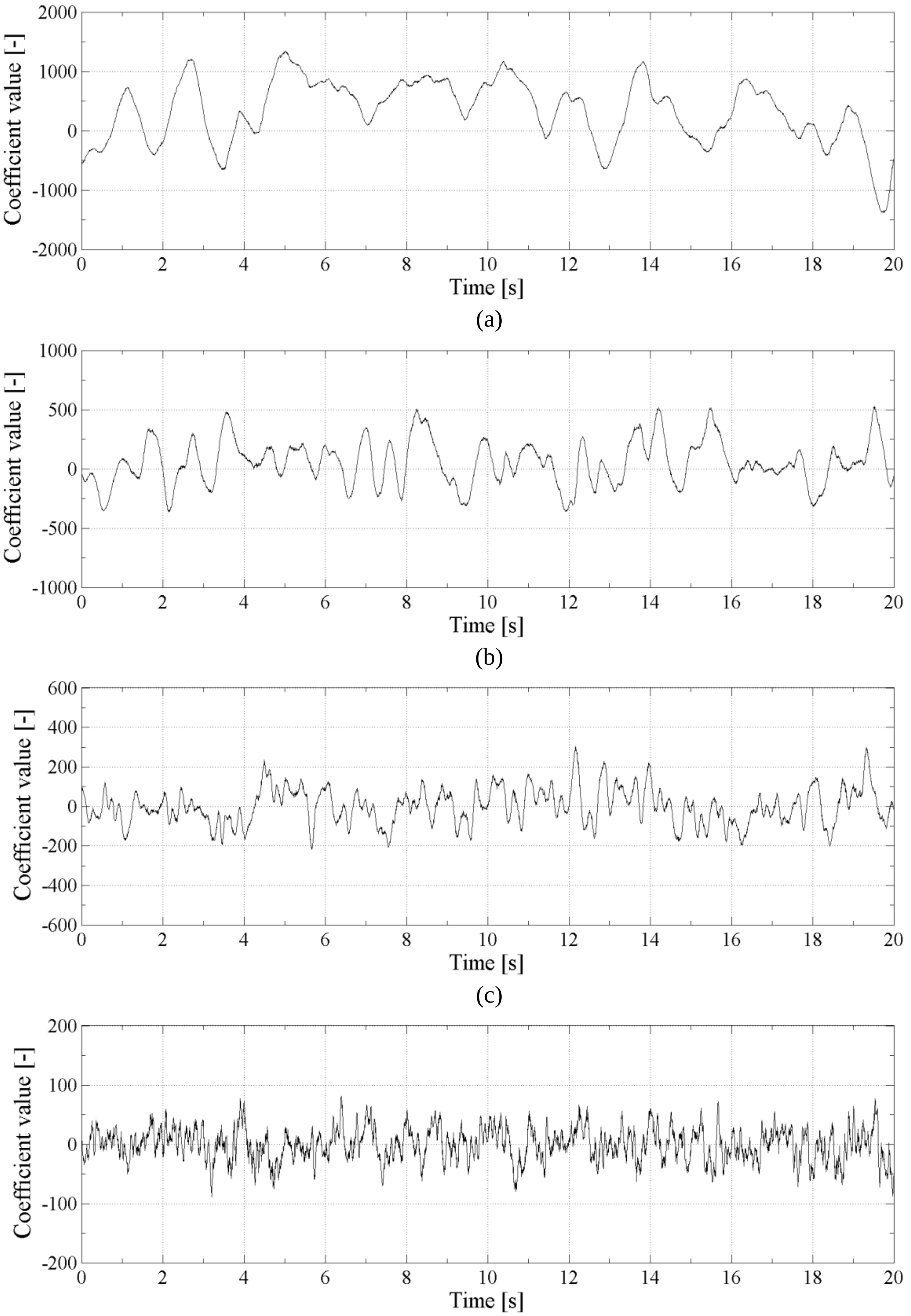

(a)

(b)

(c)

(d)

Figure 5.18 Time series of the POD coefficients corresponding to (a) mode 1, (b) mode 10, (c) mode 45 and (d) mode 300

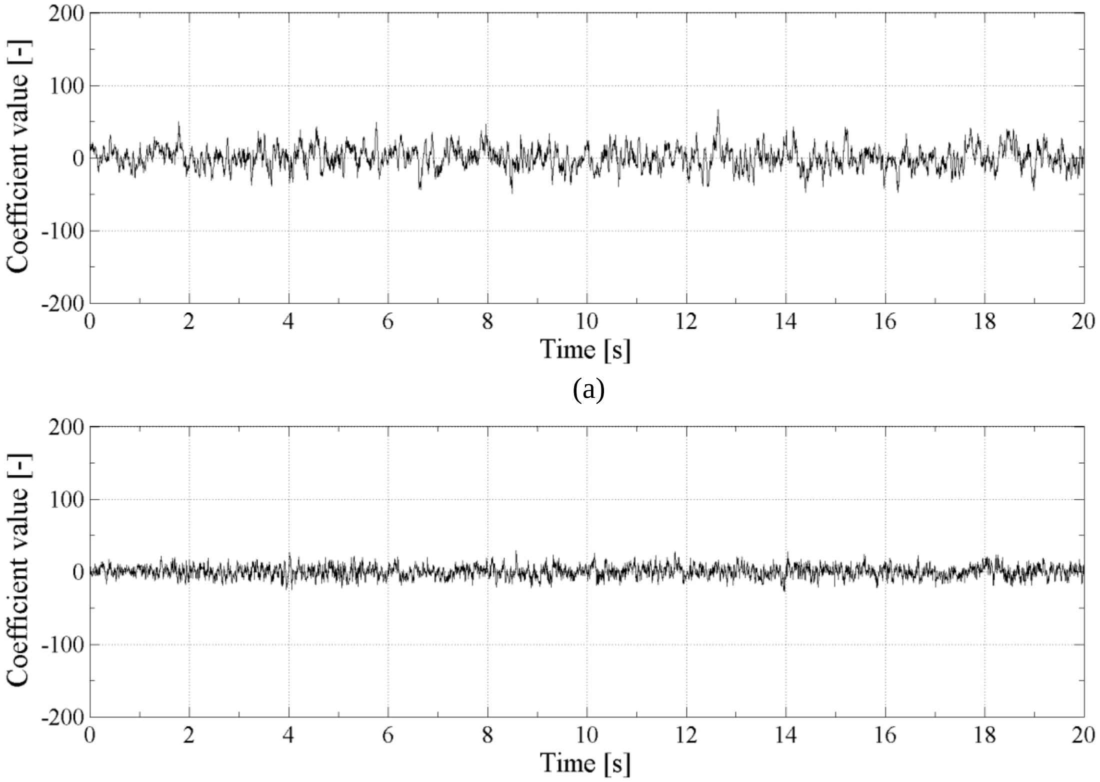

(a)

(b)

Figure 5.19 Time series of the POD coefficients corresponding to (a) mode 600 and (b) mode 1390

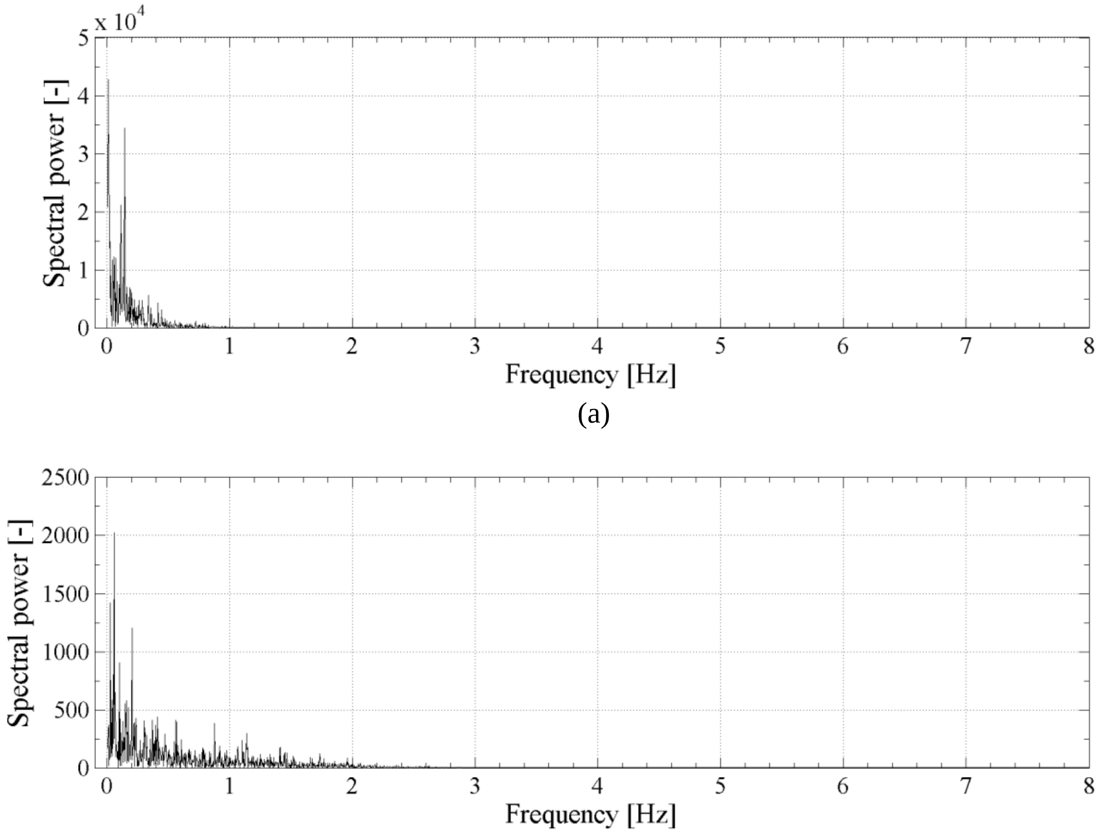

(a)

(b)

Figure 5.20 Frequency spectra of the POD coefficients corresponding to (a) mode 1 and (b) mode 10

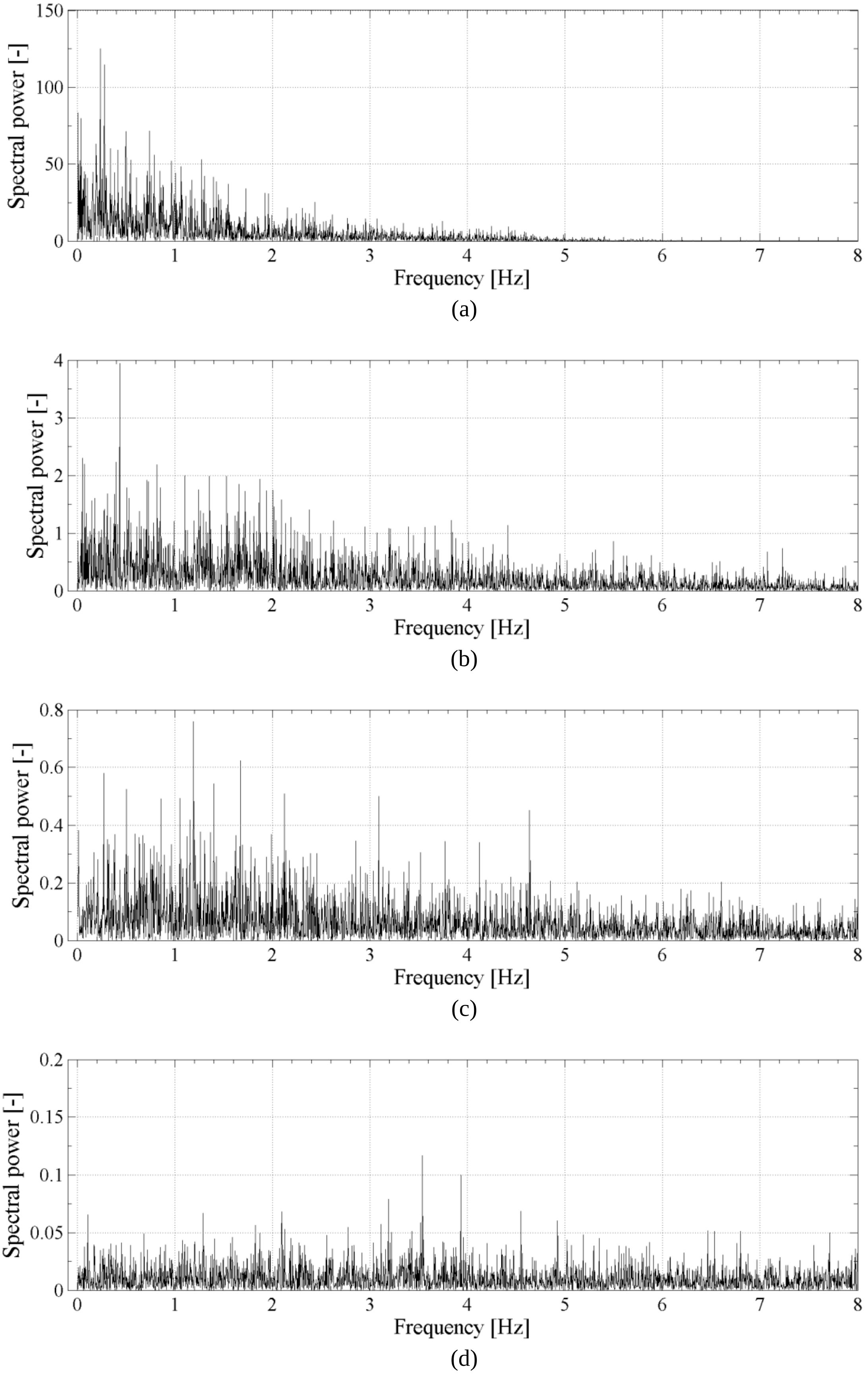

Figure 5.21 Frequency spectra of the POD coefficients corresponding to (a) mode 45, (b) mode 300, (c) mode 600 and (d) mode 1390

5.3.2 On the interpretation of the POD results

The vortical structures that can be observed in the vector fields of POD modes are by themselves not extracted flow structures. This can be demonstrated using the contributions of POD mode 45 to the reconstructed dataset at different time steps. As mentioned before, the contribution of POD mode i at time step t_n can be calculated as the product of the vector field of POD mode i and the value of the POD coefficient at the needed time step $a_i(t_n)$. Accordingly, Figure 5.22 shows the contributions of mode 45 at two time steps with different POD coefficients; the value of the coefficient is a_{45}= 200 in Figure 5.22 (a) and a_{45}= -200 in Figure 5.22 (b). It can be seen that the sign of the coefficient determines the rotation direction of the vortical structures in the contribution of the POD mode. Following Eq. (2.39), the sum of a POD coefficient a_i over the time is zero. Consequently, the contribution of a POD mode occurs similar frequently with both rotation directions. As it is highly improbable that turbulent eddies of same size but opposite rotation direction occur at the same location alternately in turbulent flows, the POD modes are by themselves not extracted flow structures, but just oscillation components needed to reproduce the input dataset.

Since the velocity dataset can be reconstructed using the combination of the POD modes, it is obvious, that flow structures evolve in the reconstructed dataset as the combined contribution of the POD modes, hence as the superposition of the oscillations.

However, structures evolving in the combination of arbitrary POD modes are also inappropriate to be considered as flow structures, similarly to the vortical structures in the individual POD modes. This can be well demonstrated using the reconstructed velocity field at time step t =2.070 s. The velocity field reconstructed using POD modes 1-45 contains two marked distinct vortical structures (Figure 5.23). These are neither present in the velocity field reconstructed using POD modes 1-17 (Figure 5.24), nor in the velocity field reconstructed using POD modes 18-45 (Figure 5.25), although the sum of these POD modes contain them. Furthermore, none of the POD modes from 18 to 45 contain vortical structures with the same center positions as the marked structures.

Consequently, flow structures evolve as the combination of several POD modes, and it is a challenge to find the POD modes necessary for the reconstruction of a particular eddy of interest. This also implies that excluding arbitrary POD modes probably excludes only some portions of flow structures, so that the structures in the reconstructed data become distorted.

Studies that described flow structures using POD have identified the necessary POD modes based on connections between the contributing POD modes, like the almost identical energy contributions or identical characteristic frequencies of POD coefficients (e.g. Bernero et al. 2000, Meyer et al. 2007, Feng et al. 2011). Note that the flow structures described by POD in such studies occurred repeatedly in the same positions, hence they were mostly oscillations.

Since the energy contributions of modes, the sizes of the vortical structures within modes and the frequencies of the POD-coefficient time series show a continuous transition from mode to mode in the present data, identities mentioned above were not found between the modes of the present dataset. This will be revisited in Chapter 6.

The only POD mode that could not be involved in such an examination is POD mode 0, i.e. the mean velocity field, as it has no POD coefficients and no turbulent kinetic energy contribution. Since the mean velocity field is not homogeneous and consists of a structured vector field (Figure 5.1), its modulation may result in structures not present in the vector fields of POD modes and had to be examined explicitly.

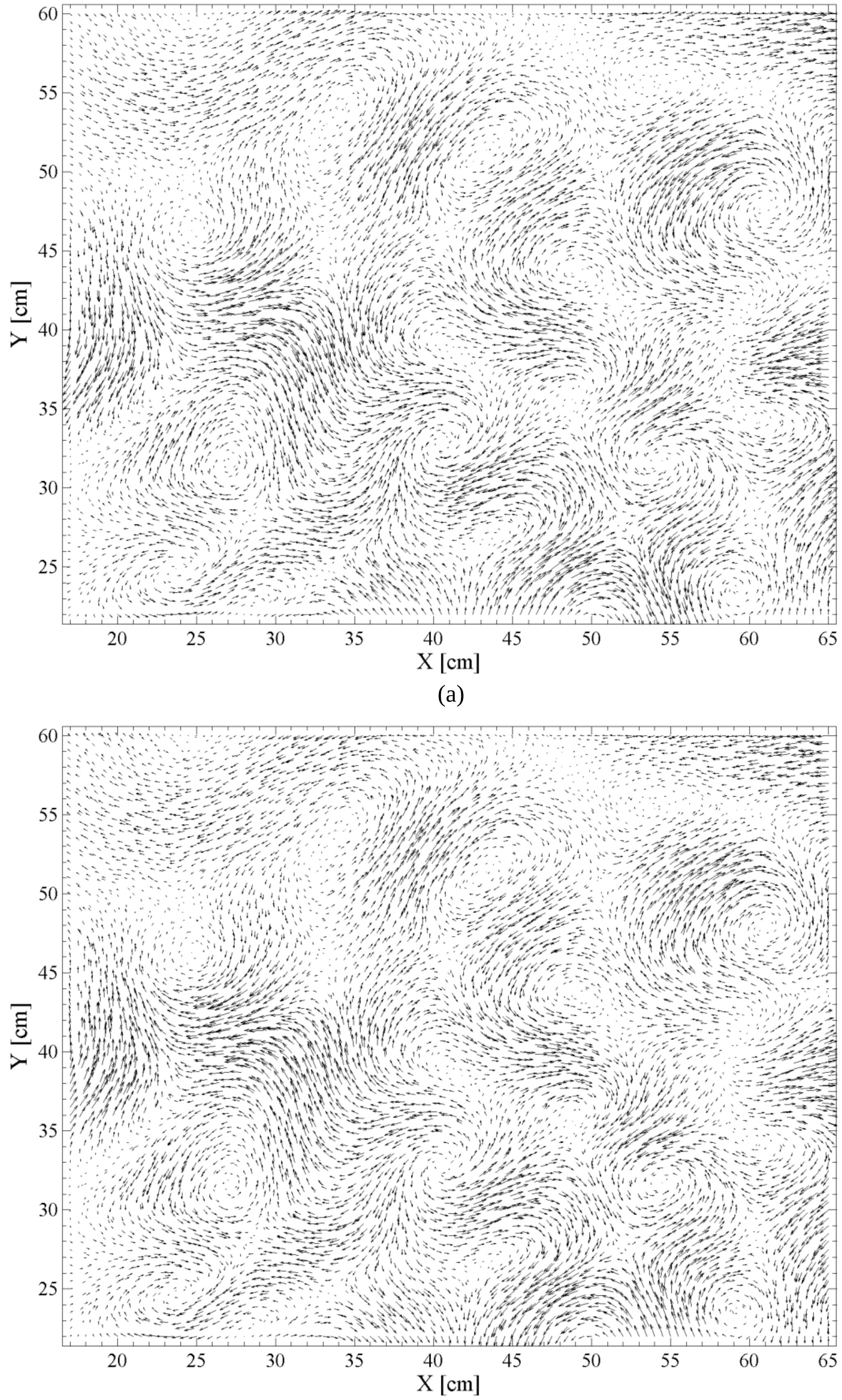

(a)

(b)

Figure 5.22 The contribution of POD mode 45 at different coefficients (a) a=200 and (b) a= -200

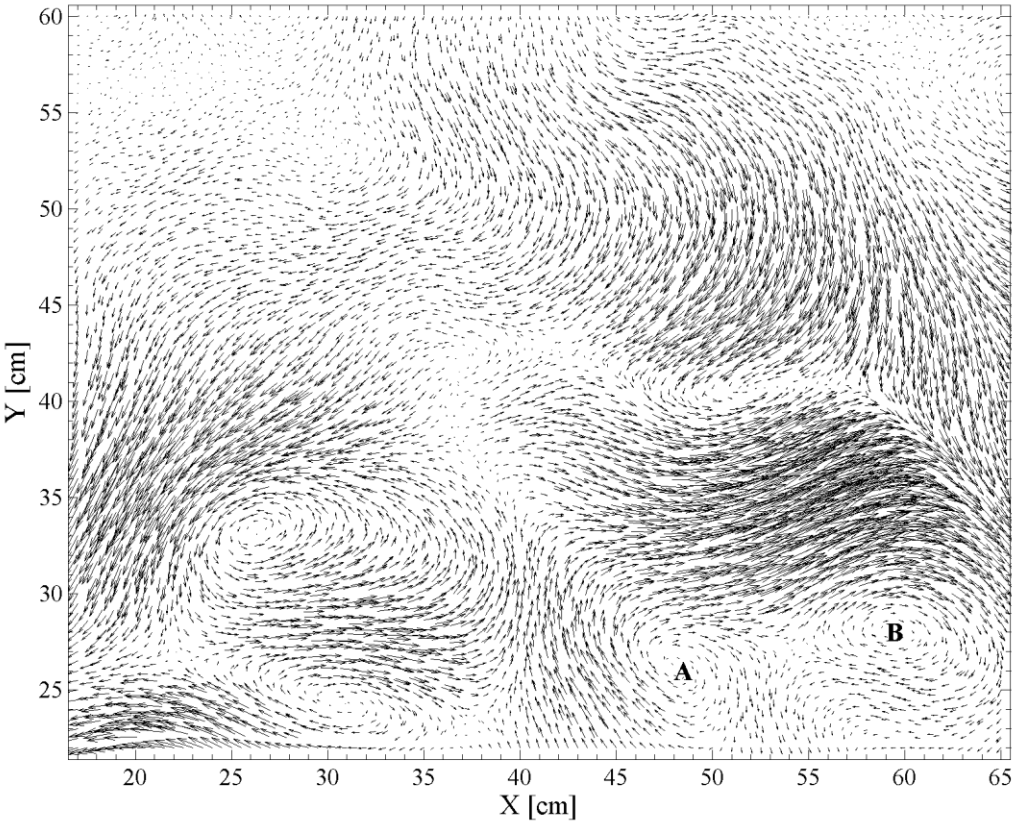

Figure 5.23 The combined contribution of POD modes 1-45 at the time step t =2.070 s

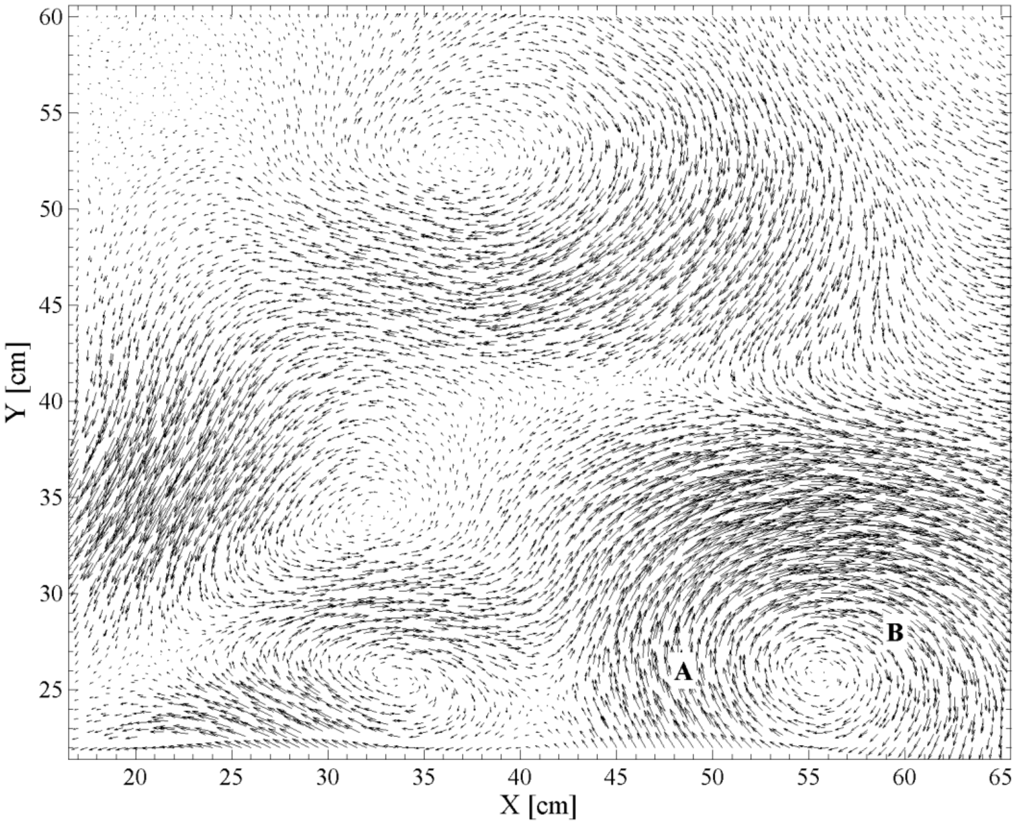

Figure 5.24 The combined contribution of POD modes 1-17 at the time step t =2.070 s

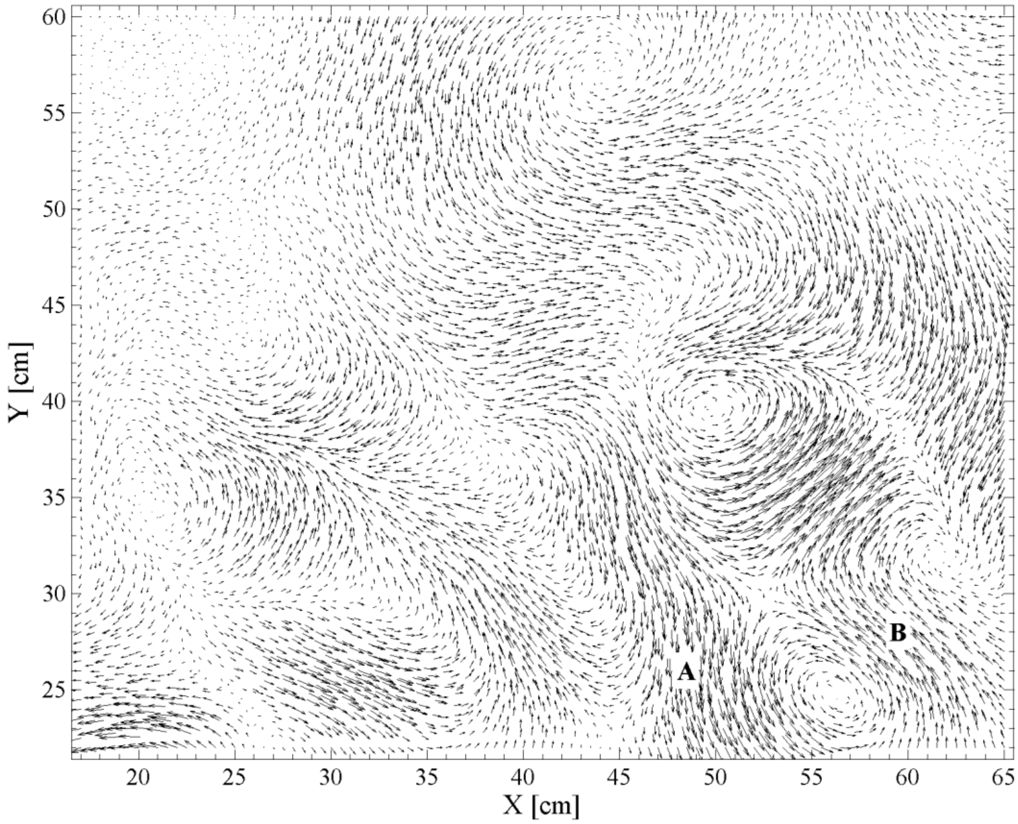

Figure 5.25 The combined contribution of POD modes 18-45 at the time step t =2.070 s

Figure 5.26 (a) shows the contribution of POD mode 1 at three time steps with significantly different POD coefficients: a_1~ -1200 at t_I=55.895 s (Figure 5.26 a/I), a_1~ 0 at t_{II}=62.560 s (Figure 5.26 a/II), and a_1= +1000 at a time step t_{III}=79.030 s (Figure 5.26 a/III). As demonstrated before, the sign of the coefficient determines the rotation direction of the vortical structure in the contribution of the POD mode (Figure 5.26 a). Figure 5.26 (b) contains the reconstructed velocity data using the POD modes 0 and 1, denoted as POD modes 0-1. It can be recognized that the result of the modulation by POD mode 1 is a displacement of the main-stream location. The impact of POD mode 1 on the main stream can be visually compared with the raw velocity fields at different time steps in Figures 5.26 (b-c). It can be recognized that the displacement of the main stream observed in the modulated mean flow corresponds roughly the displacements observed in the raw velocity data.

Note that the oscillating main stream is recognizable in the reconstructed velocity field, but not in the vector field of the POD mode. In other words, the oscillating main stream evolves as flow structure by the combination of POD modes 0-1, but in the sense of the oscillation components it is represented by a single POD mode.

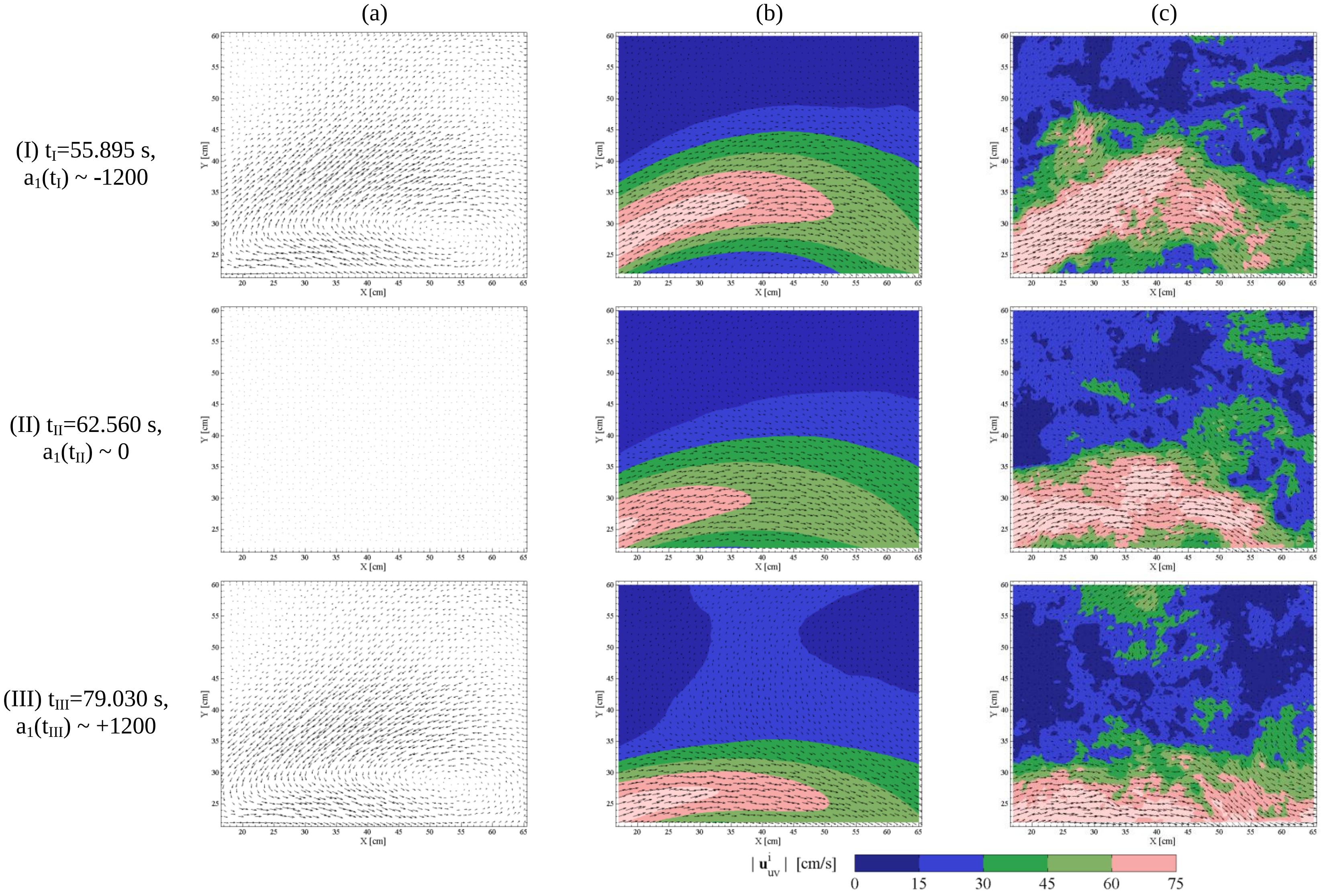

Figure 5.26 Velocity fields at three time steps (I-III) with different contributions of POD mode 1; (a) the contribution of POD mode 1, (b) the velocity fields reconstructed using POD modes 0-1 and (c) the raw velocity fields.

It can be deduced that flow structures with different moving patterns are represented differently in POD modes, according to the turbulent kinetic energy representation of POD modes, as follows. Flow structures that occur at the same locations repeatedly, introduce a considerable amount of turbulent kinetic energy at those locations and, especially large structures involving larger areas, therefore usually generate a few number of POD modes representing the structure. Flow structures, in turn, that do not occur at the same locations repeatedly but are, for example, convected with the flow do not produce high fluctuation power at fixed locations, and are not going to be represented by few POD modes. Hence, if there are large flow processes occurring repeatedly at the same locations, they are going to be represented by POD modes of high energy contributions, while fluctuations of other flow structures have to be reconstructed by the combination of several POD modes.

Further, it is reasonable to assume that flow structures occurring repeatedly at nearly but not exactly the same position generate a POD mode of high energy contribution containing a kind of spatial intersection of the occurrences, and the exact position is reproduced by involving further POD modes to the reconstruction. This implies that a reconstruction involving only the POD mode containing the intersection of such flow structure is not going to reproduce the flow structure exactly. However, as it will be seen in Chapter 6, the POD mode containing the intersections is suitable for investigating the occurrences of such flow structures.

5.3.3 On the convergence of POD results

Since POD modes are computed as a set of optimal basis functions of the given input velocity dataset, variations in the input dataset have consequently an impact on the POD results. Therefore, the impact of the measurement duration on the POD results was explicitly investigated. Such an examination is, however, computationally quite extensive, since the POD results have to be computed for each selected duration. For this reason, this examination was undertaken based on the POD results of only three durations: 3-, 4- and 5-minutes durations. The velocity datasets of 3- and 4-minutes durations were fragments of the available 5-minutes long measurement, both with the same initial time step as the original dataset. The convergence of the results is examined here by comparing the results of different durations.

The distributions of turbulent kinetic energy contributions among POD modes resulting from different measurement durations yield nearly the same result (Figure 5.27); a difference can be only recognized at the highest mode numbers.

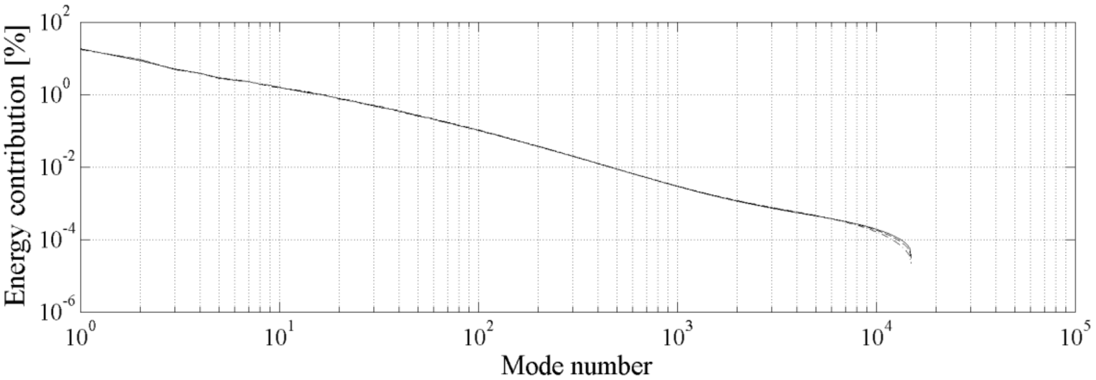

Figure 5.27 Distributions of turbulent kinetic energy among POD modes resulting from different measurement durations; dashed line: 3-minutes, dashed-dot line: 4-minutes, solid line: 5-minutes.

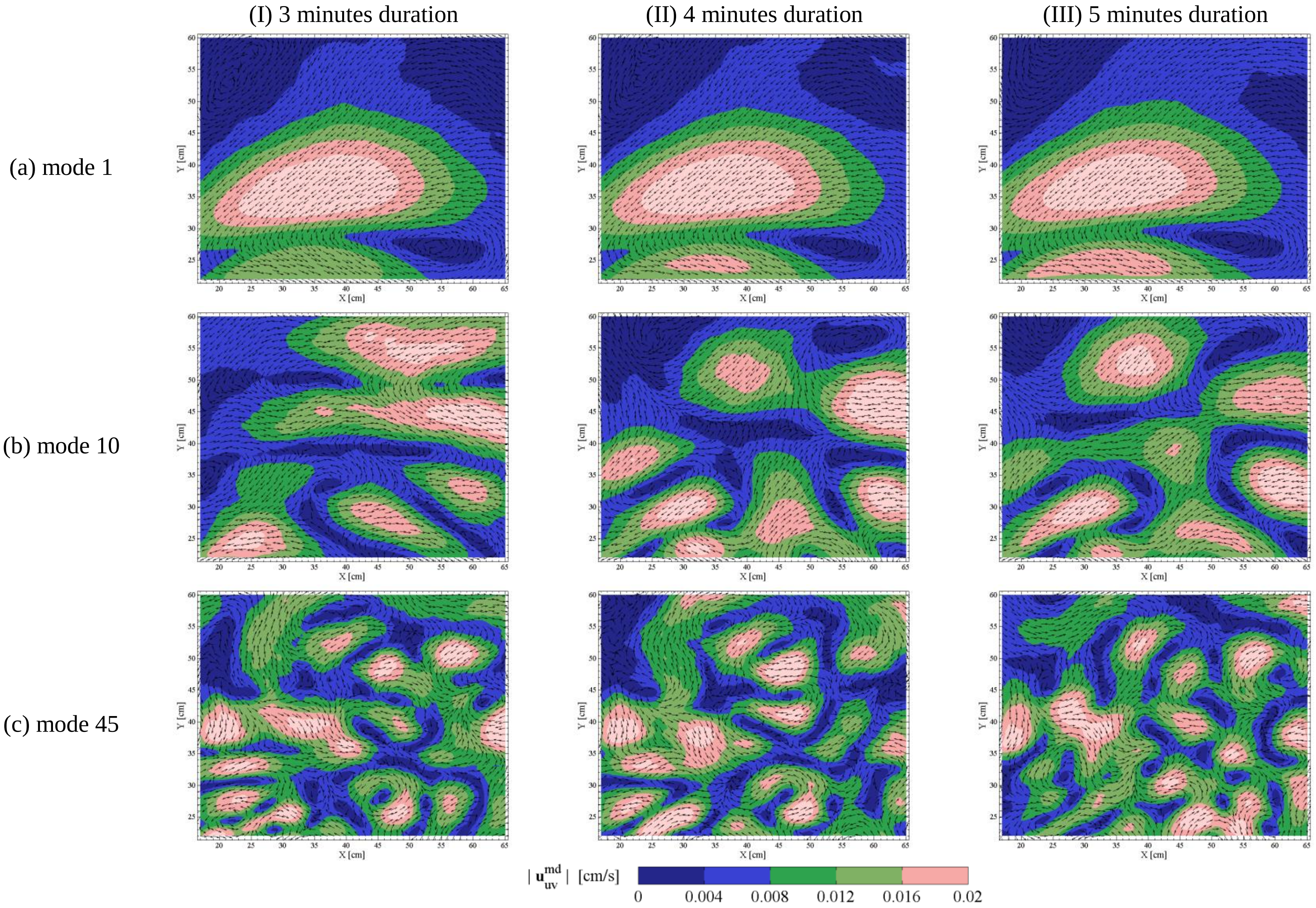

Figure 5.28 POD modes 1, 10 and 45 resulting from different measurement durations. The vectors are displayed as unit vectors; the color contours show the vector magnitudes and the contour levels are the same for all subfigures.

As illustrated by Figures 5.28 (a-c), POD modes of different mode numbers are changed to different extent with increasing duration. While the first POD modes change little (Figure 5.28 a), low-order POD modes appear to converge with increasing duration (Figure 5.28 b). The higher the mode number is, the more dissimilar the POD modes are at different durations (e.g. Figure 5.28 c).

A similar tendency can be observed in the time series of the POD coefficients arising from different measurement durations (Figure 5.29); the lower the mode number is, the more similar are the curves of the time series. Note that the offset in the coefficient time series corresponding to POD mode 1 can be explained by the different mean velocity fields resulting from the different durations. A quantitative comparison of the coefficient time series arising from different durations is not performed here, since such a comparison has to consider the different mean velocity fields, which, however, requires more sophisticated methods, like the Common Base POD (Kriegseis et al. 2010).

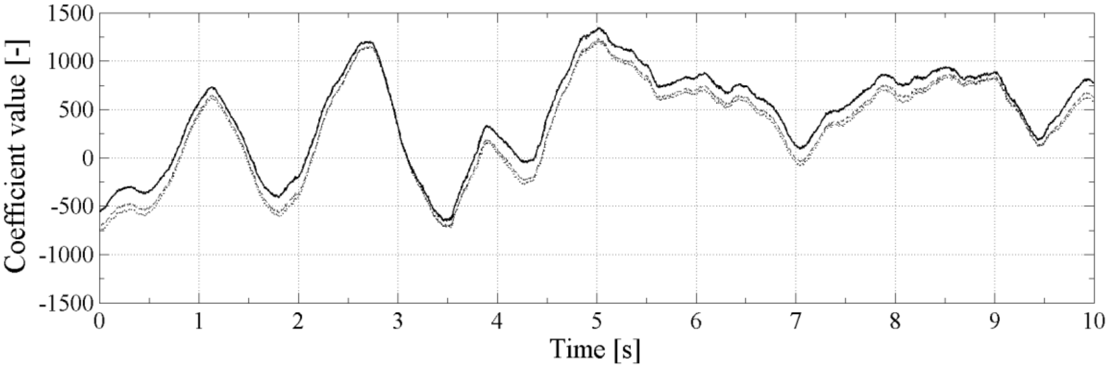

(a)

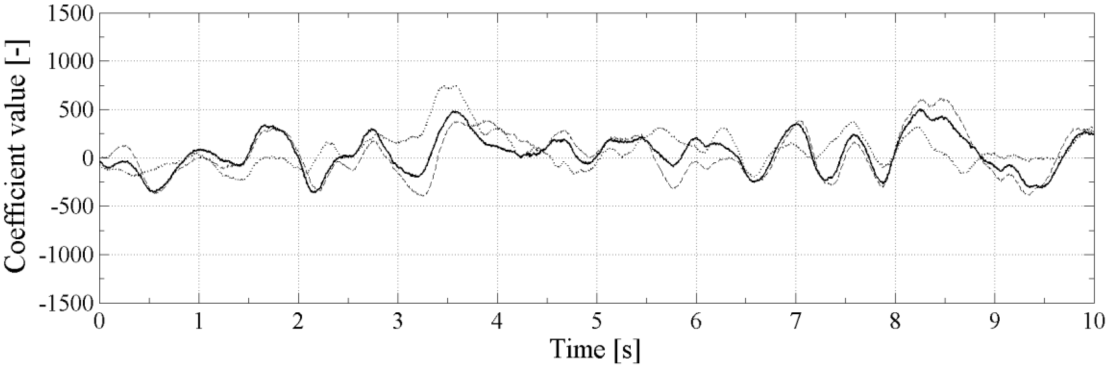

(b)

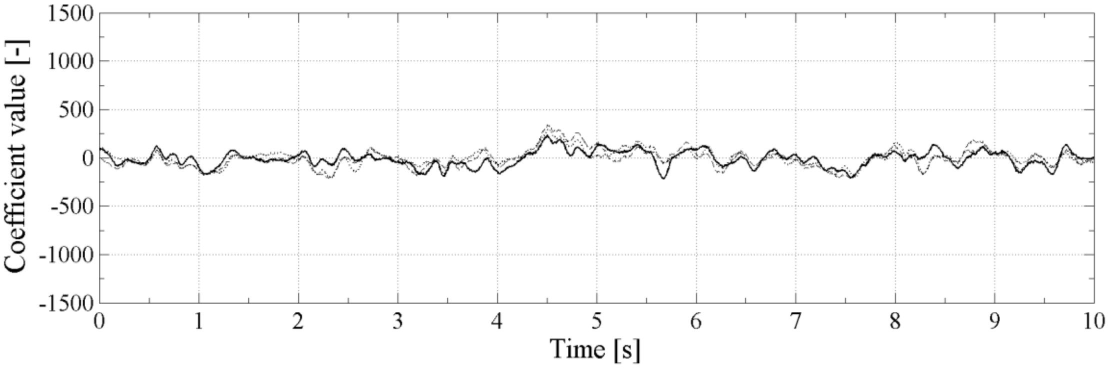

(c)

Figure 5.29 POD coefficients resulting from different measurement durations: (a) modes 1, (b) mode 10 and (c) mode 45. Dotted line: 3-minutes, dashed line: 4-minutes and solid line: 5-minutes duration.

It can be concluded, that although the POD results are adjusted to the changed content of the input velocity dataset, low-order POD modes prove to converge to steady vector fields and the first modes obtain a nearly steady content already at shorter measurement durations.

Considering that POD results are intended to be used to identify repeating flow processes, practical significance on the reproducibility of the results is obtained by comparing POD results of independently performed measurements of the same flow. For this purpose, the results of two shorter but overlapping fragments, the first 3-minutes and the last 3 minutes of the available 5 minutes long measurement are compared in the following. Since only low-order POD modes appeared to be nearly steady for 3-minutes duration in the previous analysis, only low-order POD modes are compared here.

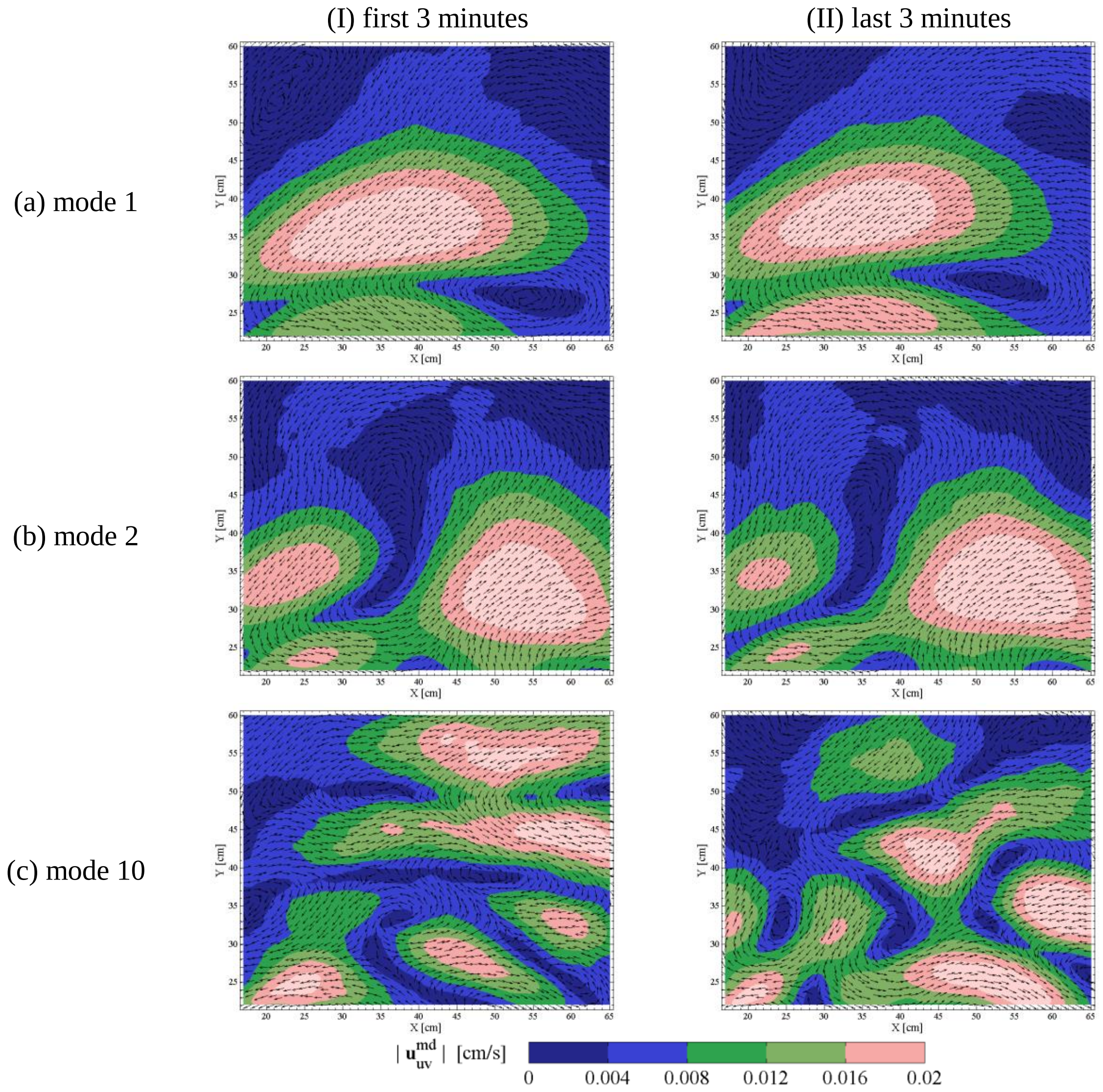

Figure 5.30 Comparison of POD modes resulting from the (I) first and (II) the last 3-minutes fragments of the available measurement: (a) POD mode 1, (b) POD mode 2 and (c) POD mode 10

The comparison of the POD modes resulting from the two fragments show that while the first POD modes show a high degree of similarity (e.g. Figures 5.30 a-b), the higher the mode number is, the less resemblance can be recognized between the POD modes arising from the two 3-minutes fragments (e.g. Figures 5.30 c).

The overlapping one minute long period of the two fragments permits the direct comparison of the POD-coefficient time series (Figure 5.31). The comparison reveals that the curves of the time series corresponding to the same mode number show high similarity at low mode numbers, which decreases with increasing mode number.

Briefly, POD results are computed to reproduce the input dataset; hence they are adjusted to the patterns in the particular input dataset. Although the 3 minutes duration proved to be too short to get steady POD results in the previous subsection, POD of two, in large parts different 3-minutes long velocity datasets of the same flow lead to nearly the same POD results at low mode numbers and the corresponding POD-coefficient time series followed systematic patterns. This affirms that low-order POD modes represent processes that occur repeatedly in the flow.

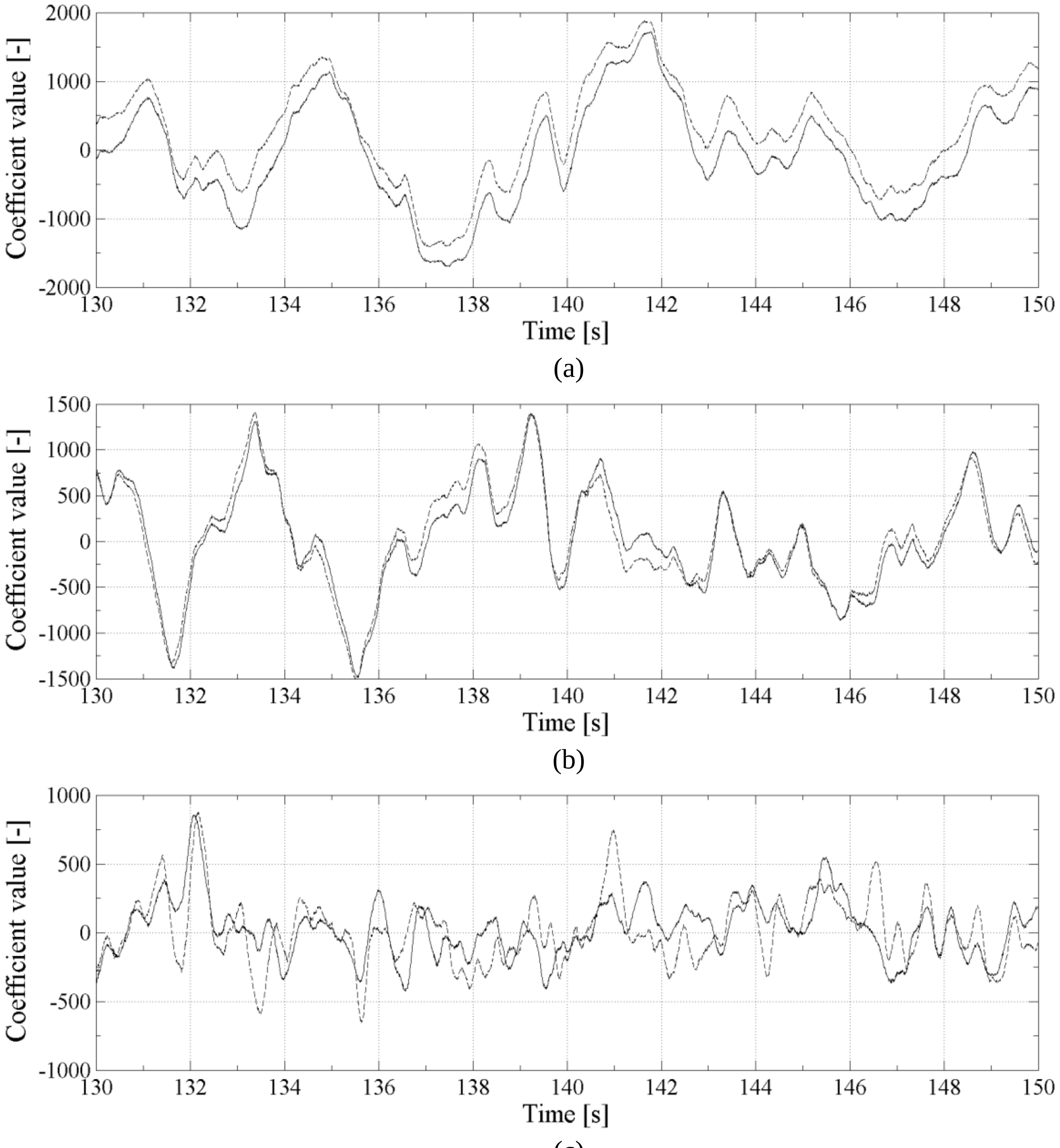

Figure 5.31 Comparison of POD coefficients resulting from the first (solid line) and the last (dashed line) 3-minutes fragments of the available measurement: (a) POD mode 1, (b) POD mode 2 and (c) POD mode 10.

5.4 Summary

The mean velocity field of the measurement confirmed that both parts of the main stream and parts of the recirculation region were included in the measurement field, which leads to an inhomogeneous mean flow field. Although the main stream appears to be clearly recognizable in the mean velocity field, observing the instantaneous velocity field of sequential time steps reveals that the main stream is oscillating, which is not recognizable based on the mean flow field.

The velocity spectra of the velocity time series show a clear -5/3 slope in every measured grid point, which approves that the measurement captured the energy containing range to a significant extent. Remarkable peaks were detected in the velocity spectra between 0.1 and 0.2 Hz in most grid point. This indicates that large parts of the measurement field are affected by processes of such low frequencies. It can, however, not be determined based on such statistical analyses, what flow structures produce these peaks, which will be justified in Chapter 6.

The instantaneous vector fields contain the velocity fluctuations of turbulent flow structures superimposed to the mean velocity field, which represents a considerable disturbance in the vector distribution, hence in detecting flow structures. Although the main stream is a dominant flow structure that can be roughly recognized visually, its instantaneous centerline could not be determined reliably in the instantaneous velocity fields, so that further characteristics of the main-stream oscillation, like characteristic frequencies or amplitude of the oscillation, cannot be determined based on the raw velocity data.

The analysis of the measurement duration has shown, on the one hand, that the measured mean and variance values converge over the measurement time in every grid point. On the other hand, the examination of the errors arising from the finite length measurement pointed out that the estimated error in the measured variances is significant in large parts of the measurement field. This means that the measurement duration of 5-minutes was not sufficient in large parts of the flow field for obtaining steady variance values.

POD is a method that is suitable to be applied on velocity datasets with inhomogeneous flow fields. It decomposes the input velocity dataset to orthogonal oscillation components defined as single vector fields, called POD modes, and corresponding coefficient time series. The contribution of an individual POD mode at a given time step is the product of the vector field of the POD mode and the value of the POD coefficient at the needed time step. The instantaneous velocity field at a time step can be reconstructed as the sum of the contributions of the individual POD modes at that time step.

The vortical structures that can be observed in the vector fields of the POD modes are by themselves not flow structures but just spatial patterns of the oscillation created by the individual POD modes. Flow structures evolve as the result of the combined contributions of several POD modes. Further, apparent structures in the velocity fields reconstructed using arbitrary combinations of POD modes are also not suitable to be regarded as flow structures without further evidence, because the exclusion of arbitrary POD modes from the reconstruction probably excludes only some portions of flow structures, so that the structures in the reconstructed data become distorted. For these reasons, it is generally a challenge to find the appropriate POD modes participating in the reconstruction of a particular flow structure of interest.

The POD modes expected to be relevant for describing flow structures or characteristic flow processes are usually low-order POD modes that are connected. Connection can be usually identified based on common characteristics, like identical energy contributions or identical dominant frequencies of the POD coefficients. Such a connection between POD modes was not clearly recognizable in the measured dataset. However, the main flow field, also called POD mode 0, could not be involved in such an examination, because it has no turbulent kinetic energy contribution or POD coefficients.

Since the movement pattern of the main-stream displacement shows an oscillating character, it is expected to be efficiently represented in the POD result. As a result of the structure of the auto-covariance matrix in Eq. (2.30) and the eigenvalue problem in Eq. (2.31) POD works grid point bounded. If a flow structure occurs at the same locations repeatedly, it introduces significant amount of turbulent kinetic energy at the same locations, so that it is probably represented by very few POD modes with large energy contributions. For this reason, POD can be efficiently used to identify flow structures that occur at the same locations repeatedly, especially large structures showing an oscillating pattern.

The velocity data reconstructed using POD modes 0-1 appeared to reproduce a dominant part of the oscillating main stream. The oscillating main stream is recognizable in the velocity field reconstructed using POD modes 0-1, even though it is not obviously recognizable in the vector field of the POD mode 1. In the sense of the oscillation components, however, it is dominantly represented by a single POD mode. It has to be further noted that the dominant reproduction of the oscillating main stream by POD modes 0-1 could only be confirmed by visual examination in this chapter.

The examination of the impact of the measurement duration on the POD results is computationally extensive, since POD has to be computed explicitly for each examined duration, hence dataset with given duration. For this reason, the examination was performed in this chapter using datasets of three different durations and revealed that low-order POD modes and POD coefficients converge already at shorter durations. Furthermore, the POD modes 1 and 2 and the corresponding POD coefficients yielded essentially the same result based on 3-minutes and on 5-minutes durations.

6 Detecting predictable flow events based on non-periodically repeating flow events

As described in Section 1.1 predictability of turbulence has been proposed in the literature as one of the features that essentially determine the influence of turbulence on fish swimming behavior. The feature of predictability is interpreted in this work as the existence of turbulent flow events in the flow whose occurrences are predictable. The fundamental assumption of the present approach is that repeating flow events are the basis for predictability, because repetition facilitates their recognition by experience on the fish' part. Leaning on this assumption, the following requirements for predictability (short-term predictability) have been formulated:

1. flow events occurring repeatedly in the flow exist,
2. repeating sequences of different flow events exist in the flow.

If these conditions are fulfilled, the flow events occurring later within the repeating sequence are considered predictable in the sense of short-term predictability, even if the sequence itself is repeating non-periodically.

It has to be reminded that the feature of predictability refers to the flow alone. Whether fish are able to recognize or use predictable flow events of given characteristics, has to be evaluated based on fish-behavior experiments by correlating fish behavior and the occurrences of predictable flow events. While fish-behavior experiments have already proven that fish can make use of the predictability of periodically occurring flow events (see Section 1.1), the predictability of non-periodically repeating flow events has not been evaluated yet, because such flow events could not be detected by the flow-analysis methods so far.

In this chapter a flow-analysis methodology is presented that is suitable for detecting non-periodically repeating predictable flow events and their occurrences. First, it is presented how repeating sequences of flow events can be identified based on POD. Then, it is demonstrated how a supplementary flow feature that is not represented by a POD mode can be involved in the examination. Finally, it is discussed how the predictable flow events determined using the method presented could be detected in full-scale facilities by means of point measurement techniques.

6.1 Identifying repeating flow events occurring sequentially based on POD

As described in Chapter 5, repeating flow events are expected to be well represented by POD modes, especially if they are of large scale and occur frequently at the same locations. In the present section repeating sequences of flow events are identified based on POD results.

First the main-stream oscillation is examined in detail based on POD mode 1, because it is the largest and most energetic flow structure with repeating character, which expectedly is the easiest that fish will recognized. Then, further POD modes are studied in order to find other repeating flow events that are in connection with the main-stream oscillation. Finally, the sequence of the occurrence of the connected flow events is determined.

6.1.1 Examining the oscillating main stream based on POD mode 1

As shown in the previous chapter, the oscillating main stream could be principally reproduced by POD modes 0-1, i.e. by the velocity fields reconstructed using POD modes 0 and 1 (Figure 5.26). However, the rough agreement of the main-stream locations in the raw and the reconstructed velocity fields was only asserted by visual comparison of the velocity fields at different time steps. Although Tarrade et al. (2011) also found that POD mode 1 roughly describes the main-stream oscillation (see Section 3.3), they did not present a comparison of the main-stream locations in the raw velocity fields and in the velocity fields reconstructed using POD modes 0-1.

The verification of the correctness of the main-stream locations reconstructed by POD modes 0-1 is difficult, because it requires the comparison of the main-stream locations in the raw and the reconstructed velocity fields. However, the accurate location of the main stream cannot be determined reliably in the raw velocity fields due to the disturbing presence of the instantaneous fluctuations of superimposed turbulent flow structures (Figure 6.1 a). In order to make the main stream in the raw velocity fields better identifiable, the fluctuations arising from small-scale flow structures were reduced in the present section using low-pass frequency filtering by considering that small-scale turbulent flow structures are not only of smaller size but statistically also of higher frequency. The low-pass frequency filtering was performed on the time series of each grid point; the frequency cutoff was selected as 0.7 Hz based on the velocity spectra in the grid points (e.g. Figure 5.4), which contained peaks between 0.1 and 0.2 Hz and showed the -5/3 slope starting at about 1-3 Hz.

The instantaneous velocity fields of the raw data, the low-pass frequency-filtered data and the data reconstructed using POD modes 0-1 can be compared visually at three different time steps in Figure 6.1. It can be seen that the fluctuations are significantly reduced in the low-pass filtered velocity fields (Figure 6.1 b) and that the main-stream locations show a good agreement between the low-pass frequency-filtered data and the data reconstructed using POD modes 0-1. Although this confirms that POD modes 0-1 reproduce the oscillating main stream to a large extent, the agreement is still qualitative.

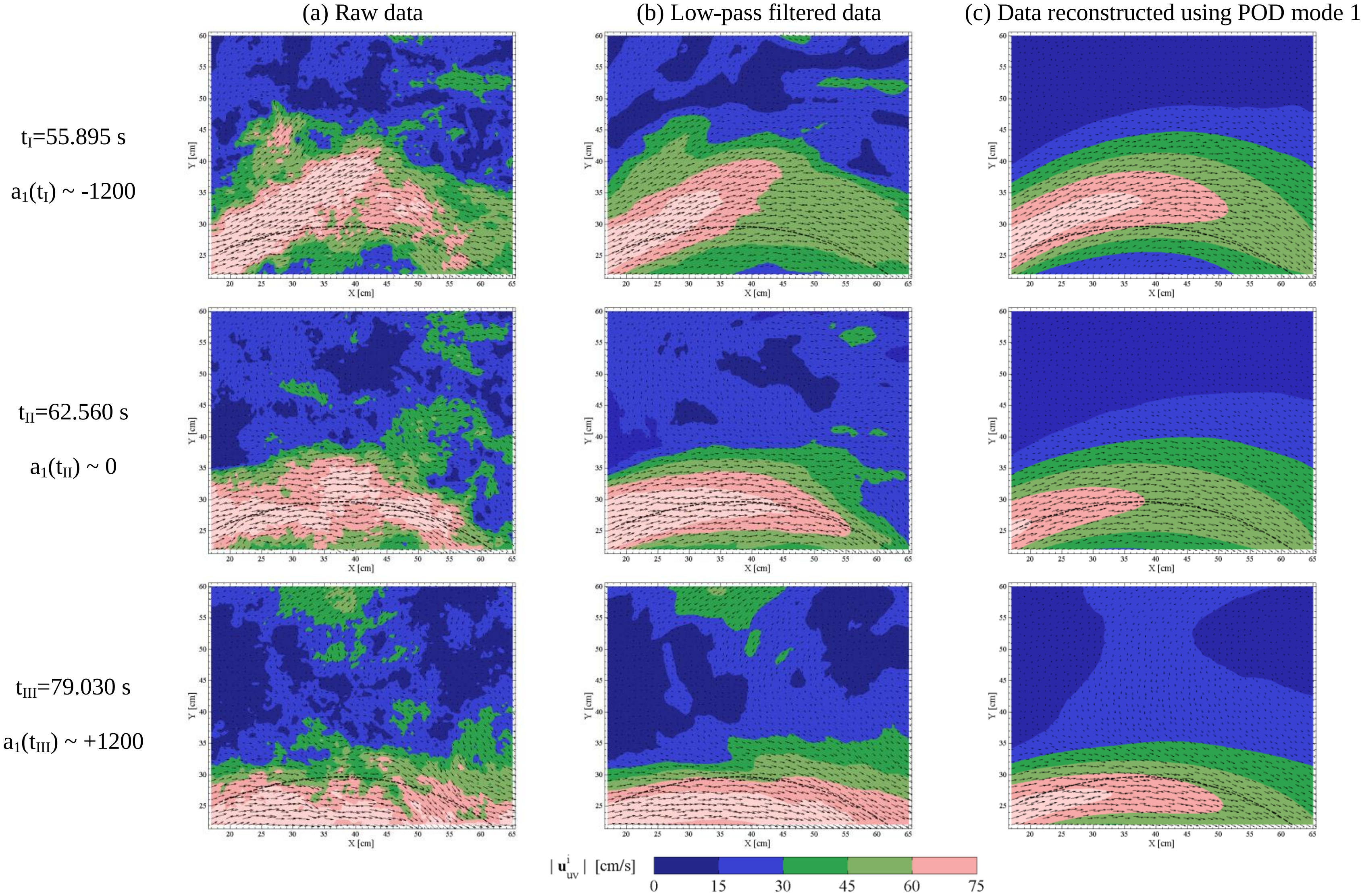

Figure 6.1 Instantaneous velocity fields of (a) raw velocity data (b) low-pass frequency-filtered velocity data (c) velocity data reconstructed using POD modes 0-1 at three different time steps. The dashed line represents the mean main-stream centerline.

As a first attempt to quantitatively compare the main-stream locations in the different velocity fields, the curves along the highest velocity magnitudes within the main-stream were generated. The curves resulting from the low-pass frequency-filtered velocity fields were, however, inconsistent by using both streamlines and polynomial curve-fitting as follows. Streamlines were directed out of the visually recognizable main-stream centerline due to portions of small-scale velocity fluctuations that persisted after the filtering. The polynomial curve-fitting to the locations with the highest velocity magnitudes were misled by large flow structures that produced high velocity magnitudes outside the main stream. Such flow structures persisted in the velocity fields after the frequency filtering, because they possessed similar fluctuation frequencies as the main-stream oscillation.

Finally, instead of generating curves, the *y*-positions of the grid points with the highest velocity magnitudes were used to approximately compare *main-stream centerline* locations as follows. The y-position of the grid point in the cross-section of x=35.00 cm with the highest velocity magnitudes has been ascertained at every time step for both the filtered and the reconstructed datasets (Figure 6.2). This cross-section was selected because the main-stream centerline position showed strong deviations from the mean main-stream centerline and, at the same time, the velocity difference between the main stream centerline and the rest of the flow was still significant (Figure 6.1 c).

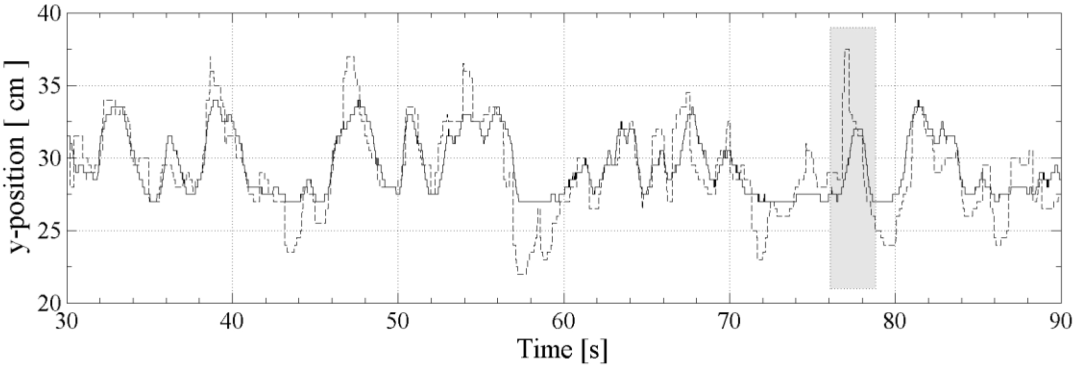

Figure 6.2 Approximated *y*-position of the main stream centerline at x=35.00 cm in the frequency-filtered (dashed line) and in the reconstructed (solid line) datasets. The grey rectangle marks the exemplary interval. The precision of the *y*-positions is 5.0 mm due to the grid resolution of the data.

Figure 6.2 represents the comparison of the main-stream centerline positions in the data reconstructed using POD modes 0-1 and in the frequency-filtered data. This confirms that they coincide to a large extent, but also reveals significant deviations at several short intervals. Such an exemplary interval marked by the grey rectangle is examined next in detail.

The sequence of the raw and of the reconstructed velocity fields corresponding to the exemplary interval (Figure 6.2) is displayed in Figures 6.3 and 6.4. Three characteristic sections can be distinguished in the sequence of the raw velocity fields (Figures 6.3 b and 6.4 b). First a large flow structure enters to the measurement field from the upstream side (t_{III}-t_{IV}); then the flow structure travels on the left-hand side of the main stream, thereby pulling the main stream from its original position and becoming less and less distinguishable from the main stream (t_V-t_{VII}); and finally the flow structure is undistinguishable from the main stream and the main stream returns to its original position (t_{VII}-t_X).

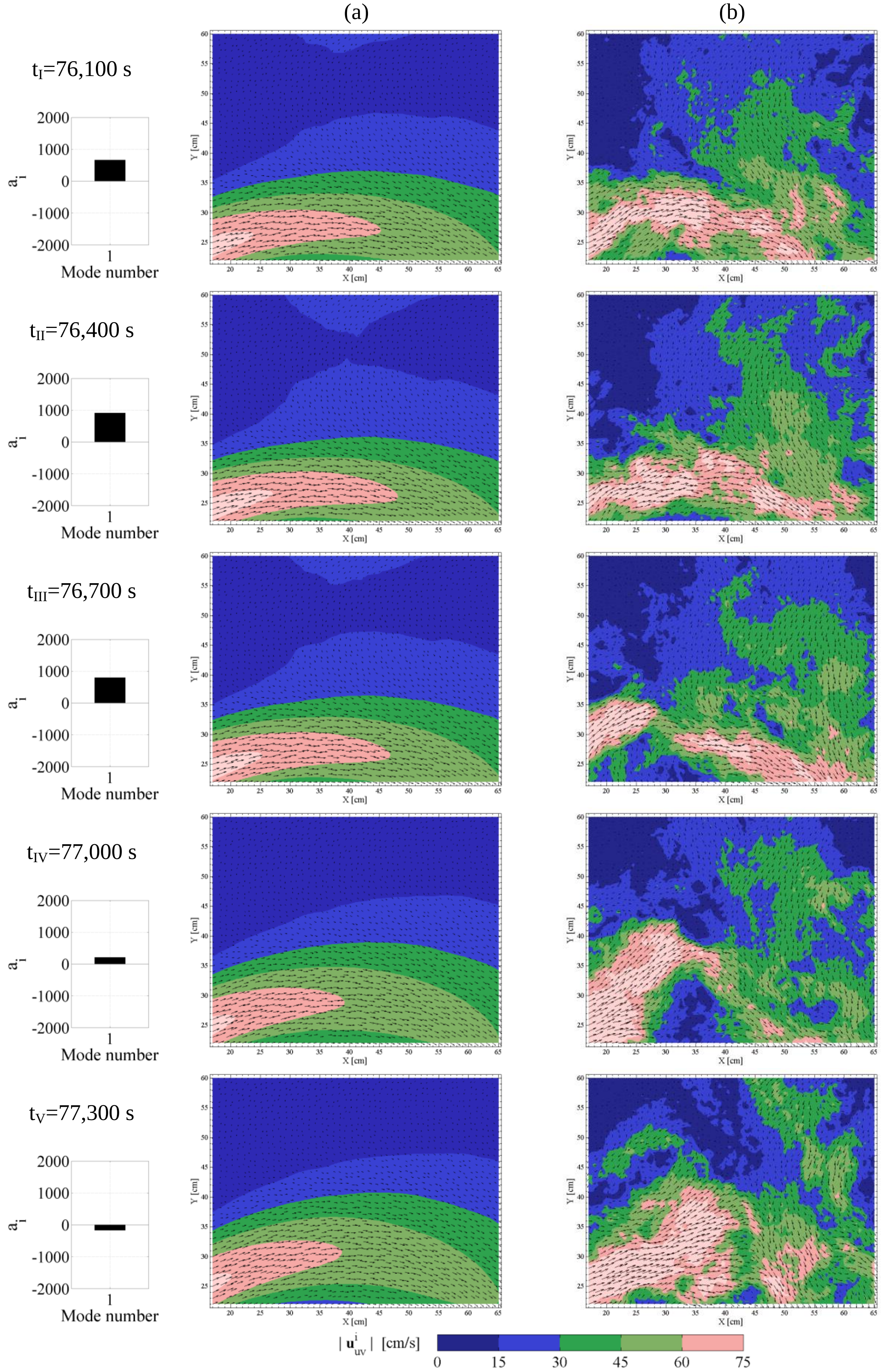

Figure 6.3 Sequence of velocity fields between t=76.1-77.3 s in (a) the dataset reconstructed using POD mode 0-1 (b) the raw dataset. The bar graphs show the values of the POD coefficient of mode 1

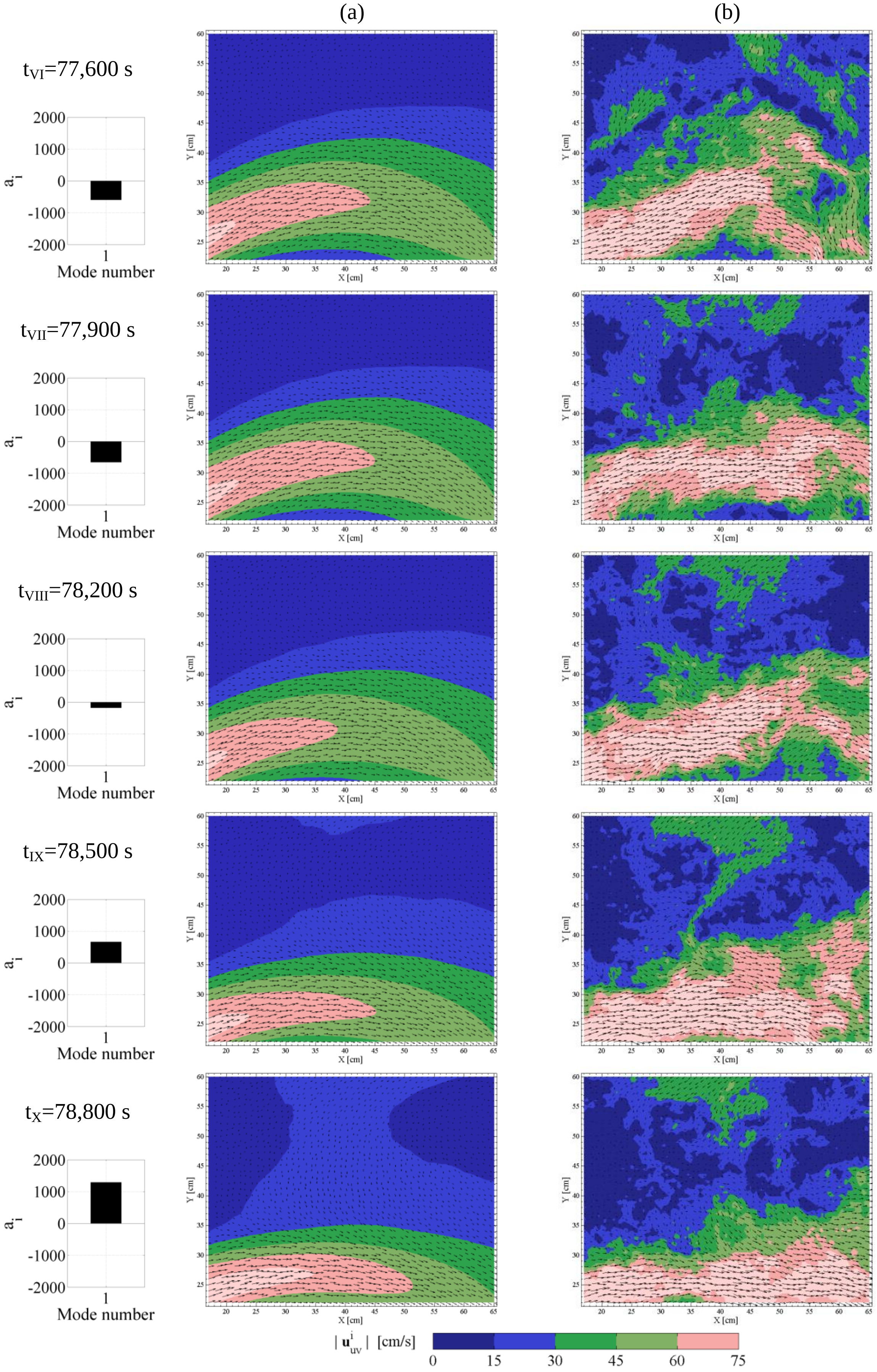

Figure 6.4 Sequence of velocity fields between t=77.6-78.8 s in (a) the dataset reconstructed using POD mode 0-1 (b) the raw dataset. The bar graphs show the values of the POD coefficient of mode 1.

It is notable in the velocity fields reconstructed using POD modes 0-1 (Figures 6.3 a and 6.4 a) that, while only a marginal displacement of the main stream occurs at the beginning of the process (t_I–t_{IV}), the displacement becomes more and more significant as the flow structure pulls the main stream and becomes less and less distinguishable from the main stream (t_V–t_{VII}), which corresponds with the visual observations in the raw velocity fields. This explains the differences in the *y*-positions in Figure 6.2, which arise from the different contents of the two datasets. While the dataset reconstructed using POD modes 0-1 just contains a main stream with a consistent centerline (Figures 6.3 a and 6.4 a), the low-pass frequency-filtered data additionally contains flow structures that sometimes produce high velocities outside the main stream, which results in deviations in the *y*-positions. Further, the example also highlights that, while POD mode 1 itself is not used for reproducing the large flow structure, it reproduces the main-stream displacement caused by the flow structure traveling along the main stream. This justifies that the data reconstructed using POD modes 0-1 can be considered as the dominant component of the oscillating main stream.

It is interesting that the energy contribution of POD mode 1 to the ensemble turbulent kinetic energy is 18.7 %, which is not uniformly distributed over the measurement field but rather concentrated on the sides of the mean main stream. Figure 6.5 (a) shows the ratio of the turbulent kinetic energy produced by POD mode 1 to the total turbulent kinetic energy over the measurement field. This reveals that the turbulent kinetic energy introduced by POD mode 1 is the highest on the left-hand side of the mean main stream (represented by P_C) and its contribution locally exceeds 50% of the local total turbulent kinetic energy level (Figure 6.5 a).

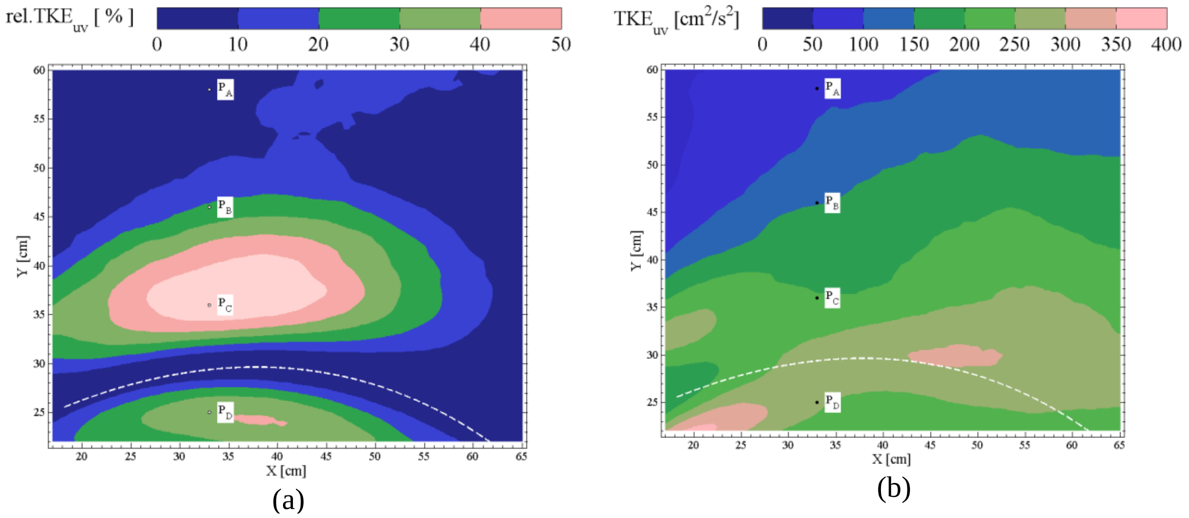

(a)

(b)

Figure 6.5 (a) Distribution of the local TKE contributions of POD mode 1 and (b) turbulent kinetic energy field of the dataset reconstructed excluding POD mode 1.

Figure 6.5 (b) shows the turbulent kinetic energy field of the dataset reconstructed excluding POD mode 1, i.e. the dataset reconstructed using POD modes from 2 to 14938. This figure confirms that the high turbulent kinetic energy levels in the two zones on the sides of the mean main stream shown in Figure 5.2 are produced by the main-stream oscillation represented by POD mode 1.

The contribution of POD mode 1 to the ensemble turbulent kinetic energy can also be observed by comparing velocity spectra of the raw dataset and the dataset reconstructed excluding POD mode 1. In the velocity spectra it can be recognized that the energy contributions are significantly changed at low frequencies in positions near the mean main stream, for example in position P_C (Figure 6.6).

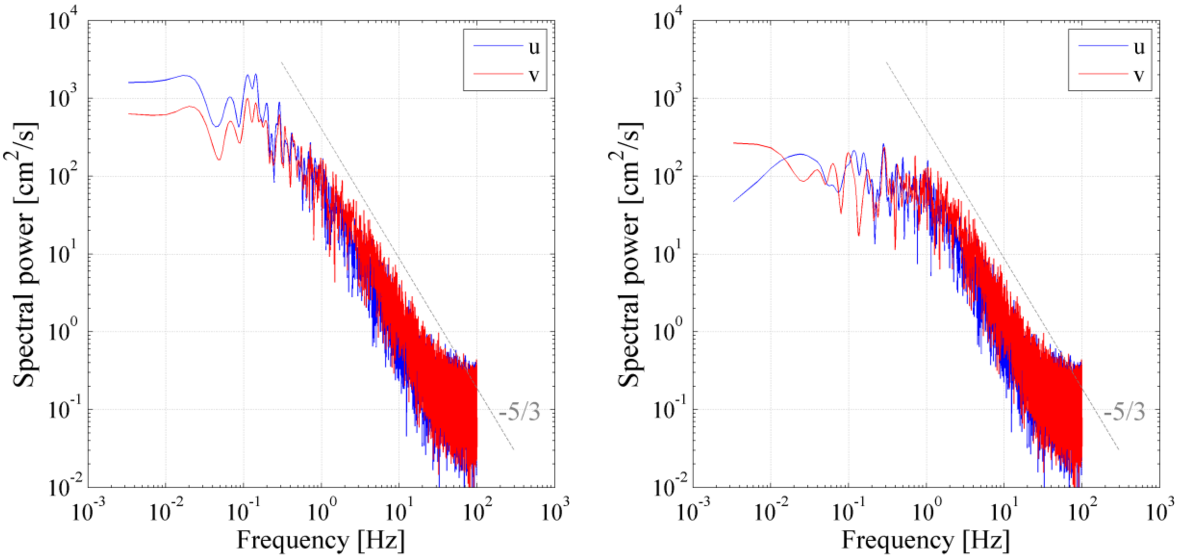

(a) (b)

Figure 6.6 Velocity spectra in position P_C in (a) the raw dataset and (b) the dataset reconstructed excluding POD mode 1.

6.1.2 Identifying repeating flow events connected with POD mode 1

In this section, further POD modes of high energy contributions are examined in detail in order to find other repeating flow events that are in connection with POD mode 1, i.e. the main-stream oscillation. The following investigation focuses on POD modes of high energy contributions, because they proved to be deterministic in representing processes of the flow in the previous chapter (see Section 5.3.3). Though, since it is not possible to display details of each POD mode in the printed work, only the characteristics of the POD modes 1 to 6 are presented exemplary in this section.

Figures 6.7 and 6.8 show the vector fields of the individual POD modes (columns a) and reveal their impact on the flow (columns b and c). The impact of an examined POD mode is demonstrated through the velocity fields reconstructed using POD mode 0 and the examined POD mode at both a large positive (Figures 6.7 b and 6.8 b) and a large negative POD coefficient (Figures 6.7 c and 6.8 c). The coefficients have been selected because they are typical large values for the examined POD mode (see Figure 5.18 a for POD mode 1), so that the corresponding reconstructed velocity fields can be regarded as instantaneous velocity fields. It can be observed in the reconstructed velocity fields that different modes produce different oscillations of the trajectory along the highest velocities. While the direction of the main-stream displacement caused by the oscillation of POD mode 1 is identical along the whole length, POD modes of higher order often represent oscillations yielding displacements in alternating directions at different wavelengths and positions. The impacts of the individual POD modes on the flow, however, do not reveal a connection between them.

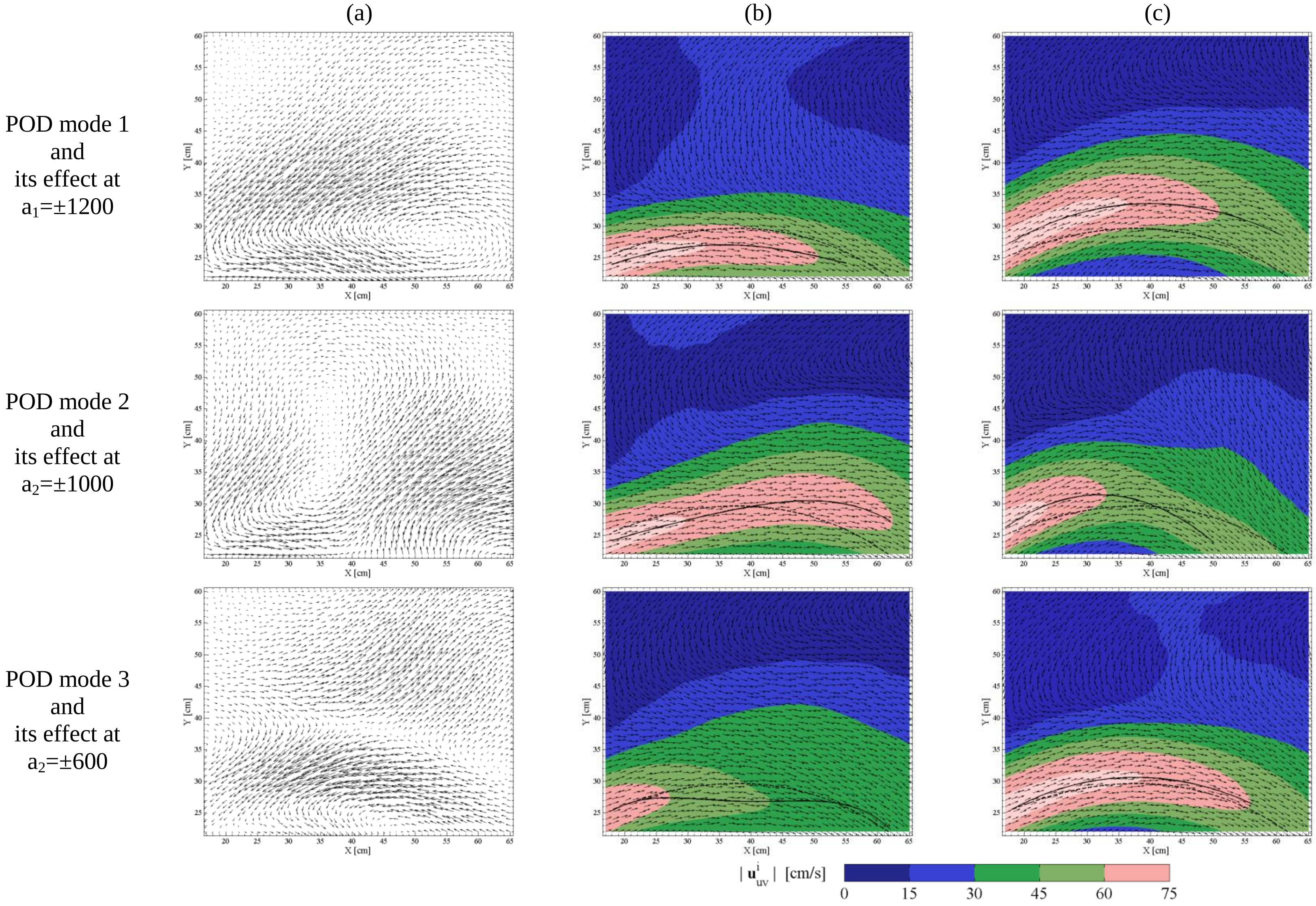

Figure 6.7 (a) The POD mode; (b-c) the velocity fields reconstructed using POD mode 0 and the examined POD mode at a large positive and negative coefficients, respectively. The solid line shows the trajectory of the highest velocities in the reconstructed fields; the dashed line is the mean main-stream centerline.

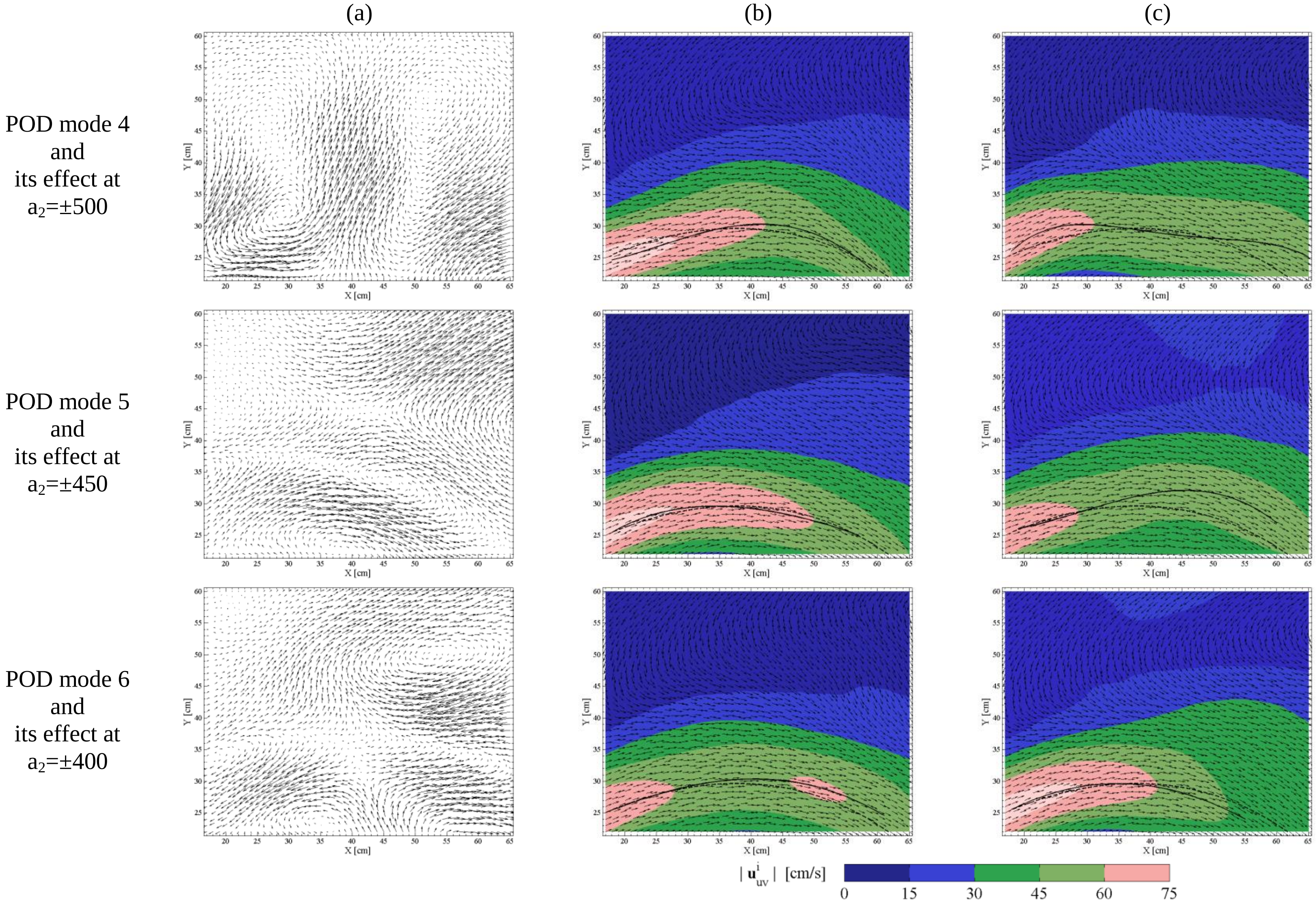

Figure 6.8 (a) The POD mode; (b-c) the velocity fields reconstructed using POD mode 0 and the examined POD mode at a large positive and negative coefficients, respectively. The solid line shows the trajectory of the highest velocities in the reconstructed fields; the dashed line is the mean main-stream centerline.

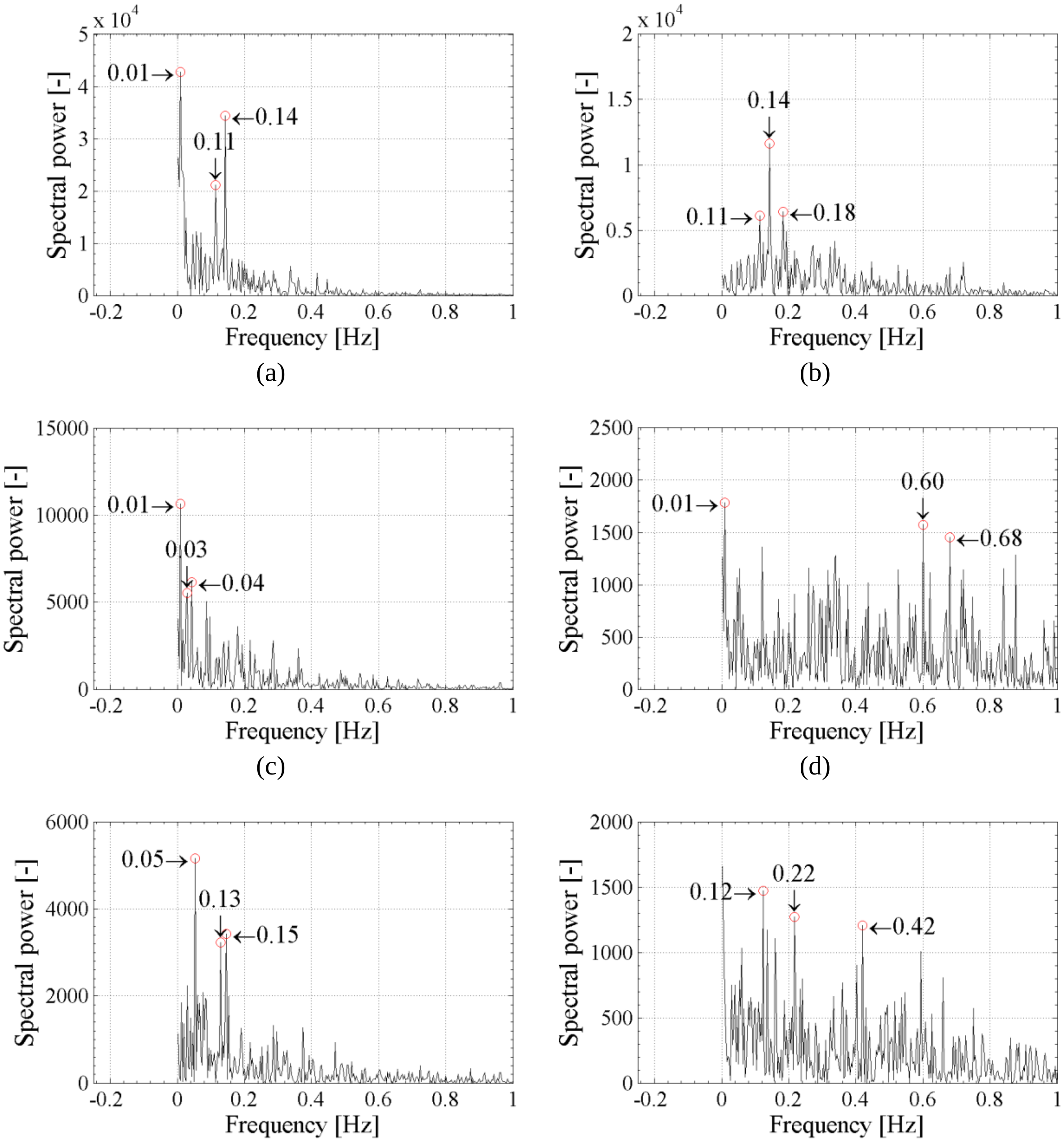

(a) (b)

(c) (d)

(e) (f)

Figure 6.9 Frequency spectra of the POD coefficients of (a) POD mode 1, (b) POD mode 2, (c) POD mode 3, (d) POD mode 4, (e) POD mode 5, (f) POD mode 6. The frequencies of the three highest energy contributions are marked.

Figure 6.9 shows the frequency spectra of the POD coefficient time series of modes 1-6 highlighting the characteristic frequencies of the three highest power contributions. Although the characteristic frequencies of none of the examined POD modes are identic, POD modes 1 and 2 show a common characteristic frequency, which suggests to examine the impact of POD mode 2 explicitly.

In order to visualize the role of POD mode 2, the raw velocity fields have been compared with velocity fields reconstructed using POD modes from 0 to 2, denoted here as POD modes 0-2. Figures 6.10 and 6.11 contain the raw and the reconstructed velocity fields of the same exemplary interval that was studied in the previous section, which allows the comparison of these results with the sequence of velocity fields reconstructed using POD modes 0-1.

Figures 6.10 and 6.11 reveal that POD mode 2 plays a significant role in reconstructing the large flow structure entering the measurement field at t_{III}. It can be seen in Figures 6.10 and 6.11 that the reconstructed flow field is modified by POD mode 2 at different time steps depending on the flow structure position. At the time steps where the flow structure is entering the measurement field (t_{III}-t_V) high flow velocities are produced in the upstream part of the flow field on the left-hand side of the main stream, which is achieved by negative POD coefficients of POD mode 2. At time steps where the flow structure travels along the main stream (t_{VII}-t_{IX}) high flow velocities are produced in the downstream part of the flow field on the left-hand side of the main stream, which is achieved by positive POD coefficients of POD mode 2.

This sequence reveals how POD modes can be used to reconstruct individual time steps; the flow velocities are increased at the needed positions by combining POD modes 1 and 2 at appropriate values of the coefficients a_1 and a_2.

Essential for the reconstruction of the individual time steps is the combination of POD modes at appropriate values of the coefficients. Figure 6.12 gives an overview of meaningful velocity fields that can be generated using POD modes 0-2 by combining large positive, zero and large negative values of the coefficients a_1 and a_2. Note that the values of the coefficients have been selected based on typical large values for the examined POD modes. It can be recognized that the process observed in the exemplary sequence (Figures 6.10 and 6.11) can be roughly described by the velocity fields in Figure 6.12 starting from the velocity field at (a_1>0, a_2=0), followed by (a_1>0, a_2<0), and then continued with the remaining velocity fields in anti-clockwise direction. The velocity field at (a_1=0, a_2=0) has not been used in the exemplary sequence. Notable in this representation is that some of the velocity fields in Figure 6.12, like (a_1>0, a_2<0) or (a_1<0, a_2>0), do not show up when examining the POD modes separately, like in Figures 6.7 and 6.8.

Although the connection between POD modes 1 and 2 has been discovered based on a common characteristic frequency in the frequency spectra of the corresponding POD coefficients, a further efficient method for revealing connections between POD modes representing subsequent flow events is shown and explained in next section.

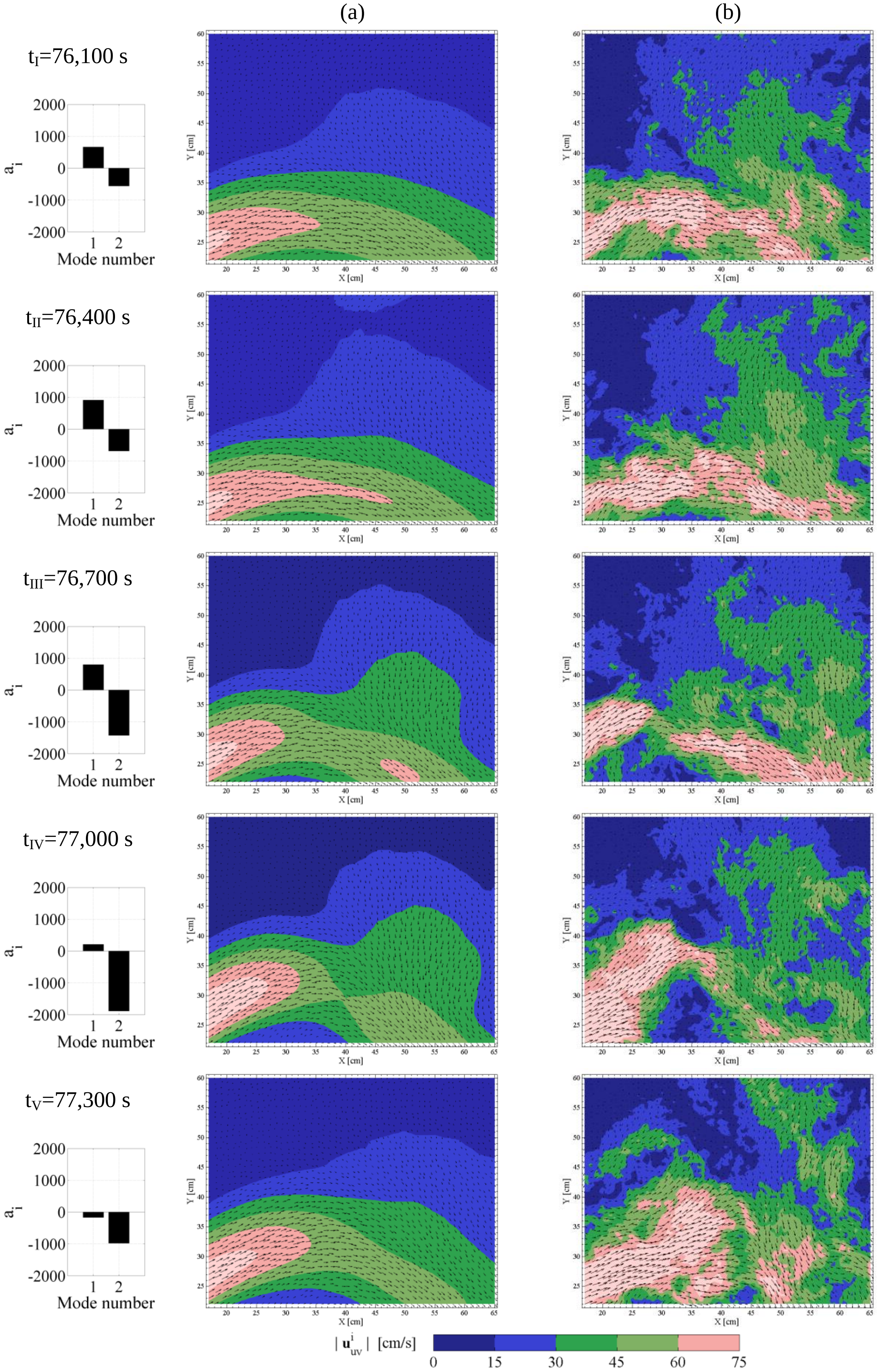

Figure 6.10 Sequence of velocity fields between t=76.1-77.3 s in (a) the dataset reconstructed using POD modes 0-2 (b) the raw dataset. The bar graphs show the values of the POD coefficients.

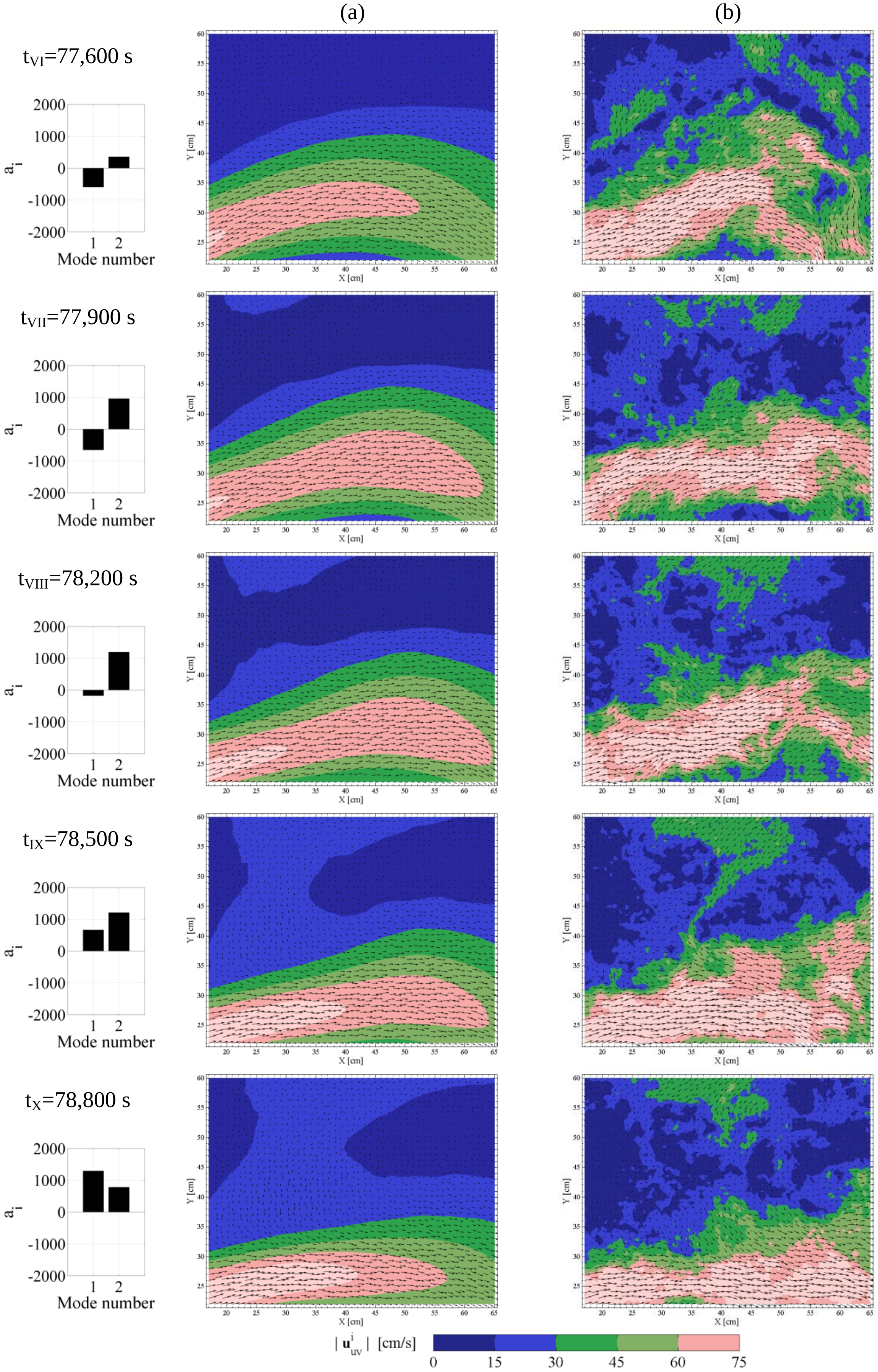

Figure 6.11 Sequence of velocity fields between t=77.6-78.8 s in (a) the dataset reconstructed using POD modes 0-2 (b) the raw dataset. The bar graphs show the values of the POD coefficients.

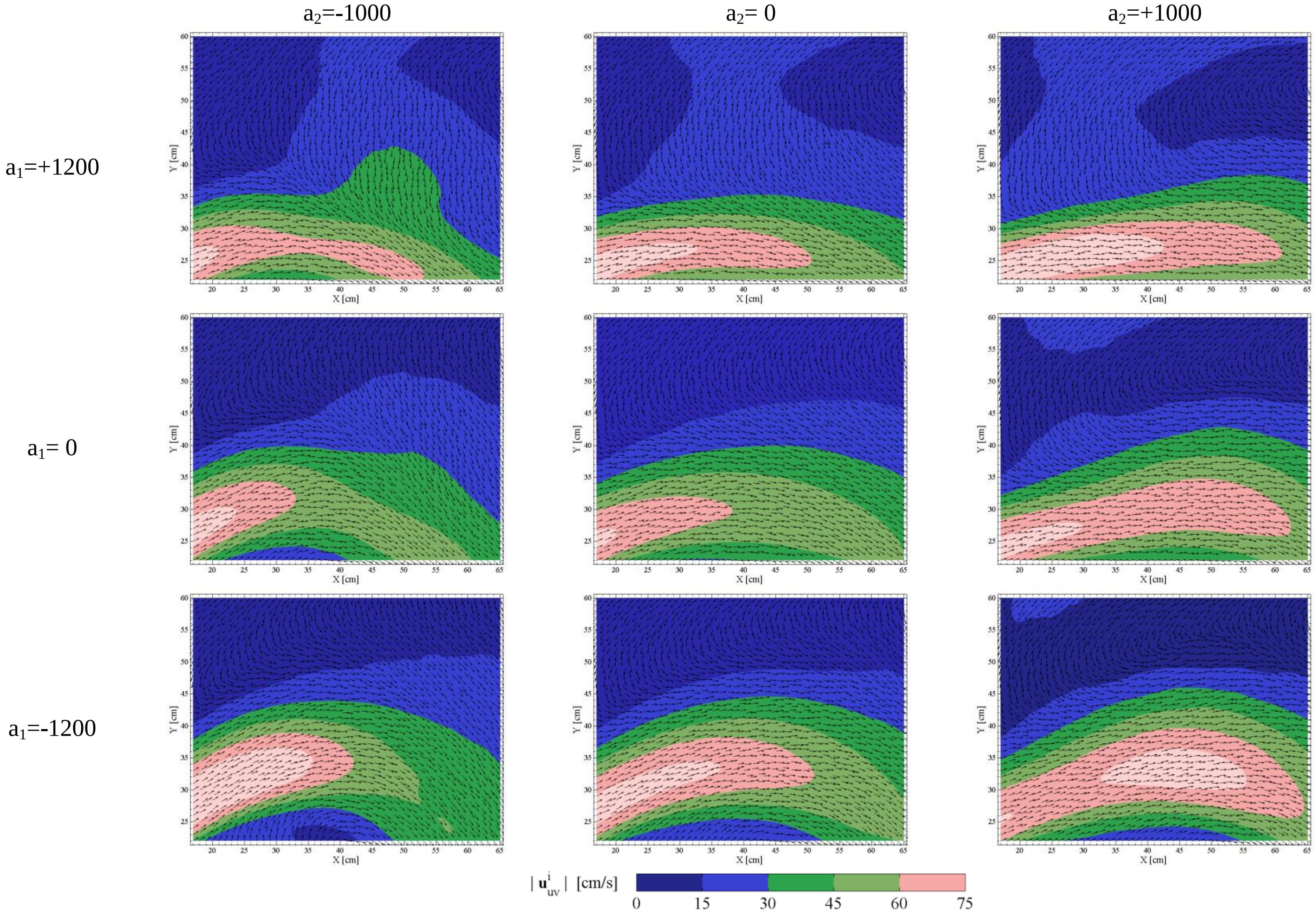

Figure 6.12 Possible velocity fields using POD modes 0-2 by meaningful combinations of the POD coefficients a_1 and a_2.

6.1.3 Determining the sequential occurrence of flow events represented by POD modes

In terms of flow events the exemplary sequence presented before (Figures 6.10 and 6.11), which is regarded as a *sample sequence* in the following, can be illustrated using Figure 6.13:

1. a transversal current from the left-hand side of the main stream pushes the main stream to the right,
2. a flow structure entering the measurement field from upstream does not follow the new main-stream trajectory but leaves the main stream to the left-hand side of the main stream,
3. the flow structure travels along the left side of main stream, thereby pulling the main stream to the left-hand side and becoming less and less distinguishable from the main stream,
4. the flow structure leaves the measurement field, while the main stream returns to its original position.

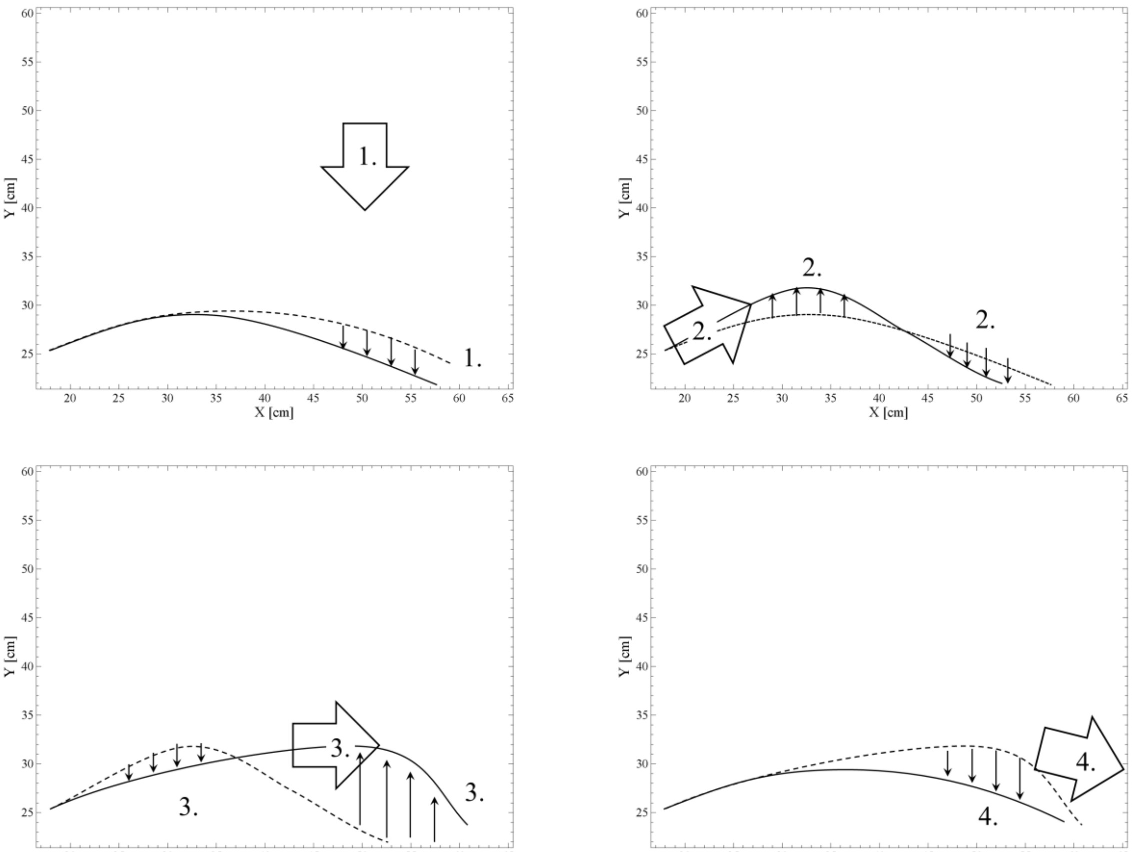

Figure 6.13 The flow events of the sample sequence represented by POD modes 0-2. The dashed line represents the position of the main stream in the previous frame; the solid line represents the new position of the main stream; the block arrow represents further flow events relevant for the process

In terms of POD the sample sequence of flow events shown in Figure 6.13 can be substantially represented by the simplified temporal evolution of the coefficients a_1 and a_2 as shown in Figure 6.14. The sequence consists of a characteristic process: (I) a_2 becomes negative at some point in time where

a_1 is positive, and a_1 starts to decrease; (II) a_2 reaches negative maximum and somewhat later a_1 too; (III) a_2 becomes positive while a_1 is negative; (IV) a_1 gets positive, then a_2 reaches a positive maximum and becomes finally zero.

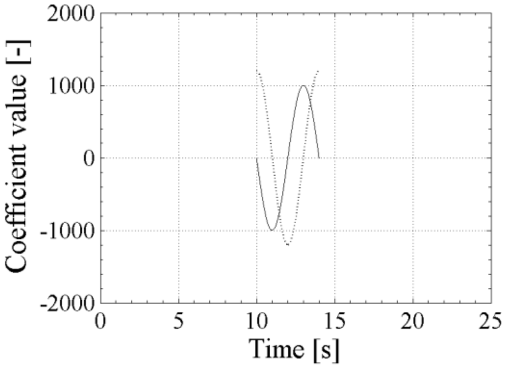

Figure 6.14 The sample sequence described using POD coefficients a_1 (dashed line) and a_2 (solid line).

The detailed examination of the time series of coefficients a_1 and a_2 resulting from the measurement (Figure 6.15) reveals that the sample sequence (described by Figures 6.13 and 6.14) occurs repeatedly in the measured dataset. Although every occurrence is somewhat different, the sample sequence can be clearly recognized in the intervals marked by dark grey rectangles and less similar occurrences of the sample sequence can be recognized in the intervals marked by light grey rectangles. These occurrences are typically initiating by a_2 turning to negative followed by a significant decrease of a_1. This demonstrates that the sample sequence is occurring repeatedly in the majority of time, so that it appears to be the fundamental process of the measured flow.

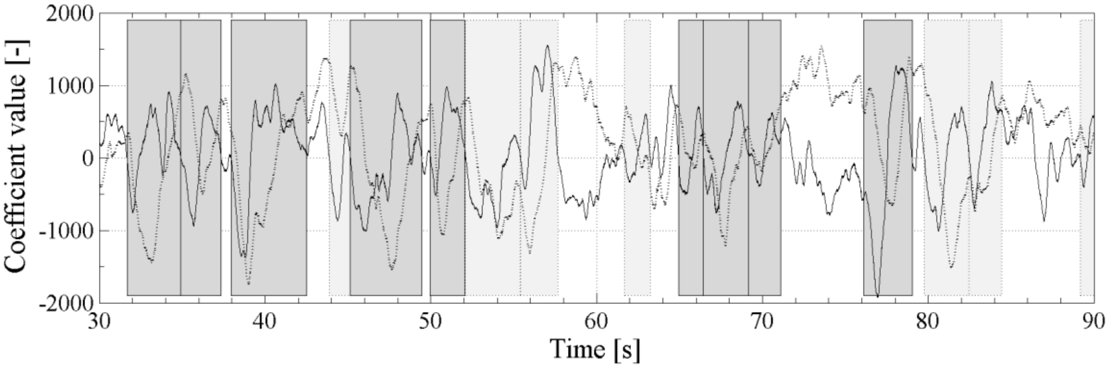

Figure 6.15 Time series of POD coefficients a_1 (dashed line) and a_2 (solid line) resulting from the measured dataset. The dark grey rectangles show more obvious and the light grey rectangles show less obvious occurrences of the sample sequence.

Tarrade et al. (2011) have not identified these processes using the temporal sequences of the POD coefficients, but their description based on visual observation of the instantaneous velocity fields is very similar to the one in this work. They explained the observed process as a combined result of velocity bursts arriving from the upstream pool and fluid exchange between the recirculation regions and the main stream. Further, they also found POD modes 1 and 2 to be connected, but contrary to present results they identified the connection based on the similar energy contributions of these POD modes.

The sample sequence described above practically confirms the existence of repeating sequences of flow events as required by the second condition of predictability described at the beginning of this chapter. Although the sample sequence never occurs identically, the different occurrences are essentially the same. Crucial for the present examination is that there is a sequential occurrence of flow events, i.e. the flow events represented by POD mode 2 precede the events represented by POD mode 1, namely that a_1 starts to increase after the negative peak of a_2, and the positive peak of a_1 occurs after the positive peak of a_2.

A usual method to find a time lag between time series is the cross-correlation function. The cross-correlation function of the coefficients a_1 and a_2 of present data shows a significant positive peak at a time lag of t=1.185 s and a similarly large negative time lag at t=-0.620 s (Figure 6.16). Considering the sample sequence in Figure 6.14 one can recognize that the positive peak denotes accordance with matching signs and the negative peak accordance with opposite signs. Although the correlation factor of about 0.4 seems to be low, it is significant compared to the standard deviation of the cross-correlation function. Besides, the relatively low peak correlation factor is to a large extent due to the fact that a_1 and a_2 denote different processes (a_1 represent the main-stream oscillation and a_2 represents flow further flow events), which leads to different time-series characteristics. Note that the absence of further large peaks in the normalized correlation can be seen as an evidence of aperiodicity.

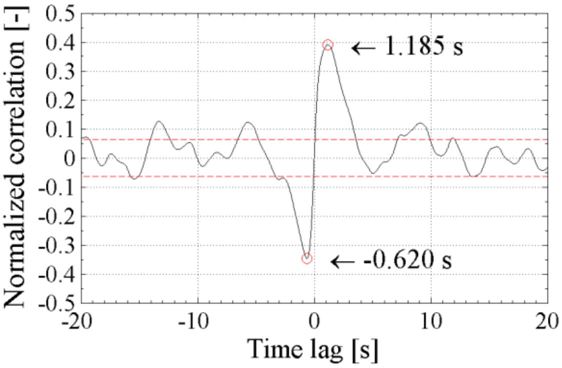

Figure 6.16 Cross-correlation function of the POD-coefficient time-series a_1 and a_2. The dashed lines denote the standard deviation of the function.

Since the time lags between flow events within the repeating sequence show variability (Figure 6.15), the time lag resulting from the cross-correlation function (Figure 6.16) is just a statistical time lag and should be handled with caution. Note that the individual time lags might be required to be measured synchronously to the fish-behavior experiments in the future, in order to correctly evaluate the correlation between fish-behavior and the occurrences of flow events during the experiments.

It has to be highlighted that the cross-correlation functions of POD coefficients (e.g. Figure 6.16) appear to be an efficient tool to identify connections between POD modes as aimed in Section 6.1.2.

These results confirm that the first and the second conditions of predictability are fulfilled by the present measurements. Subsequently occurring repeating flow events, i.e. repeating sequences of flow events, exist in the flow.

6.2 On identifying a connection between supplementary flow features and repeating flow events represented by POD modes

In the previous section it has been presented how repeating sequences of flow events can be detected in the measurement field based on POD. By using POD, however, only flow events are detected that occur inside the measurement field and that are represented by POD modes. If a *supplementary flow feature* not represented by a POD mode is considered to be relevant for predictability, it has to be involved supplementary into the examination. The supplementary flow feature can be relevant for fish behavior, if its change describes a *flow situation* that is advantageous or disadvantageous for fish. Such *supplementary flow feature* could be in case of the present measurement, for example, the flow velocity in the upstream slot (because it is not covered by the PIV measurement field, hence POD modes) or the curl of the velocity at any location (because single POD modes are not suitable to represent the curl as demonstrated in Section 5.3.2). The flow velocity in the slot would be relevant for fish behavior, since its temporal change describes an advantageous or disadvantageous *flow situation* depending on whether flow velocities in the slot are temporally low or high.

Since it can be expected that predictability is valuable for fish only if some advantageous or disadvantageous flow situation becomes predictable based on the repeating sequences of flow events, a connection is needed between the occurrences of advantageous or disadvantageous flow situation and the repeating sequence of flow events. In this section it is demonstrated how a connection can be identified between the occurrences of repeating flow events discussed in previous sections and the occurrences of advantageous or disadvantageous flow situations represented by the temporal change of the supplementary flow feature. Since both can be expected to occur non-periodically, a connection searched for based on the time series that represent their occurrences.

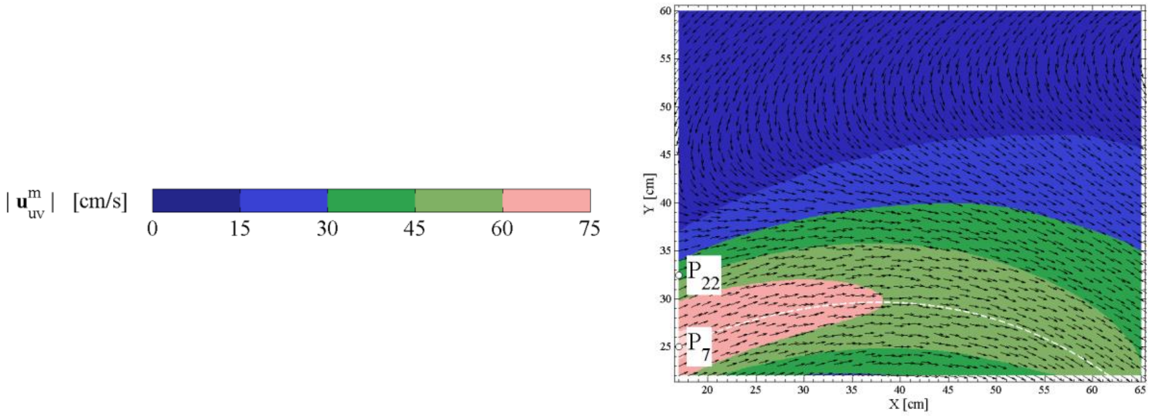

Figure 6.17 The mean velocity field with the locations of the used supplementary flow feature

It has to be highlighted that at the present stage of the work only a hypothetically advantageous flow situation has been used for several reasons. On the one hand, findings of fish-behavior experiments addressing flow situation with unsteady character are very limited. On the other hand, regions of the pool near the slot that are expected to be relevant for fish behavior were neither included in the measurement field of the present study, nor measured synchronously by a supplementary system.

However, although this demonstration is done based on a supplementary flow feature describing just a hypothetical advantageous flow situation, the following scheme can be adapted to other flow features based on future findings on fish-behavior.

The following demonstration uses the time series of the *u* velocity component in two different grid points at the upstream edge of the measurement field (Figure 6.17) as supplementary flow features. The hypothetical advantageous flow situation is represented by low flow velocities in points P_7 and P_{22}, as this enable fish to approach to slot using less energy while swimming upstream. Note that low flow velocities are represented by negative values of the velocity fluctuations in this example.

A usual method to reveal the relationship between different time series is scatter plot. Scatter plots of velocity time series of highly turbulent flows, however, usually show high variance, which prohibits the clear recognition of a relationship (Figure 6.18). The variance can be reduced by applying low-pass frequency filters to the velocity time series. When selecting the cutoff frequency of the filter it should be taken into consideration that the characteristic frequencies relevant for the studied connection remain preserved after the filtering (Figure 6.19).

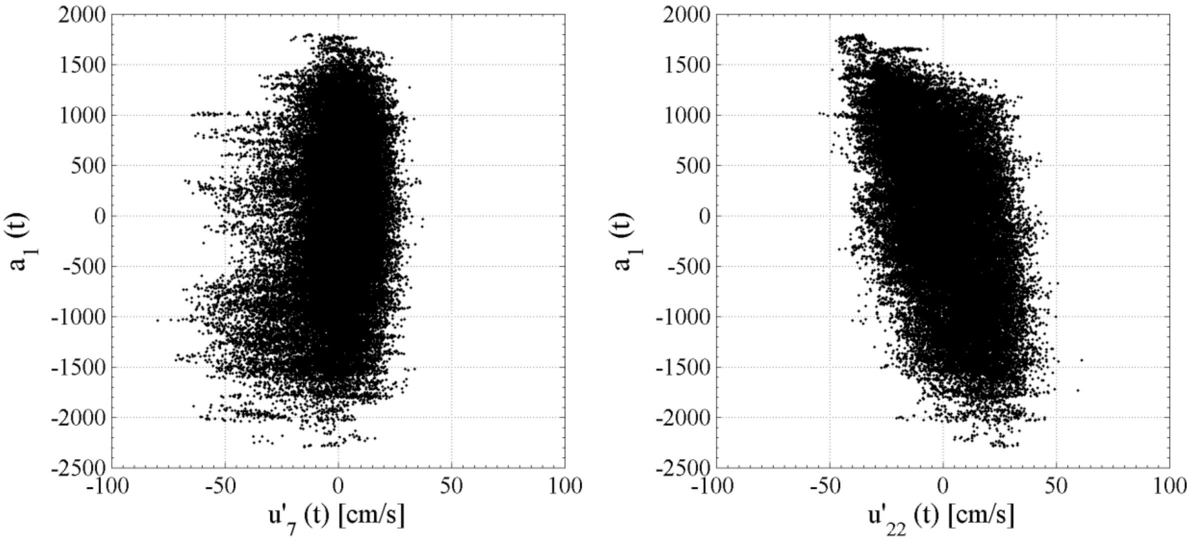

(a) (b)

Figure 6.18 Correlation scatter plots of the time series of POD coefficient a_1 and of the u velocity component in (a) P_7 and (b) P_{22}

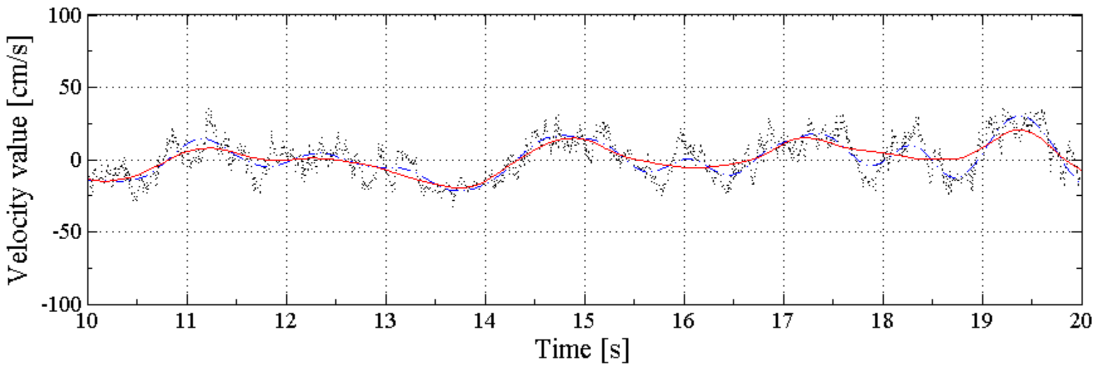

Figure 6.19 Low-pass frequency filtering of the u time series in P_{22} using different frequency cutoffs: raw data (dotted line), frequency cutoff of 1 Hz (dashed-dot-line) and 0.5 Hz (solid line)

Figure 6.20 shows the scatter plots based on the low-pass filtered velocity fluctuation time series using a frequency cutoff of 0.5 Hz. While the u' velocity appears to be almost not influenced from POD mode 1 in P_7 (Figure 6.20 a), it depends on the coefficient a_1 in P_{22} as follows (Figure 6.20 b). The connection between POD mode 1 and the u' velocity in P_{22} can be formulated as follows: at higher values of the coefficient a_1 the values of the u' velocity tend on average to become lower. If low u' velocities in P_{22} are considered advantageous for fish, such a flow condition would be given with higher probability in periods when the coefficient a_1 has high values, i.e. the main stream is located at low *y*-positions, hence more on the right-hand side in main flow direction (see also Section 6.1.1).

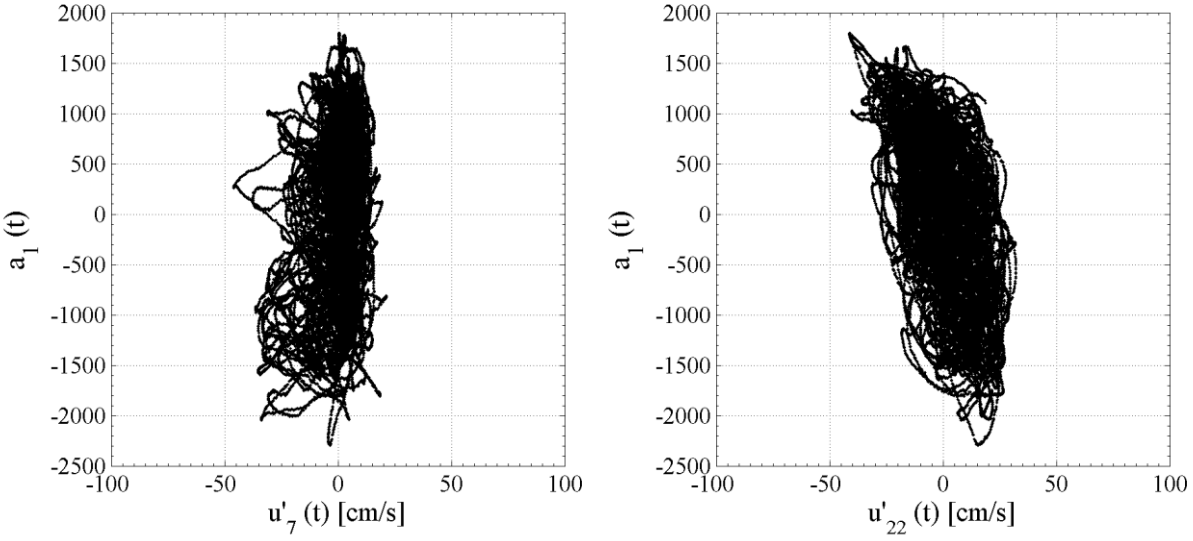

(a) (b)

Figure 6.20 Correlation scatter plots of POD coefficient a_1 and of the low-pass filtered u' velocity component in (a) P_7 and (b) P_{22}

It has to be noted that, since the velocity time series in P_7 and P_{22} used in this example were part of the input dataset for POD, this connection is already largely included in POD mode 1.

6.3 On detecting repeating flow events by means of point measurement techniques

Essential for the applicability of the presented methodology for evaluating fish behavior is that the occurrences of the predictable flow events have to be correlated with the behavior of fish. This requires measurements that are performed simultaneously with the fish-behavior observations, because predictable flow events can occur non-periodically. However, due to technical limitations and special requirements of the PIV technique (e.g. limited camera resolutions, no objects in the flow obstructing the illumination) it is hardly possible to perform PIV measurements during fish-behavior experiments in full-scale facilities. Since the only critical requirement of the presented methodology is that the flow has to be measured simultaneously in the whole flow field, the measurement is, in principle, also possible using simultaneous point measurements. In the present section it is demonstrated that the occurrences of the predictable flow events can be detected by means of point measurements, provided that the POD modes relevant for the predictability have been determined first using PIV.

For this demonstration the results presented in previous sections are compared with results obtained from a very-low-resolution dataset that is generated by keeping every 8th time step and every 16th grid point of the originally available velocity dataset. This yields a sampling frequency of 25 Hz and a spatial resolution of 80x80 mm providing 35 grid points.

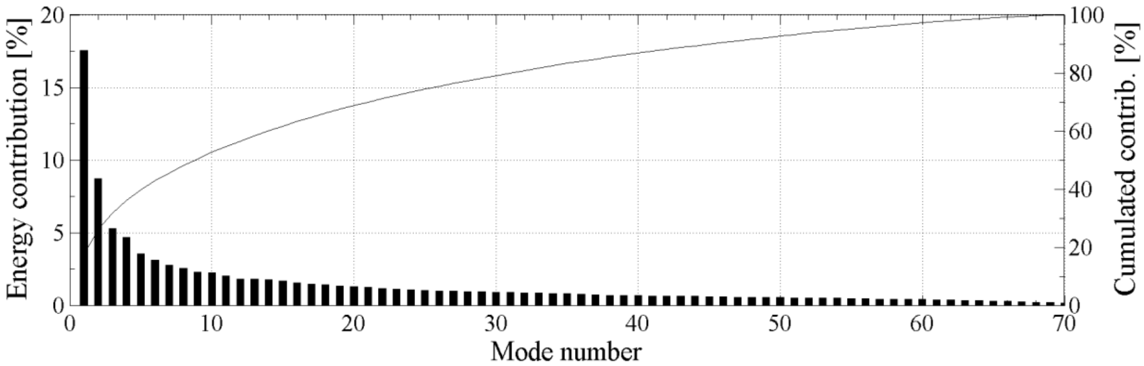

Figure 6.21 Contributions and cumulated contributions of the 70 POD modes of the low-resolution dataset to the ensemble turbulent kinetic energy

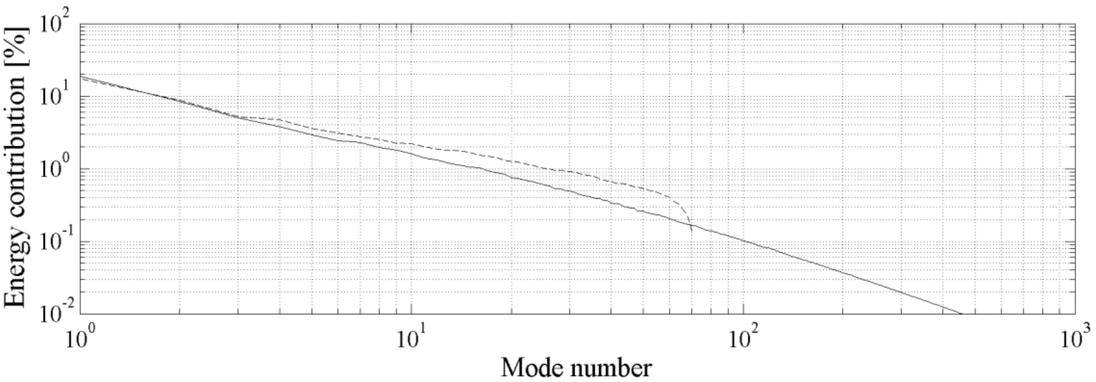

Figure 6.22 Distributions of the ensemble turbulent kinetic energies among the POD modes of the low-resolution dataset (dashed line) and the original dataset (solid line)

The POD of the low-resolution dataset resulted in 70 POD modes. Their contributions to the ensemble turbulent kinetic energy are displayed in Figure 6.21. The comparison of the contributions resulting from the two datasets is displayed in Figure 6.22. This reveals that only POD modes 1-3 have nearly the same percentual energy contributions in the two datasets; the remaining POD modes have larger contributions in the low-resolution dataset than in the original dataset.

The direct comparison of POD modes and POD coefficients resulting from datasets of different resolutions is not meaningful, because POD modes are normalized as represented by Eq. (3.1). Therefore, the magnitudes of the vectors in the POD modes using a lower grid resolution become generally larger. This can be observed well in Figure 6.23, where the vector fields of the POD modes 1 resulting from the original and the low-resolution datasets can be compared.

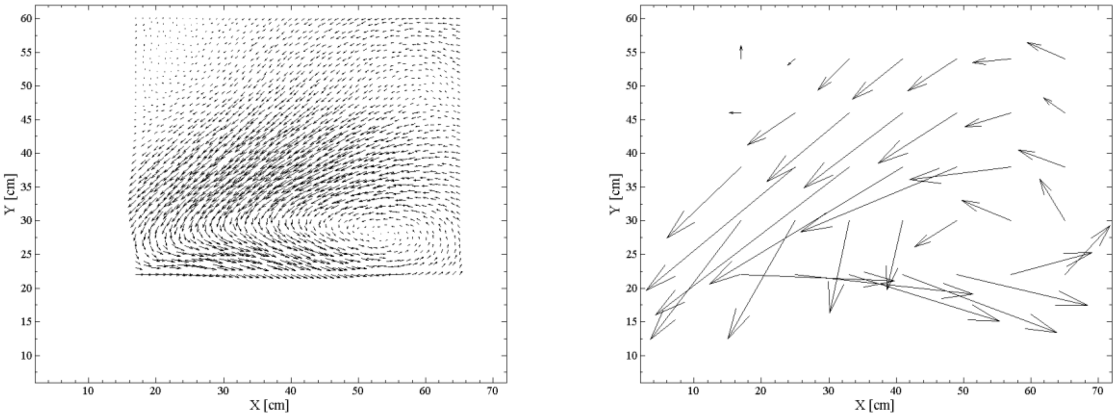

(a) (b)

Figure 6.23 POD mode 1 resulting from: (a) the original and (b) the low-resolution dataset

It has to be reminded that the vector magnitudes in the POD modes and the amplitudes of the corresponding POD coefficients are related to each other. The velocity contribution of a POD mode is obtained as the product of the vectors of the POD mode and the values of the corresponding POD coefficient. Consequently, the product is unchanged if the increase in the vectors is compensated by the decreased values of the corresponding POD coefficient.

For the comparison of the POD results arising from the different datasets, the POD results of the low-resolution dataset were rescaled as follows. The vectors of the low-resolution POD modes were divided by a scale factor, while the values of the corresponding POD coefficients were multiplied by the same scale factor, so that the velocities reproduced by the POD modes remain unchanged. The scale factor was calculated for each POD mode *i* based on the standard deviations of the corresponding POD coefficients arising from the different datasets as:

$$sf_i = \frac{\sigma_{ai}^{O}}{\sigma_{ai}^{L}} \tag{6.1}$$

where $\sigma_{ai}{}^{O}$ denotes the standard deviation of a_i resulting from the original dataset and $\sigma_{ai}{}^{L}$ denotes the standard deviation of a_i resulting from the low-resolution dataset. The scale factor yielded sf_1 = 14.94 for POD mode 1 and sf_2 = 14.27 for POD mode 2 in the present datasets.

After rescaling the POD results of the low-resolution dataset as described above, the vector fields of POD modes 1 and 2 resulting from the different datasets (Figure 6.24) and the time series of POD coefficients a_1 and a_2 resulting from the different datasets (Figures 6.25 and 6.26) can be compared. It can be recognized that the POD results of the different datasets yield to the same magnitudes both in the vector fields of the POD modes and in the values of the POD coefficients.

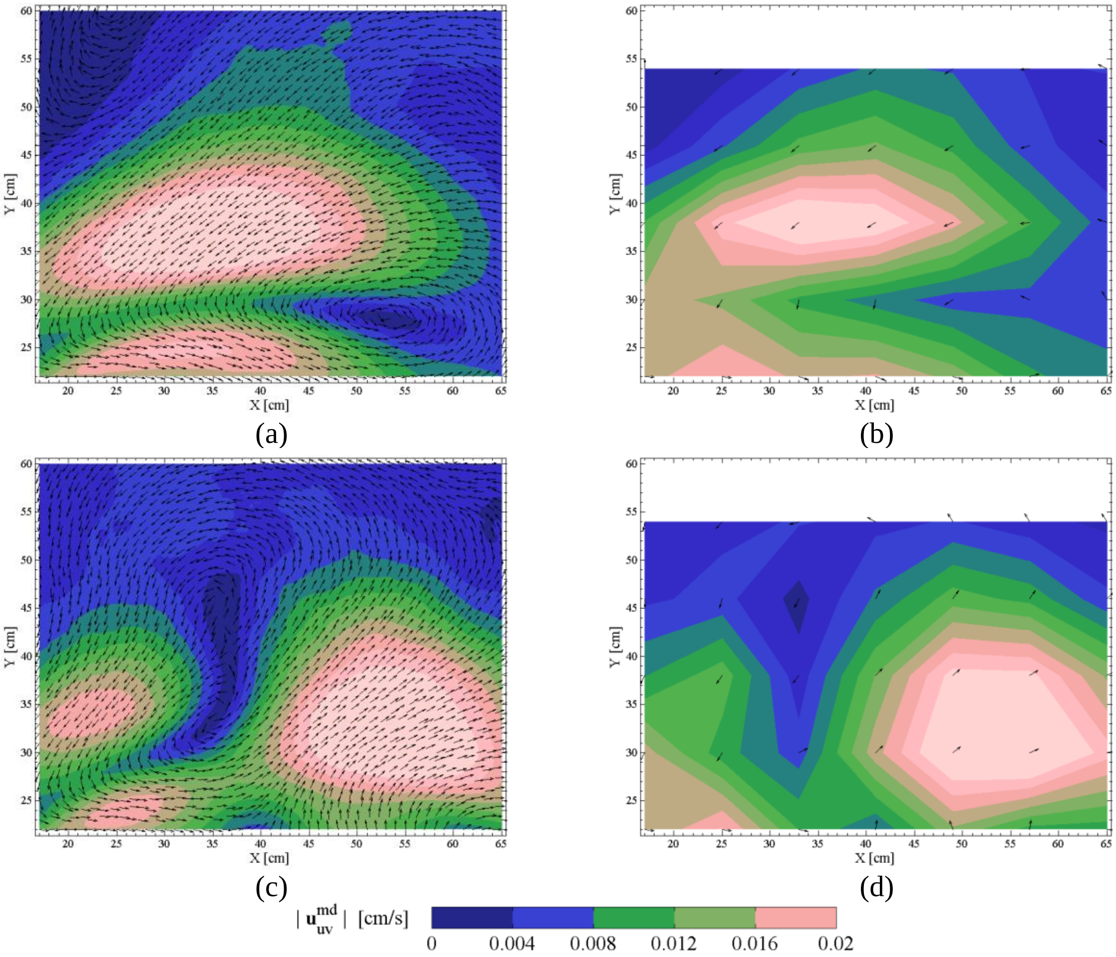

Figure 6.24 POD modes 1 and 2 after rescaling the low-resolution POD results:
(a) POD mode 1 of the original dataset, (b) POD mode 1 of the low-resolution dataset,
(c) POD mode 2 of the original dataset and (d) POD mode 2 of the low-resolution datasets.

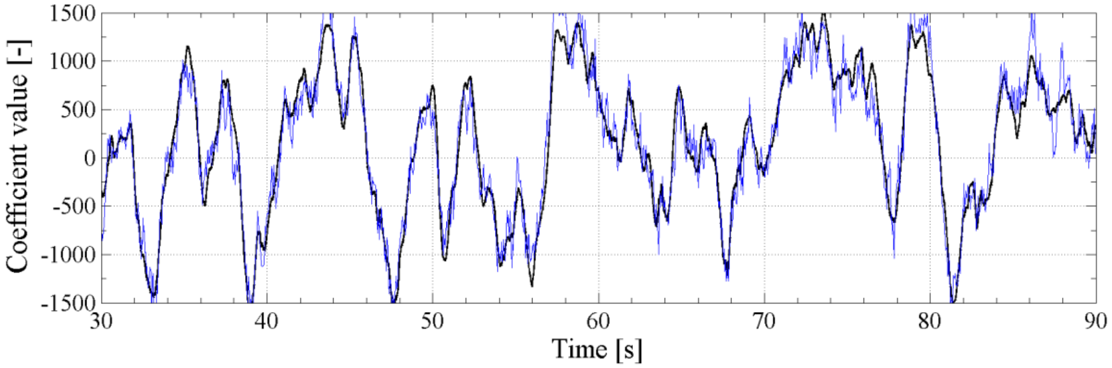

Figure 6.25 Time series of the POD coefficients a_1 resulting from the original dataset (thick black line) and from the low-resolution dataset after rescaling (thin blue line)

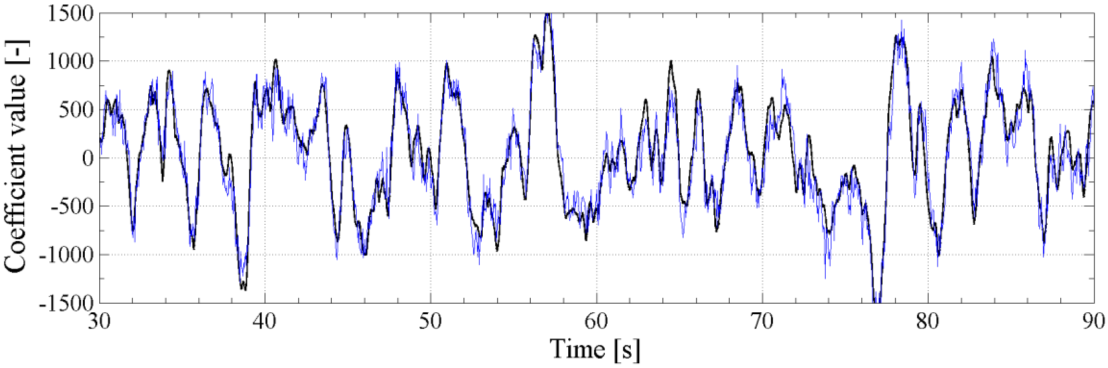

Figure 6.26 Time series of the POD coefficients a_2 resulting from the original dataset (thick black line) and from the low-resolution dataset after rescaling (thin blue line)

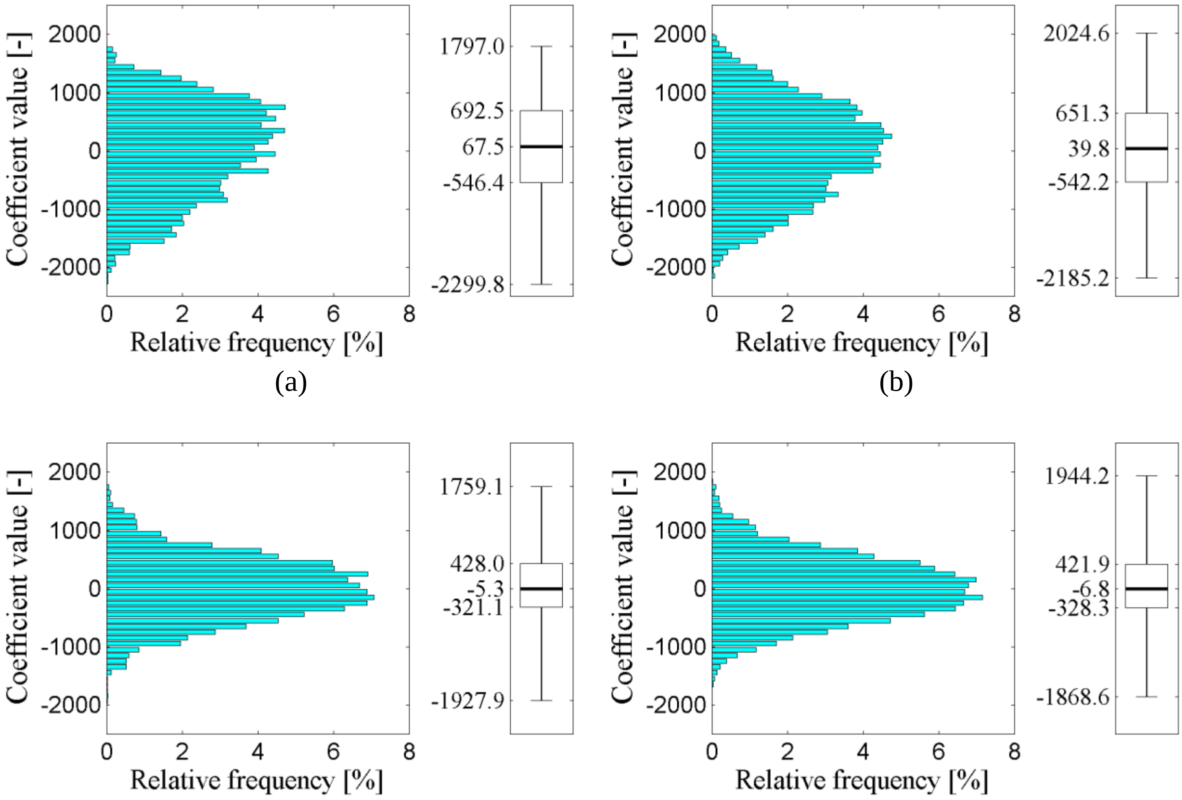

(a) (b) (c) (d)

Figure 6.27 Amplitude distributions of the POD coefficients after rescaling the low-resolution POD results: (a) POD mode 1 of the original dataset, (b) POD mode 1 of the low-resolution dataset, (c) POD mode 2 of the original dataset and (d) POD mode 2 of the low-resolution datasets.

In Figures 6.25 and 6.26 it can be further recognized that the time series of POD coefficients a_1 and a_2 resulting from the different datasets are essentially the same; minor differences arise from the small-scale fluctuations present in the coefficients of the low-resolution datasets. While these small-scale fluctuations affect the characteristic amplitudes of the time series to some extent (Figure 6.27), they do not have an effect on the characteristic frequencies of the POD coefficients (Figure 6.28).

Further, it can be observed that the cross-correlation function of the POD coefficients a_1 and a_2 resulting from the low-resolution dataset essentially yield the same time lags as the original dataset (Figure 6.29).

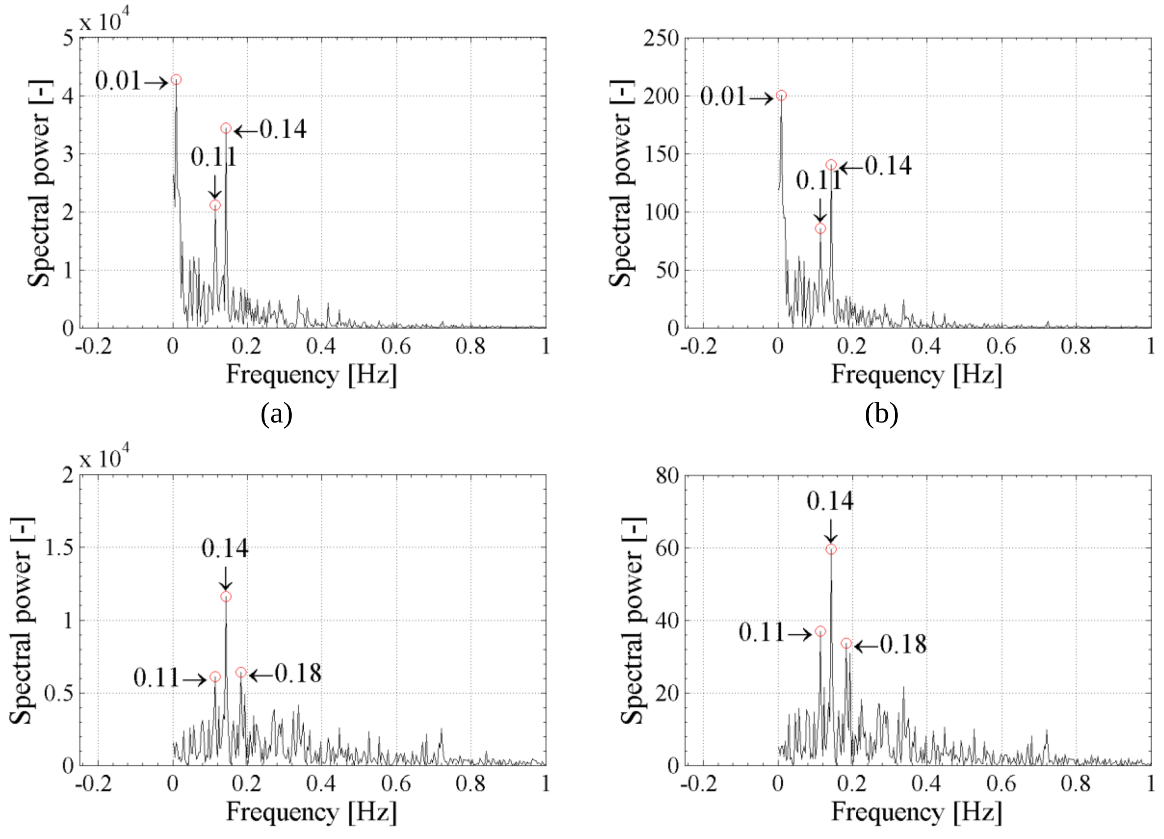

Figure 6.28 Characteristic frequencies of the POD coefficients:
(a) POD mode 1 of the original dataset, (b) POD mode 1 of the low-resolution dataset,
(c) POD mode 2 of the original dataset and (d) POD mode 2 of the low-resolution datasets.

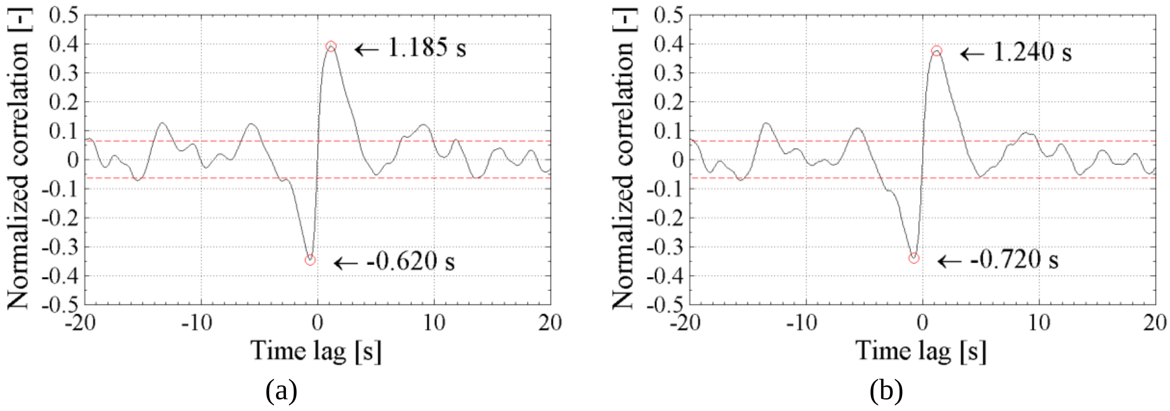

Figure 6.29 Cross-correlation functions of the POD coefficients a_1 and a_2 resulting from
(a) the original dataset and (b) the low-resolution dataset.
The dashed lines denote the standard deviation of the function.

It has to be highlighted that it has not been investigated explicitly how grid the resolution or the placement of the grid points affect the POD results arising from the low-resolution dataset. Though, it is reasonable to assume that the results become different if the patterns within the POD modes are not sufficiently represented by the low-resolution grid points. In return, the number of grid points is probably further reducible, provided that the grid points are optimally placed with respect to the patterns within the POD modes of interest.

It has to be pointed out that, although the time series of the POD coefficients a_1 and a_2 are well reproduced by the low-resolution dataset used in this example, the flow processes represented by the corresponding POD modes are hardly comprehensive using solely the low-resolution POD modes. As the grid spacing of the vectors is too large, neither the processes can be well interpreted nor the location of the main-stream centerlines can be determined in the reconstructed velocity fields. Thus, the correct interpretation of the low-resolution POD modes requires prior knowledge of the high-resolution POD modes, which, however, can originate from a separate measurement of the same flow that can also be carried out in a scale model.

6.4 Summary

In this chapter, the methodology has been presented that is suitable for detecting predictable flow events and their occurrences. Leaning on the fundamental assumption described at the beginning of the chapter, the presented methodology detects repeating sequences of large-scale flow events and their occurrences based on POD results. The methodology essentially consists of the detailed examination of POD modes of high energy contributions, which proved to be deterministic in representing processes of the flow (see Section 5.3.3).

The methodology has been demonstrated in this chapter on the PIV measurement performed in the scale model of a vertical-slot fish pass and has shown that:

- POD modes 1 and 2 represent large-scale flow events that occur repeatedly in the flow
- the occurrences of flow events represented by POD modes 1 and 2 can be identified in the POD-coefficient time series due to the compact description of processes provided by POD
- a connection between POD modes 1 and 2 could be identified based on both the cross-correlation function and the frequency spectra of their time series
- the temporal occurrences of flow events represented by POD modes 1 and 2 reveals that they occur sequentially.

In terms of flow processes, POD modes 0-1 essentially reproduce the non-periodically oscillating main stream, and POD mode 2 complements this by the appearance and position change of further flow structures connected with the oscillation.

In terms of flow events, POD modes 1 and 2 form a repeating sequence of following flow events (see Figure 6.13):

1. a transversal current from the left-hand side of the main stream pushes the main stream to the right,
2. a flow structure entering the measurement field from upstream does not follow the new main-stream trajectory but leaves the main stream to the left-hand side of the main stream,
3. the flow structure travels along the left side of main stream, thereby pulling the main stream to the left-hand side and becoming less and less distinguishable from the main stream,
4. the flow structure leaves the measurement field, while the main stream returns to its original position.

The sequential occurrence of these flow events proves that both the first and the second conditions of predictability formulated at the beginning of the chapter are fulfilled, i.e. there exist repeating sequences of flow events in the flow.

This sequence of flow events is repeating in non-periodic intervals in the measured dataset. Although the repeating sequence of flow events remains essentially the same, each of the occurrences is somewhat different. This implies that the time lag between the occurrences of flow events within the repeating sequence varies to some extent at different occurrences of the repeating sequence, which has to be considered in later fish-behavior experiments. Though, an average time lag between the occurrences of flow events within the repeating sequence can be provided using the cross-correlation function of the involved POD-coefficient time series, which gave about 1.2 s in the present measurement.

Although the trigger of the process cannot be ultimately identified, it is reasonable to assume that the subsequent occurrence of the two following flow events generates the oscillation. These are the transversal current from the left-hand side of the main stream that pushes the main-stream trajectory to the right (1), and the flow structure arriving with the main stream in form of a burst that does not follow the new main-stream trajectory (2). This interpretation is strengthened by the additional POD modes of high energy contributions that apparently also represent repeating bursts arriving from upstream (Figure 6.8), but do not cause main-stream displacements.

In this chapter, it has also been demonstrated how a supplementary flow feature not represented by a POD mode can be involved into the examination or, in other words, how a connection between the repeating sequence of flow events represented by POD modes and the change of a supplementary flow feature can be identified. This can be required if such a supplementary flow feature is relevant for fish behavior, i.e. it describes flow situations that are advantageous or disadvantageous for fish. Since the occurrences of both the flow events and the examined flow situations are repeating non-periodically, it is reasonable to look for the connection based on their time series. Although demonstration used only a hypothetically advantageous flow situation, the presented scheme can be enhanced in the future using other flow situations or flow features based on results of fish-behavior studies.

Finally, it has been demonstrated that the occurrences of predictable flow events can be detected by low-resolution measurements that are feasible by means of point measurement techniques in full-scale facilities, provided that the POD modes relevant for the predictability had been determined first by PIV. This is essential for the applicability of the methodology for evaluating fish behavior, because the measurement has to be performed simultaneously to fish-behavior observations in the full-scale facility, where PIV is hardly possible.

For this demonstration a low-resolution velocity dataset has been generated from the high-resolution PIV measurement, then POD modes and POD coefficient obtained from the high- and the low-resolution datasets have been compared. The results have confirmed that the temporal sequences of flow events represented by POD modes 1 and 2 could be well identified in the POD-coefficient time series obtained from the low-resolution dataset. In turn, although the POD modes 1 and 2 of the low-resolution dataset were essentially the same as the ones in the original dataset, the POD modes of the low-resolution dataset are difficult to interpret without the POD results of the original dataset. For this reason, the high-resolution dataset is required as a reference for the analysis of the low-resolution dataset.

These considerations suggest that the predictable flow events have to be determined first based on a PIV measurement, which can also be performed in a scale model of the facility; then grid point positions and measurement frequency of the low-resolution measurement have to be determined and optimized based on the POD of the PIV measurement; and finally the low-resolution measurement can be performed simultaneously with the fish-behavior experiments.

7 Conclusions and outlook

One of the features determining the influence of turbulence on fish behavior is, according to an earlier publication, the predictability of turbulence, which has been interpreted in this work as the existence of turbulent *flow events* in the flow field whose *occurrences* are predictable. Here, the term *flow event* is used to denote changes in the flow associated with the appearance of turbulent flow structures or their change of position, such as the appearance of a turbulent eddy at a location or the trajectory displacement of an unsteady main stream. The term *occurrence* denotes instances of times at which the particular flow event happens, e.g. when a particular turbulent eddy appears at a given location.

This work has developed a flow-analysis methodology for detecting predictable flow events in vertical-slot fish passes, even if they occur non-periodically. The fundamental assumption of the present approach is that repeating flow events are the basis for predictability, because repetition facilitates their recognition by experience on the fish' part. Leaning on this assumption, the following requirements for predictability have been formulated:

1. flow events occurring repeatedly in the flow exist;
2. repeating sequences of different flow events exist in the flow.

If these conditions are fulfilled, the flow events occurring later within the repeating sequence can be considered predictable in the sense of short-term predictability, even if the sequence itself is repeating non-periodically. It has to be reminded that the feature of predictability refers to the flow alone. The methodology presented here is accordingly based on the analysis of the flow.

In the following, the summary and conclusions concerning the results are followed by recommendations for the future work.

7.1 Summary and conclusions

The methodology developed in this thesis has been applied to a measurement performed with Particle Image Velocimetry (PIV) in a scale model of a vertical-slot fish pass. The following main issues have been discussed in details concerning the methodology:

1. The interpretation of POD results (Section 5.3) and the presentation of the methodology (Section 6.1). This included whether POD results are suitable for representing flow structures, how to detect flow events based on the POD results, how to identify a temporal sequence of connected flow events and their occurrences.
2. The involvement of supplementary flow features into the examination (Section 6.2)
3. Considerations on performing the measurements by means of point measurement techniques during fish-behavior experiments (Section 6.3).

7.1.1 The developed methodology under consideration of the interpretation of POD results

The presented methodology is based on POD (see Section 2.5). Briefly explained, POD creates a set of orthonormal basis functions for the input velocity dataset in form of single vector fields called *POD modes*. This implies, firstly, that the instantaneous velocity fields of the *input dataset can be reconstructed* at each time step as a linear combination of the POD modes, and secondly, that the coefficients corresponding to a given POD mode at all time steps can be expressed as a *time series*. A POD mode multiplied by the coefficient value at a given time step produces a single vector field, which is called in this work *velocity contribution of the POD mode* at the given time step. Further, the variance of the coefficient's time series gives the variance contribution of the POD mode, which is proportional to the *kinetic-energy contribution of the POD mode*.

The discussion on the interpretation of POD modes (Section 5.3) pointed out that POD modes form in combination with the coefficient time series – periodic or non-periodic – spatial oscillations, which can be used to reconstruct the input dataset. While the vortical structures observed in the vector fields of the POD modes are not real flow structures by themselves, POD modes can represent flow structures. Whether POD modes do represent real flow structures and can be used to detect flow events, has to be examined individually.

The detailed examination of the POD modes calculated from the PIV measurement performed in this work (Section 6.1) proved that POD modes 1 and 2 do represent significantly flow events that occur repeatedly. While POD mode 1 describes the non-periodically oscillating main stream, POD mode 2 represents additional repeating flow events within the measurement field. Further, the time series of coefficients corresponding to POD modes 1 and 2 can be used to identify the occurrences of such repeating flow events.

From the point of view of representing flow structures, the following conclusions can be deduced on POD modes.

- Large flow structures that occur repeatedly at exactly the same location – like eddies shed behind a fixed obstruction – are expected to be represented well at that location by one (or two) POD modes having high energy contributions. Consequently, such flow structures are reconstructed well at that location by those POD modes at each time step, so that the occurrences of the flow events associated with such flow structures can be detected based on the coefficient time series of the involved POD modes
- Large flow structures that occur repeatedly at nearly but not exactly the same location – like eddies separating at somewhat variable locations, or a main stream with an oscillating centerline – are expected to generate more POD modes of high energy contributions as follows. A single POD mode having a very high energy contribution contains a kind of spatial intersection of the individual occurrences. Additional POD modes having lower energy contributions contain the difference between that spatial intersection and the specific vector pattern at the individual occurrences. Therefore, the specific vector pattern of such a flow structure at a given occurrence can be *reconstructed* by adding the contribution of the single POD mode containing the intersection and additional POD modes that modulate the first one at the given occurrence. While the single POD mode containing the spatial intersection is not sufficient to reconstruct such flow structures at each individual occurrence exactly, this POD mode is re-

quired for the reconstruction at any particular occurrence. Therefore, the single POD mode containing the intersection can be used to identify all the occurrences of such flow structures. For example, in the case of the oscillating main stream in the presented measurement, POD mode 0 (the mean velocity field) can be regarded as the single POD mode containing the spatial intersection of the individual occurrences, while POD mode 1 provided the vector patterns of the main stream at different times.

As mentioned earlier, the occurrences of the flow structure represented by a POD mode is can be detected based on the time series of the corresponding POD coefficient. In this study, the examination of the coefficient time series corresponding to POD mode 1 and 2 (Section 6.1) showed that the flow events represented by these POD modes do occur sequentially. This confirms that both the first and the second conditions of predictability formulated at the beginning are fulfilled; i.e. repeating sequences of flow events in the flow do exist. The coefficient time series of the involved POD mode can also be used to detect the time lags between occurrences of the subsequent flow events.

Therefore, it can be concluded that repeating flow events, arising from large-scale flow structures can be efficiently identified in a velocity dataset using POD. For the detection of such flow events it is sufficient that a POD mode represents the underlying flow structure to a significant extent, even when this does not occur at exactly the same location. The occurrences of flow events associated with such flow structures can be detected based on the time series of the POD coefficients, which describes the history of occurrences compactly. The coefficient time series of different POD modes can then be used to determine sequences of occurrences.

It has to be pointed out that, in principle, any of the POD modes is a possible basis for the presented methodology, so long as it significantly represents flow events. However, as lower order POD modes are expected to represent large flow events occurring frequently, they are expected to be more suitable for the methodology. The results of Tarrade et al. (2011) suggest, in particular, that in the pools of vertical-slot fish passes there might be other flow events that are relevant for predictability. Although they did not investigate repeating flow events using the time series of the POD coefficients, based on the vector field patterns of POD modes they deduced two additional POD modes to be connected with POD mode 1. Since the vector field of those POD modes produced significant velocity contributions in areas not covered by the present measurement field, they could not be captured here.

7.1.2 The involvement of supplementary flow features into the examination

By using POD, only flow events can be detected that occur inside the measurement field and that are represented by POD modes. If a flow feature not represented by a POD mode is considered relevant for predictability, it has to be involved supplementary into the examination. Such a supplementary flow feature is in case of this work, for example, the flow velocity in the slot, since it is outside the measurement field and is certainly relevant for fish, as fish inevitably have to swim across the slot. The temporal change of the flow velocity in the slot (the velocity time series) describes a *flow situation* that can be advantageous or disadvantageous for fish depending on whether flow velocities at the slot are temporally low or high. Since it can be expected that the predictability of such advantageous or disadvantageous flow situations is relevant for fish, the inclusion of supplementary flow features describing such flow situations into the examination is reasonable.

The example of Section 6.2 has shown how to establish a connection between a repeating sequence of flow events and a supplementary flow feature describing advantageous or disadvantageous flow situations. Since repeating flow events occur non-periodically, it is reasonable to look for such a connection based on the time series of the specific flow feature and of the POD coefficient.

It has to be highlighted that:

- the examined flow feature can be any arbitrary unsteady parameter of the flow (e.g. flow velocity, velocity gradient, size of a region with particular flow velocity or other flow features, etc.) so long as a time series of it can be formed.
- the location of the flow situation that is advantageous or disadvantageous for fish can be outside of the measurement field of the whole-field measurement used for the POD analysis. However, in this case the separate measurement of the flow feature describing the flow situation has to be simultaneous with the whole-field measurement.

Although it has not been explicitly discussed in this study, there might also be a time lag between the occurrences of a repeating flow event and the occurrences of the supplementary flow feature describing a relevant flow situation. In such cases a further analysis of the two time series should be considered, e.g. as one with the POD coefficients in Figures 6.15and 6.16. In addition, the correlation scatter plots (Figure 6.20) can be drawn after applying a time shift to one of the time series. Such a time lag has to be considered during the evaluation of fish-behavior experiments.

7.1.3 Considerations on performing the measurements by means of point measurement techniques

It has to be reminded that the feature of predictability refers to the flow alone. It will have to be ascertained using fish-behavior experiments in the future whether fish are actually able to recognize and use predictable flow events of given characteristics (e.g. size of flow structures associated with the flow events relevant for predictability, time lags between flow events). This implies a future need to correlate fish behavior and the occurrences of predictable flow events.

The flow measurement and the fish-behavior observations will have to be performed simultaneously considering that the repeating sequences of flow events relevant for predictability occur non-periodically, and also that, for each occurrence of the repeating sequence, the time lag between the flow events within the sequence will vary somewhat. Moreover, since fish-behavior experiments have to be carried out in full-scale facilities (due to the scale dependence of the influence of turbulence, see Section 1.1), measurements using PIV are hardly possible.

For this reason, it has been demonstrated in this study that the occurrences of the repeating flow events can be detected by very-low-resolution “whole-field” measurements that are, in principle, feasible by means of point measurement techniques (Section 6.3). The presented demonstration has, however, also shown that the POD modes relevant for predictability must have been determined based on a high-resolution dataset prior to the low-resolution measurements. Although this hypothesis has not been investigated explicitly, it is reasonable to assume that the POD results obtained from the low-resolution datasets will depend on the layout of the low-resolution grid points. That is to say, the layout of the low-resolution grid has to reproduce the pattern in the vector fields of relevant POD modes sufficiently. As a consequence, the layout of the low-resolution grid has to be optimized based on the

POD modes obtained from a high-resolution dataset, which, thus, has to be available prior to the low-resolution measurements.

Taking into account that PIV measurements are usually not possible in a full-scale facility, the consequence of the above considerations is that the primary PIV measurements providing the high-resolution dataset must be performed in a scale model of the full-scale facility.

7.2 Recommendations for the future work

As a conclusion, a plausible methodology for detecting predictable flow events in fish-behavior experiments may consist of the following steps:

1. Perform a primary high-resolution PIV measurement in the facility of interest. If PIV is not possible in the facility (e.g. due to its size, turbidity), the measurement must be performed in a scale model of it. Further, those flow features not captured by the PIV measurement but relevant for fish behavior (supplementary flow feature describing advantageous or disadvantageous flow situations) need to be measured simultaneously by an additional measurement system.
2. Identify repeating sequences of flow events based on POD of the PIV measurement as described in Section 6.1:
    a. Identify POD modes representing repeating flow events
    b. Identify connections between POD modes, i.e. connected repeating flow events
    c. Determine the sequence of the connected repeating flow events, i.e. the repeating sequence of flow events
3. Identify the connection between the repeating sequence of flow events represented by POD modes and supplementary flow features describing advantageous or disadvantageous flow situations (Section6.2).
4. Determine the grid layout and the measurement frequency required to obtain the time series of POD-coefficient needed to detect the predictable flow events with low-resolution measurements (Section 6.3).
5. Perform the low-resolution measurements in the full-scale facility in order to identify occurrences of repeating flow events. If a scale model has been used for the PIV measurements, compare the characteristics of the POD coefficients obtained from the two different facilities in order to exclude modeling effects (Figure 6.27).

During the evaluation of fish-behavior experiments, the following temporal aspects have to be considered:

- the repeating sequence of the flow events relevant for predictability occurs non-periodically, hence at irregular time intervals (Section 6.1.3).
- although each repeating sequence remains essentially the same, each occurrence is somewhat different, which implies that the time lag between the flow events within the sequence varies to some extent from occurrence to occurrence (Section 6.1.3).
- if an advantageous or disadvantageous flow situation is given by a supplementary flow feature, then a time lag might exist between the occurrences of the repeating flow events being

part of the repeating sequence and the occurrences of the advantageous or disadvantageous flow situations.

Based on the conclusions of this study, the following recommendations can be made for improving the methodology for investigations in vertical-slot fish passes:

- in order to capture all flow events possibly connected with the main-stream oscillation, the PIV measurements should cover as large an area of the pools as possible, and especially the regions near the slot.
- the flow at the upstream slot should be captured with supplementary measurements and simultaneously with the PIV measurements, in order to examine whether also the flow changes in the slot are predictable.
- the instantaneous water levels should be measured at several locations in the pools simultaneously with the PIV measurements, in order to examine whether the main-stream displacements can be determined by water level measurements. Since the oscillation appears to be partly caused by fluid exchange between the recirculation and the main-stream regions, it is speculated that the oscillation has a significant influence on the instantaneous water levels.

While the presented methodology provides a practical framework for investigating the predictability of non-periodically repeating flow events, the following aspects of the methodology need further clarification.

The 2D-2C PIV system used in the present work provided two-dimensional velocity vectors, and the flow events relevant for the predictability have been detected based on two-dimensional velocities. Since these flow events represented a relative high turbulent kinetic energy (see the TKE contributions of POD modes 1 and 2 in Figures 5.9 and 6.5), and since according to the literature (Section 3.3) the turbulent kinetic energy has been found to be independent of the distance from the bottom, it can fairly safely be assumed that such large-scale flow events occupy the whole water depth and are, consequently, well characterized using the horizontal velocity components in vertical-slot fish passes. However, it should be verified whether the measurement errors caused by discarding the vertical component of the velocity (see Section 4.3.5) are negligible for the results. This should also be considered for further flow events relevant for predictability not included in the limited measurement field.

The results presented in this work have shown that the flow in the present fish pass model has predictable components. It remains to be confirmed whether other pool geometries also generate predictable flow events, and it should also be investigated whether the characteristics of the predictable flow events (e.g. location of the relevant flow events, time lags) are dependent on the pool geometry. Although the quantitative comparison of the characteristics of POD modes measured in different geometries is possible by simple means as shown in e.g. Figures 6.27 and 6.286.28, a more sophisticated comparison can be performed using the Common Base POD (Kriegseis et al. 2010).

It should also be noted that the main-stream oscillation, which plays an essential role in the predictability for the present measurement, has not been measured in a real fish pass yet. This is, to a large extent, due to the lack of a whole-field measurement method that is applicable to the case. By using low-resolution measurements as suggested in this work (Section 6.3), the main components of the oscillation can be determined also in field. Based on such measurements it should be ascertained whether this oscillation is also present in real facilities, and whether it has the same characteristics as in the corresponding scale models. The latter point for attention is important in order to exclude that, in the laboratory apparatus, the filling process and the size of the inflow tank influence the oscillation. The characteristics of the oscillation components measured in the prototype can then be compared with those measured in the scale model by using the quantitative characteristics of the relevant POD modes as shown in e.g. Figures 6.27 and 6.28.

The low-resolution measurements performed simultaneously with fish-behavior observations are expected to disturb fish to some extent. On the one hand, this disturbance can be obviously reduced by decreasing the used number of measurement devices, hence the number of grid points. On the other hand, the disturbance of the measurement device is expected to be reduced by placing the point measurement devices in regions where they cause fewer disturbances for fish, which should be considered in step 4 above.

In case of vertical-slot fish passes, where large-scales repeating flow events are assumed to occupy the whole water depth, the placement of the measurement devices near the water surface has to be considered as follows. Firstly, further investigations should ascertain that the predictable flow events detected by the present methodology actually occupy the whole water depth. Secondly, it has to be examined at which distance from the water surface they are still detectable, in order to exclude near-surface influences. Moreover, the number of measurement devices, hence of grid points, might be further reduced, if the main-stream displacements could rather be detected by water level measurements as speculated before.

The conclusive proof of the suitability of this methodology for the investigation of predictable flow events can be only obtained by applying the methodology in a fish-behavior experiment. Thereby, it could be ascertained whether fish are able to recognize and use repeating flow events and the repeating sequences as assumed in the presented study.

The predictability is of particular importance in vertical-slot fish passes, because such facilities consist of several dozens of pools, which implies that fish encounter almost the same flow again and again in such facilities. Accordingly, a pattern learned at the beginning of such a facility is applicable again and again further upstream. The main-stream oscillation, observed both in the present work and in two previous studies (Sections 3.3 and 6.1.1), certainly increases the chance that predictable flow events exist. Nonetheless, the adaptation of the present methodology to other hydraulic structures than vertical-slot fish passes deserves separate considerations.

8 References

Adrian, R. J.; Christensen, K. T. & Liu, Z.-C. (2000), Analysis and interpretation of instantaneous turbulent velocity fields, *Experiments in Fluids* **29**, 275-290.

Aubry, N. (1991), On the hidden beauty of the proper orthogonal decomposition, *Theoretical and Computational Fluid Dynamics* **2**(5-6), 339-352.

Barnett, V. (e. (1981), *Interpreting Multivariate Data*, John Wiley & Sons.

Bendat, J. S. & Piersol, A. G. (2000), *Random Data Analysis and Measurement Procedures*, John Wiley & Sons.

Bernero, S. & Fiedler, E. H. (2000), Application of particle image velocimetry and proper orthogonal decomposition to the study of a jet in a counterflow, *Experiments in Fluids* **29**(1), 274--281.

Cordier, L. & Bergmann, M. (2008), Proper Orthogonal Decomposition: an overview, 'Lecture series 2002-04, 2003-03 and 2008-01 on post-processing of experimental and numerical data, Von Karman Institute for Fluid Dynamics, 2008.', VKI, , pp. 46 pages.

Davidson, P. A. (2004), *Turbulence, an introduction for scientists and engineers*, Oxford University Press.

DVWK (1996), *Fischaufstiegsanlagen - Bemessung, Gestaltung, Funktionskontrolle*, In: DWA-Regelwerk, Deutscher Verband für Wasserwirtschaft und Kulturbau - German Association for Water, Wastewater and Waste

DWA (2014), M-509: *Fischaufstiegsanlagen und fischpassierbare Bauwerke*, In: DWA-Regelwerk, Deutsche Vereinigung für Wasserwirtschaft, Abwasser und Abfall e.V.

DWA (2010), M-509 (Entwurf): *Fischaufstiegsanlagen und fischpassierbare Bauwerke - Gestaltung, Bemessung, Qualitätssicherung*, In: DWA-Regelwerk, Deutsche Vereinigung für Wasserwirtschaft, Abwasser und Abfall e.V.

Enders, E. C.; Boisclair, D. & Roy, A. G. (2003), The effect of turbulence on the cost of swimming for juvenile Atlantic salmon (Salmo salar), *Canadian Journal of Fisheries and Aquatic Sciences* **60**, 1149-1160.

Feng, L.-H.; Wang, J.-J. & Pan, C. (2011), Proper orthogonal decomposition analysis of vortex dynamics of a circular cylinder under synthetic jet control, *Physics of Fluids* **23**(1), 014106.

Frigo, M. & Johnson, S. (1998), FFTW: an adaptive software architecture for the FFT, *Proceedings of the 1998 IEEE International Conference on Acoustics, Speech and Signal Processing* 3, 1381 - 1384.

Fuentes-Perez, J. F.; Sanz-Ronda, F. J.; Martinez de Azagra Paredes, A. & Garcia-Vega, A. (2014), Modeling Water-Depth Distribution in Vertical-Slot Fishways under Uniform and Nonuniform Scenarios, *Journal of Hydraulic Engineering* **140**(10), 06014016.

Guiny, E.; Ervine, D. A. & Armstrong, J. D. (2005), Hydraulic and Biological Aspects of Fish Passes for Atlantic Salmon, *Journal of Hydraulic Engineering* **131**(7), 542-553.

Harris, F. (1978), On the use of windows for harmonic analysis with the discrete Fourier transform, *Proceedings of the IEEE* **66**(1), 172-204.

Heller, V. (2011), Scale effects in physical hydraulic engineering models, *Journal of Hydraulic Research* **49**(3), 293-306.

Hoar, W. S. & Randall, D. J. (eds.) (1978), *Fish physiology*, Academic Press New York..

Höger, V.; Henning, M. & Nestmann, F. (2014), Experimental study on the influence of pool geometry on flow patterns in vertical-slot fishways, *Proceedings of the 10th International Symposium on Ecohydraulics* 2014.

Kriegseis, J.; Dehler, T.; Gnirss, M. & Tropea, C. (2010),'Common-base proper orthogonal decomposition as a means of quantitative data comparison, *Measurement Science and Technology* **21**(8), 085403.

Krüger, F.; Heimerl, S.; Seidel, F. & Lehmann, B. (2010), Ein Diskussionsbeitrag zur hydraulischen Berechnung von Schlitzpässen, *Wasserwirtschaft* **100**(3), 30-36.

Lacey, R. W. J.; Neary, V. S.; Liao, J. C.; Enders, E. C. & Tritico, H. M. (2011), The IPOS framework: linking fish swimming performance in altered flows from laboratory experiments to rivers, *River Research and Applications* **28**(4), 429-443.

Larinier, M. (1992), Passes a bassins successifs, prebarrages et rivieres artificielles, *Bulletin Francais de Peche et Pisciculture* **326-327**, 45-72.

Ledoux, H. (2006), Modelling Three-dimensional Fields in Geoscience with the Voronoi Diagram and its Dual, PhD thesis, University of Glamorgan.

Liao, J. C. (2007), A review of fish swimming mechanics and behaviour in altered flows, *Philosophical Transactions of the Royal Society B: Biological Sciences* **362**(1487), 1973-1993.

Liao, J. C. (2003), The Karman gait: novel body kinematics of rainbow trout swimming in a vortex street, *Journal of Experimental Biology* **206**(6), 1059-1073.

Liu, M.; Rajaratnam, N. & Zhu, D. Z. (2006), Mean flow and turbulence structure in vertical slot fishways, *Journal of Hydraulic Engineering* **132**, 765-777.

Lumley, J. (1967), The structure of inhomogeneous turbulent flows, In: *Atmospheric Turbulence and Radio Wave Propagation*, Nauka, 166-178.

Meyer, K. E.; Pedersen, J. M. & Özcan, O. (2007), A turbulent jet in crossflow analysed with proper orthogonal decomposition, *Journal of Fluid Mechanics* **583**, 199-227.

Nikora, V.; Aberle, J.; Jowett, I.; Biggs, B. & Sykes, J. (2003), On turbulence effects on fish swimming performance: a case study of the new zealand native fish galaxias maculatus (inanga), *Proceedings of the XXX IAHR Congress*, 425-432.

Nikora, V. I. & Goring, D. G. (1998), ADV measurements of turbulence: can we improve their interpretation, *Journal of Hydraulic Engineering* **124**(6), 630-634.

Odeh, M.; Noreika, J. F.; A., H.; A., M.; Castro-Santos, T. & F., C. G. (2002), Evaluation Of The Effects Of Turbulence On The Behavior Of Migratory Fish, Final Report 2002, Report to Bonneville Power Administration, Contract No. 00000022, Project No. 200005700, 55 electronic pages (BPA Report DOE/BP-00000022-1)), Technical report, Bonneville Power Administration.

Pollock, D. (1999), *Handbook of Time Series Analysis, Signal Processing, and Dynamics*, Academic Press.

Pope, S. B. (2000), *Turbulent Flows*, Cambridge University Press.

Powers, P. & Orsborn, J. (1984), New Concepts in Fish Ladder Design: Analysis of Barriers to Upstream Fish Migration, Volume IV of IV; Investigation of the Physical and Biological Conditions Affecting Fish Passage Success at Culverts and Waterfalls, Technical report, Bonneville Power Administration, Project No. 198201400, 134 electronic pages, (BPA Report DOE/BP-36523-1).

Przybilla, A.; Kunze, S.; Rudert, A.; Bleckmann, H. & Brucker, C. (2010), Entraining in trout: a behavioural and hydrodynamic analysis, *Journal of Experimental Biology* **213**(17), 2976-2986.

Puertas, J.; Pena, L. & Teijeiro, T. (2004), Experimental Approach to the Hydraulics of Vertical Slot Fishways, *Journal of Hydraulic Engineering* **130**, 10-23.

Raffel, M.; Willert, C. E. & Kompenhaus, J. (1998), *Particle Image Velocimetry - A Practical Guide*, Springer.

Rajaratnam, N.; Katopodis, C. & Solanki, S. (1992), New designs for vertical slot fishways, *Canadian Journal of civil Engineering* **19**, 402-414.

Rajaratnam, N.; Van der Vinne, G. & Katopodis, C. (1986), Hydraulics of vertical slot fishways, *Journal of Hydraulic Engineering* **112**(10), 909-927.

Ruck, B. e. (1990), *Lasermethoden in der Strömungsmesstechnik*, AT-Fachverlag.

Sirovich, L. (1987), Turbulence and the dynamics of coherent structures part I: coherent structures, *Quarterly of Applied Mathematics* **45**(3), 561-571.

Smith, D. L.; Brannon, E. L. & Odeh, M. (2005), Response of Juvenile Rainbow Trout to Turbulence Produced by Prismatoidal Shapes, *Transactions of the American Fisheries Society* **134**(3), 741-753.

Smith, R. C. & Baker, K. S. (1981), Optical properties of the clearest natural water (200-800 nm), *Applied Optics* **20**(2), 177-184.

Sokoray-Varga, B. & Jozsa, J. (2008), Particle tracking velocimetry (PTV) and its application to analyse free surface flows in laboratory scale models, *Periodica Polytechnica Civil Engineering* **52**(2), 63–71.

Sokoray-Varga, B.; Weichert, R.; Lehmann, B. & Nestmann, F. (2012), Detecting turbulent eddies by means of time-resolved PIV measurements in a vertical-slot fish pass, *Proceddings of the 2nd IAHR Europe Congress: Water infinitely deformable but still limited*.

Sokoray-Varga, B.; Weichert, R. & Nestmann, F. (2015), Untersuchungen zu hydraulischen Berechnungsansätzen von Schlitzpässen, *Wasserwirtschaft* 2015/7-8, 61-66.

Sokoray-Varga, B.; Weichert, R. & Nestmann, F. (2014), Erfassung turbulenter Wirbel in Vertical-slot Fischpässen mittels zeitaufgelöstem PIV, *Fachtagung "Lasermethoden in der Strömungsmesstechnik"*, pp. 8.

Tarrade, L.; Pineau, G.; Calluaud, D.; Texier, A.; David, L. & Larinier, M. (2010), Detailed experimental study of hydrodynamic turbulent flows generated in vertical slot fishways, *Environmental Fluid Mechanics* **11**(1), 1-21.

Tarrade, L.; Texier, A.; David, L. & Larinier, M. (2008), Topologies and measurements of turbulent flow in vertical slot fishways, *Hydrobiologia* **609**, 177–188.

Tritico, H. M. & Cotel, A. J. (2010), The effects of turbulent eddies on the stability and critical swimming speed of creek chub (Semotilus atromaculatus), *Journal of Experimental Biology* **213**(13), 2284-2293.

Tropea, C.; Yarin, A. & Foss, J. F. (eds.) (2007), *Handbook of Experimental Fluid Mechanics*, Springer Science + Business Media.

Vaseghi, S. V. (2008), *Advanced Digital Signal Processing and Noise Reduction*, Wiley-Blackwell.

Wang, R.; David, L. & Larinier, M. (2010), Contribution of experimental fluid mechanics to the design of vertical slot fish passes, *Knowledge and Management of Aquatic Ecosystems* **396**(02), pp. 21.

Westerweel, J. & Scarano, F. (2005), Universal outlier detection for PIV data, *Experiments in Fluids* **39**, 1096-1100.

Wu, S.; Rajaratnam, N. & Katopodis, C. (1999), Structure of flow in a vertical slot fishway, *Journal of Hydraulic Engineering* **125**(4), 351-359.

Yalin, M.S. (1971). *Theory of hydraulic models*. Macmillan.